

Università degli Studi di Torino
Scuola di Dottorato in Scienza ed Alta Tecnologia



Study of Cosmic Ray Neutrons

Antonio Bonardi

Università degli Studi di Torino
Scuola di Dottorato in Scienza ed Alta Tecnologia

Indirizzo di Fisica ed Astrofisica

Study of Cosmic Ray Neutrons

Antonio Bonardi

Tutor: Piero Galeotti

Università degli Studi di Torino
Scuola di Dottorato in Scienza ed Alta Tecnologia

Indirizzo di Fisica ed Astrofisica

Tesi di dottorato - XXII ciclo

Study of Cosmic Ray Neutrons

Torino, 7 Gennaio 2010

Candidato: Antonio Bonardi

Contro-relatore: Francesco Arneodo

Tutor: Piero Galeotti

Co-Tutor: Walter Fulgione

Co-Tutor: Marco Aglietta

Abstract

The work described in this thesis was focused on cosmic rays neutrons for underground and above ground physics.

For underground physics I report the results of a Monte Carlo code used for simulating the propagation of muon induced and radioactivity neutrons inside the LVD (Large Volume Detector) experiment. In particular the attention was focused on their fluxes in the LVD detector central region, called LVD Core Facility, which was proposed for housing a new generation Dark Matter experiment. Inside the LVD Core Facility the attenuation factor radioactivity neutron flux was found 35.9 ± 0.4 , corresponding to $\Phi_n(E_{kin} > 1 \text{ MeV}) = 1.6 \pm 0.4 \cdot 10^{-8} \text{ neutrons cm}^{-2} \text{ s}^{-1}$. No significant reduction was found for muon induced neutrons: nevertheless, by using LVD external part as active veto, the muon induced neutron flux decreased by a factor ~ 50 which corresponds to $\Phi_n(E_{kin} > 10 \text{ MeV}) \sim 1.0 \cdot 10^{-10} \text{ neutrons cm}^{-2} \text{ s}^{-1}$.

For the above ground physics I report the atmospheric neutron flux measurement performed in the Laboratori Nazionali del Gran Sasso Assembly Hall (external site). The detector consisted on a Gd-doped LVD test counter and an active muon veto.

I obtained:

$$\Phi_{neutron}(E > 10 \text{ MeV}) = 63 \pm 6 \text{ neutron s}^{-1} \text{ m}^{-2}$$

$$\Phi_{neutron}(E > 20 \text{ MeV}) = 47 \pm 5 \text{ neutron s}^{-1} \text{ m}^{-2}$$

I report also the measurement of atmospheric muon mean lifetime in C_nH_{2n} liquid scintillator performed with the same device. The muon mean lifetime was found equal to $\tau = 2.125 \pm 0.015 \mu\text{s}$.

Contents

Abstract	i
1 Introduction	1
1.1 Underground Neutrons	1
1.1.1 Energy spectrum	2
1.1.2 Underground neutrons as detector background	4
1.2 Atmospheric Neutrons	5
1.2.1 Altitude neutron flux profile	5
1.2.2 Energy spectrum	6
1.2.3 Solar Neutrons	8
1.2.4 Atmospheric neutrons and electronic devices	12
1.2.5 Atmospheric neutrons and human health	13
1.2.6 Atmospheric neutrons as detector background	14
2 Underground neutrons	16
2.1 The Dark Matter problem	16
2.1.1 The DAMA results	17
2.1.2 The Gran Sasso Laboratories and Experiment for the search of Dark Matter	25
2.1.3 Neutrons as ultimate background for Dark Matter experiments .	30
2.2 The Large Volume Detector	32
2.2.1 The detector	32
2.2.2 LVD as neutron detector and neutron moderator	34

2.3	The LVD Core Facility	36
2.4	Geant4 simulation of LVD Core Facility	37
2.4.1	Muon-Induced Neutrons	39
2.4.2	Radioactivity neutrons inside LVD Core Facility	41
2.5	Conclusion	45
3	The on-the-ground detector	47
3.1	The LVD on-the-ground counter	47
3.2	The active muon veto	49
3.2.1	Instrumentation recovery	49
3.2.2	The design	51
3.2.3	The assembling phase	53
3.2.4	The selection of single module logic of trigger	54
3.2.5	The testing phase	58
3.3	Conclusion	60
4	Geant4 simulation of the on-the-ground detector	61
4.1	The apparatus geometry	61
4.2	Vertical Muons: the released energy	63
4.3	Vertical Muons: the outcoming signal	64
4.4	The Michel Spectrum	67
4.5	Neutron Capture Detection Efficiency	69
4.6	Atmospheric Neutrons Observed Spectrum	71
5	Above the ground measurements	76
5.1	Measurement setup	77
5.2	Energy calibration	78
5.3	Background spectrum	80
5.4	Veto Efficiency Check	83
5.5	Atmospheric Neutrons Flux	87
5.6	Stopping Muons	92

5.7 Muon mean life and Michel spectrum	97
5.8 Conclusions	100
acknowledgments	108

Chapter 1

Introduction

1.1 Underground Neutrons

In underground laboratories a large component of the natural background is due to neutrons (called “Underground Neutrons”) whose energy spectrum is very widespread, ranging from thermal energy up to several GeV. They are divided into two different classes:

- radioactivity neutrons
- muon-induced neutrons

Radioactivity neutrons They are the result of nuclear decay process of radioactive nuclei (mainly ^{238}U) and from (α, n) reactions in the material surrounding the detector, or in the detector itself. In the energy spectrum of underground neutron they are the predominant component up to their running out which happens for $E_{neutron} \lesssim 10$ MeV. Their flux depends by the composition of rock in which the laboratory has been realized and by the quality of concrete (if present) used during its construction. For large underground laboratories, it could happen that the total rate of radioactivity neutrons slightly varies from place to place due to a different concentration of α emitter (mainly ^{222}Rn). This effect can be seen in fig. 2.28 which shows the calculated energy spectrum of radioactivity neutrons inside Hall A and Hall C of LNGS (National Laboratory of

Gran Sasso) underground site [2]: the difference between the two shown spectra is not negligible.

Muon induced neutrons Muon induced neutrons total flux is 2-3 orders of magnitude less than radioactivity one (this ratio varies for each underground laboratory), nevertheless for energy above 10 MeV the total neutron flux in underground sites is only due to muon induced neutrons.

They are generated by nuclear reactions in which muons may incur during their propagation: typically they are produced in the surrounding rock or in the devices which are present inside the laboratory.

Muon induced neutrons can be produced by two different processes [1]:

- **photo-evaporation:**

neutrons are produced by a nucleus after the exchange of a virtual photon with a muon or with a secondary particle produced in the muon cascade: they are almost isotropic and their kinetic energy is low ($E < 50$ MeV);

- **spallation:**

neutrons are produced by the fragmentation of a nucleus scattered inelastically by a muon: their direction distribution is peaked along muon direction and their energy can go up to several GeV.

1.1.1 Energy spectrum

Since the muon flux and the radioactivity intensity in surrounding rocks are dependent on the location of the laboratory, the underground neutron energy spectrum changes from site to site. The energy spectrum is the direct consequence of this two different components: for $E_{neutron} \lesssim 10$ MeV it is dominated by radioactivity neutrons whereas for $E_{neutron} \gtrsim 10$ MeV the muonic component is the only one present.

It is difficult to measure underground neutron energy spectrum because of low energy (for radioactivity neutrons) and low flux ($\Phi(E > 1 \text{ MeV}) \sim 10^{-6} \text{ cm}^{-2} \text{ s}^{-1}$ [2], $\Phi(E > 10$

MeV) $\sim 10^{-9} \text{ cm}^{-2}\text{s}^{-1}$ [1]). Therefore few measurements are present in bibliography [3]-[4] and for many deep underground laboratories only calculated data are available ([1],[2],[5],[6]).

In fig. 2.28 it is shown the calculated energy spectrum for Hall A and Hall C of LNGS underground laboratory [2].

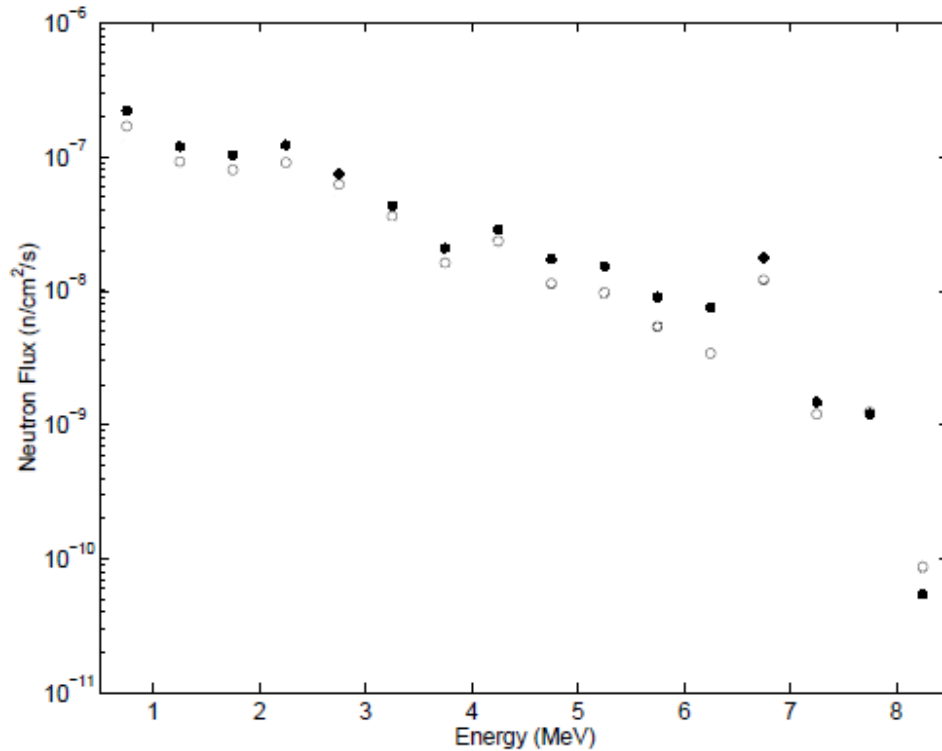


Figure 1.1: Calculated neutron flux at the Gran Sasso laboratory, ●: Hall A ○: Hall C [2]

In both the spectra shown in fig. 2.28 it is possible to note two contributions: the first one ($E < 4 \text{ MeV}$) due to ^{238}U and similar elements fission reactions, the second one ($E > 4 \text{ MeV}$) due to (α, n) reactions. Their direction is expected to be almost isotropic because they are generated almost homogeneously inside the surrounding rock.

Also the muon induced neutron energy spectrum depends on rock chemical composition, but in very faintly way: it depends mainly on the muon energy spectrum which is strictly correlated to the rock overburden depth. The muon induced energy spec-

trum has been simulated, and then fitted, for different underground sites by Mei and Hime [1] and their results are shown in fig.1.2. In fig. 1.2 it is possible to distinguish between “evaporation” and “spallation” neutrons component; it is also possible to note that the shape of the energy spectrum is almost the same for all the underground sites considered. The muon induced neutron direction is expected to be peaked along the primary muon direction with a long tail due to “evaporation” neutrons.

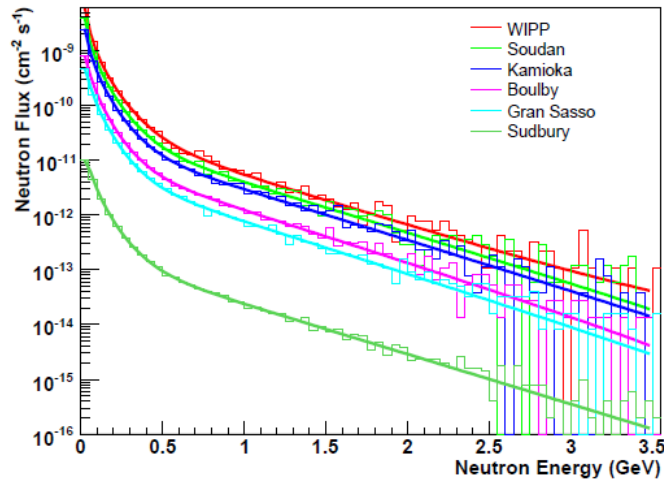


Figure 1.2: Muon induced neutron differential spectrum for different underground sites [1]

1.1.2 Underground neutrons as detector background

Neutrons are a background source for any low-background experiment looking for rare events because they can produce, by direct interaction or by production of secondary particles, signals not discernible from the researched ones. For example, neutrons can mimic the neutrino interaction (see chap. 3), the WIMPs one (see chap. 2), and also the Double Beta Decay signals by $\text{Ge}(n, n'\gamma)$, $\text{Pb}(n, n'\gamma)$ and $\text{Cu}(n, n'\gamma)$ reactions or by producing long-lived radioactive isotopes [1]. It is evident that the neutron background has to be reduced as much as possible.

Even if muon induced neutron total flux is very small if compared to the radioactivity neutron one, muon induced neutrons represent a more difficult problem to be solved. In fact, the amount of radioactivity neutrons produced inside the detector itself can be

reduced by selecting for building the detector materials with low quantity of radioactive isotopes. It is also relatively easy to shield the detector from the environmental radioactivity neutron flux by surrounding it with thick layers of moderator materials: in this way the effective radioactivity neutron flux results considerably lowered. Unfortunately, this is extremely difficult to do for muon induced neutrons because their high energy. Also their tagging in coincidence with the primary muon is difficult (except for neutrons generated inside the detector which can be easily rejected by an efficient external veto): a muon passing very far away from the detector may produce neutrons able to reach the detector because of their long propagation range [1].

1.2 Atmospheric Neutrons

All the neutrons produced by the interactions of galactic and solar cosmic rays in the atmosphere are called “Atmospheric Neutrons”. They are generated in hadronic and electromagnetic air showers by spallation and evaporation processes on nitrogen and oxygen nuclei, which are the predominant elements in the Earth’s atmosphere.

For simple kinematic reasons atmospheric neutrons are produced along the primary cosmic ray direction, i.e. downward, but there is a fraction of them moving upward because of albedo effect.

1.2.1 Altitude neutron flux profile

The flux of atmospheric neutrons grows from the top of the atmosphere downward until a maximum value known as the Pfozter Maximum at $\sim 100 \text{ g cm}^{-2}$, corresponding to an altitude of $\sim 20 \text{ km}$ [11]. Fig. 1.3 shows the altitude dependence of the atmospheric neutrons flux in two energy intervals $0.7 \text{ MeV} < E < 4.5 \text{ MeV}$ and $1 \text{ MeV} < E < 10 \text{ MeV}$, as measured by [12]. The altitude dependence of flux is different for downward and upward moving neutrons. The downward moving neutron flux increases linearly starting from the top of the atmosphere until the Pfozter Maximum and, after that,

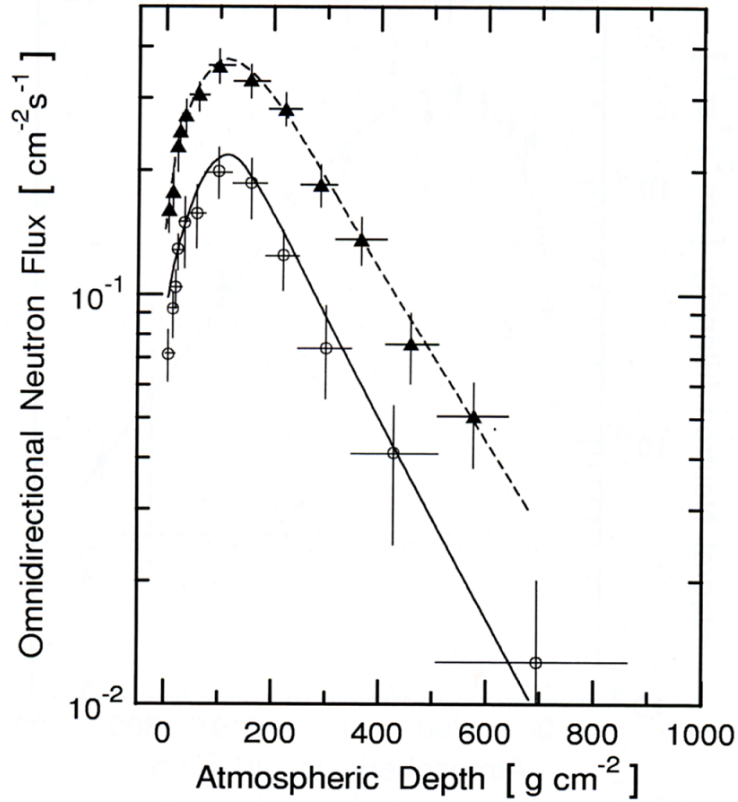


Figure 1.3: Observed altitude dependence of neutron flux for rigidity cutoff= 13.9 GV for energy interval $0.7 \text{ MeV} < E < 4.5 \text{ MeV}$ (black triangles) and $1 \text{ MeV} < E < 10 \text{ MeV}$ (empty circles) together with fitting curves [12]

decreases exponentially until the sea level; also the upward moving neutron flux decreases exponentially from the Pfozter Maximum toward the sea level but, above the Pfozter Maximum remains relatively constant and extends outward to low Earth orbit altitude. As a consequence, at the Pfozter Maximum region the total neutron flux is roughly isotropic [13].

1.2.2 Energy spectrum

The atmospheric neutron energy spectrum is consequence of the two different generation processes. This is clearly visible in the fluence rate per lethargy spectra (lethargy is the natural logarithm of energy: fluence rate per lethargy is equivalent to $E \cdot \frac{d\Phi}{dE}$, E is the particle energy, Φ is the fluence rate) shown in fig. 1.4 where two peaks are

present: the “evaporation” one for energy ~ 1 MeV and the “spallation” one for energy ~ 100 MeV.

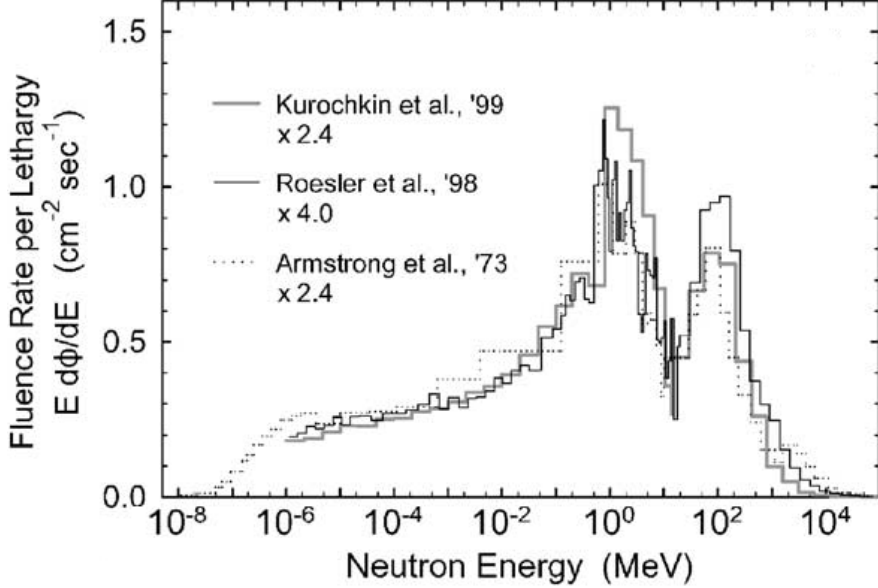


Figure 1.4: Cosmic-ray neutron spectra calculated by [8],[9] and [10], picture taken from [7]

Fig. 1.4 [7] shows the rescaled cosmic-ray neutron spectra calculated by Roesler *et al.* [8], Kurochkin *et al.* [9] and Armstrong *et al.* [10]. These spectra have been rescaled because calculated for different values of atmospheric depth and/or geomagnetic cut-off: Roesler *et al.* computed for an atmospheric depth to 200 g cm^{-2} at 4.3 GV rigidity cutoff, Kurochkin and *et al.* for 200 g cm^{-2} at 2.9 GV and Armstrong *et al.* for 50 g cm^{-2} at 4.6 GV.

Fig. 1.4 shows also that, even if the total fluence rate of atmospheric neutrons changes as a function of geomagnetic cut-off and atmospheric depth, the shape of the spectrum remains almost the same. This statement is confirmed by fig. 1.5 which shows the observed fluence spectra (after re-normalization) at different altitudes [7]. In fig. 1.5 the spectra (rescaled for an easier comparison) show that, by varying only the atmospheric depth, the shape of the observed energy spectrum does not change.

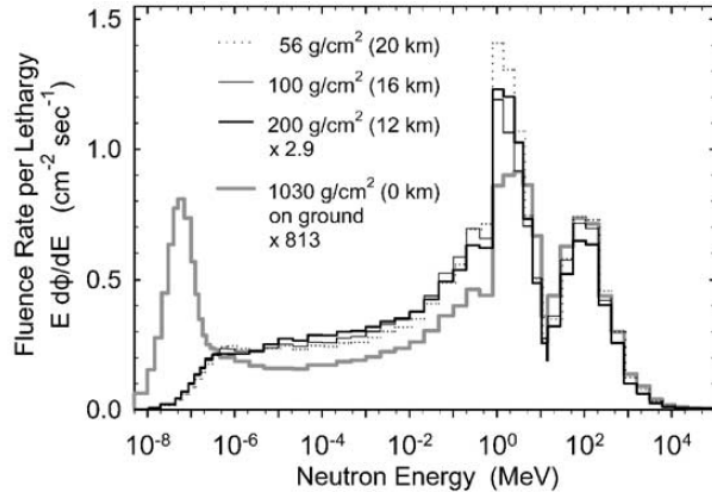


Figure 1.5: Renormalized observed neutron spectra at various altitudes on board of an airplane [7]

This is true until the measurements are performed in atmosphere and not at the ground level. The spectrum collected in fig. 1.5 observed at the ground level compared to the other ones shows two substantial differences:

- 1) there is a third peak for thermal energy due to neutrons produced by the soil;
- 2) the “spallation” peak is higher because soil and air reflect neutrons in different way.

For measurements made at the ground level it is necessary to take into account the “soil effect” and its distortion to the expected energy spectrum.

1.2.3 Solar Neutrons

Solar neutrons are one particular class of atmospheric neutrons. They are emitted almost continuously by the Sun into the interplanetary space but only during large solar flares their kinetic energy is large enough for allowing them to travel up to the Earth before decaying.

Solar flares are explosions which occur in the Sun atmosphere, usually near sunspots. During a solar flare charged particles, mainly electrons and protons plus a little fraction of heavy ions, are accelerated and, if their energy is sufficient, they can produce Coro-

nal Mass Ejections (CME) which are responsible of Northern and Southern Lights and sometimes of troubles for radio transmission, for satellites, and electrical transmissions lines.

During their emission, ions can interact with the solar atmosphere producing high energy neutrons. These neutrons arriving to the Earth carry informations on the acceleration because they are not affected by any magnetic fields along their path: by observing solar neutrons it is possible to determine the primary ions energy spectrum and time of their acceleration [18].

Solar flare frequency, which is larger during solar maximum activity, is roughly proportional to the inverse of the total emitted energy: flares producing neutrons able to reach the Earth are quite rare, ~ 1 event year⁻¹ (see fig. 1.9).

The detection of solar neutrons is difficult because almost half of them will decay during the transit time between the Sun and the Earth (the surviving probability is function of neutron kinetic energy) and, furthermore, the survived neutrons are strongly attenuated in the Earth's atmosphere [19] ($\lambda = 110$ g cm⁻², by measurement of neutron cross-section scattering in carbon [20]). Therefore in order to reduce as much as possible the thickness of crossed atmosphere, solar flares neutrons have to be observed by detectors installed at high altitude or, better, on board spacecrafts.

There are two classes of detector for solar neutron observation at ground level:

Neutron Monitors (NMs): they are constituted by a lead target, for multiplying the number of neutrons, sheets of paraffin or polyethylene, for thermalizing neutrons, and proportional counters filled with ¹⁰B or ³He gas for detecting the thermalized neutrons. Their main goal is to study variation of cosmic rays flux [19] which can be due to the periodic solar modulation or to the "Forbush Decrease" (FD). FD is the dramatic attenuation of the flux of the Galactic Cosmic Rays (GCR), measured by particle detectors on the Earth and in the interplanetary space, during and after passage of an Interplanetary CME which works as a magnetic shield for lowest energy GCR. FD takes place in the course of a few hours and over the following several days the GCR intensity returns to pre-FD value [21]. In fig. 1.6 are shown the hourly data

for Thule (Greenland, TH) and McMurdo (Antarctica, MM) NMs for the period 23-25 March 1991 during which a large FD took place [22];

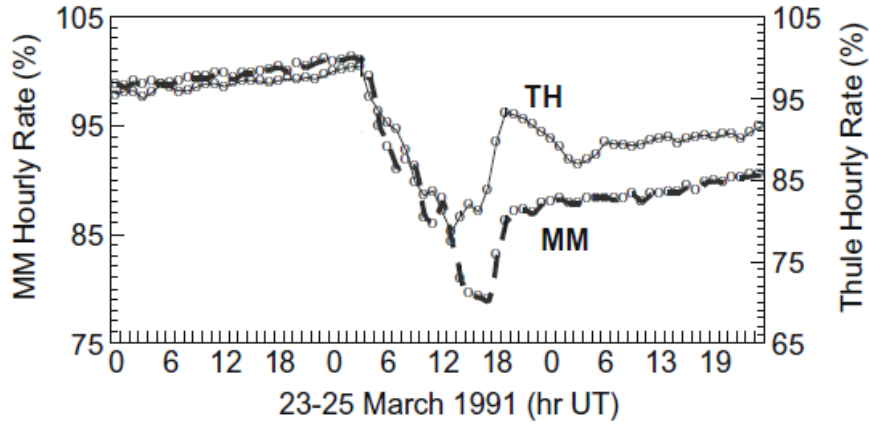


Figure 1.6: NM data (hourly pressure corrected and normalized to annual means) for Thule (TH) and McMurdo (MM) for the period 23-25 March 1991 [22]

For this purpose good energy resolution is not requested and so they are not able to give any information about neutrons direction and energy[18]: during a solar flare the neutrons energy can be only extrapolated by their arrival time distribution.

Solar Neutron Telescopes (SNTs): they are made by one (or more than one) scintillator detector surrounded by an iron/lead shield and a veto composed by proportional counters. In the scintillator detector neutrons are converted into protons: the energy of neutrons is measured by the energy of recoiling protons while their direction by the proportional counter placed under it [19] (see fig. 1.7 as example). Since SNTs are able to give information about neutron arrival time, energy and direction, they are the best detectors for solar neutrons observation.

During solar flares, neutrons are supposed to be emitted impulsively (~ 1 min) according to a power law

$$\Phi(E) \propto E^{-\gamma}$$

where $\gamma= 3-4$ (see fig. 1.9) but their arrival time at Earth is spread over a time span of 20 min due to the different times of flight. Other neutron emission models cannot be

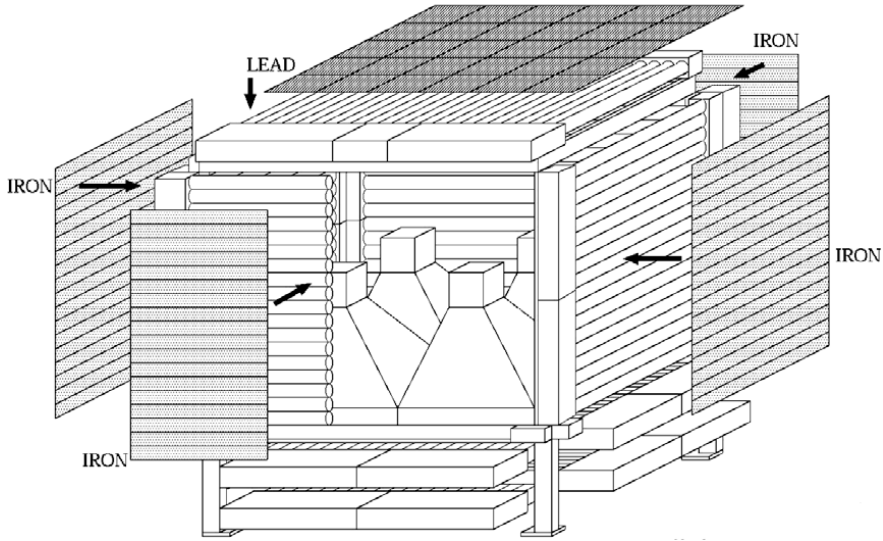


Figure 1.7: The Solar Neutron Telescope at the summit of the Sierra Negra volcano, Mexico, at 97.3W, 19.0N; 4580 m a.s.l. [19]

completely excluded because most of recorded events have been observed only by NM and, in the few cases SNT data are present, they are not exhaustive. Models predicting a high energy ($E \gtrsim 1$ GeV) constant emission are still valid, whereas for very large solar flares a long-standing power law emission is still possible [18].

In fig. 1.8 it is shown the energy distribution of neutrons emitted during the solar flare occurred on November 2, 2003 obtained by assuming the impulsive neutron emission model [23].

In fig.1.9 the distribution of the power index γ of solar flare neutrons emission ($E_n = 70\text{-}700$ MeV) for events recorded up to September 2005 is shown (the spectral index has been computed by assuming the impulsive neutron emission model).

Further detections of solar flare neutrons are requested. Also X and γ -rays observations could be of some help to solve the question about neutrons emission time and energy spectrum. In fact, X and γ -rays, which are emitted during the flare acceleration phase on the solar atmosphere by particle interactions and by bremsstrahlung emission of accelerated electrons, arrive to the Earth without suffering any delay. The princi-

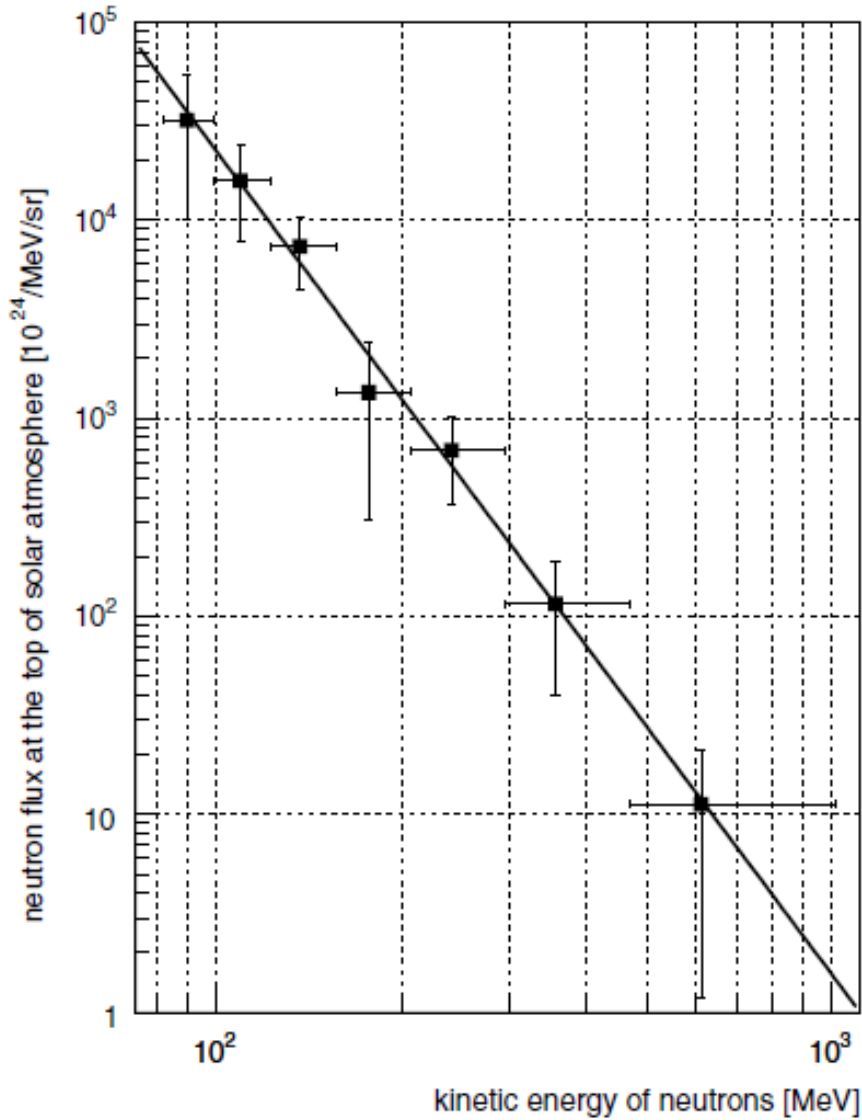


Figure 1.8: Energy spectrum of solar neutrons on the solar surface for the flare which occurred on November 4, 2003, together power law fit ($\gamma= 4.2$)[23]

pal observed γ -rays lines are the neutral pion decay one ($E_\gamma \sim 70$ MeV), the nuclear de-excitation ones from Carbon ($E_\gamma \sim 4.4$ MeV) and from Oxygen ($E_\gamma \sim 6.1$ MeV) and the one of neutron capture on Hydrogen ($E_\gamma \sim 2.2$ MeV)[18].

1.2.4 Atmospheric neutrons and electronic devices

For electronic devices neutrons in the 10-200 MeV energy range are among the most problematic of cosmic-ray secondary particles.

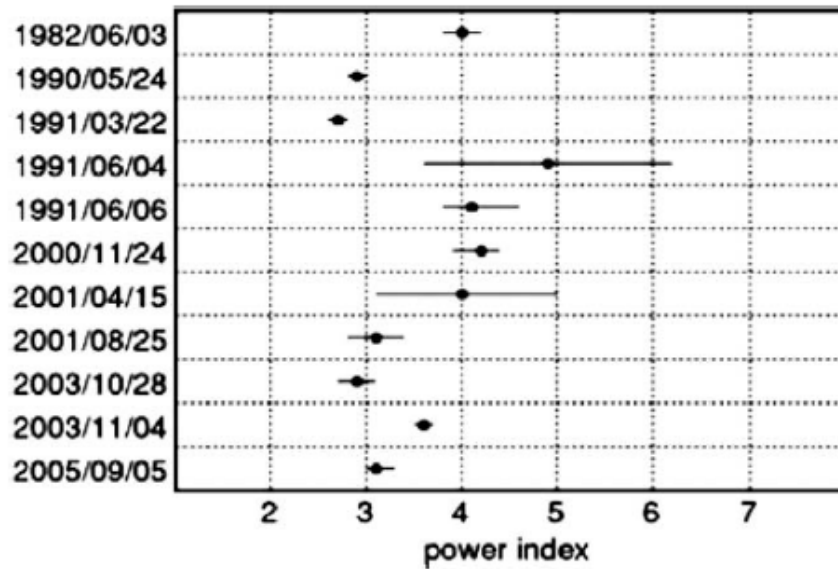


Figure 1.9: The estimated spectral indexes of solar neutron events detected by neutron monitors with energy range around $E_n = 70\text{-}700$ MeV [18]

In fact, they can incur in the $^{28}\text{Si}(n,n'\alpha)^{24}\text{Mg}$ reaction which produce an energetic, heavily ionizing α particle which may change the state of a solid state junction. This will produce a Single Event Upset (SEU), i.e. a nondestructive circuit failure. With the downsizing and the correlated increasing density of modern circuitry, the potential damaging effects due to cosmic radiation increases. A possible solution may consist on an enlarged fraction of error-correction channels inside new circuitry but this would involve a decreased miniaturization potential of electronic chips [14]. Cosmic radiation induced SUE have already been observed in systems with large allocations of random access memory (RAM) [7] and it could become serious in particular for devices installed on airplanes or space ships.

1.2.5 Atmospheric neutrons and human health

The cosmic radiation is not only dangerous for electronic devices but also for the human health. It is well known that the most efficient way for absorbing neutron energy is the elastic scattering with a free protons. The human body is made up by more than

70% of water plus a smaller quantity of fats and carbohydrates: this makes the human body a very good neutron absorber.

As a consequence, atmospheric neutrons can produce damaging effect in particular on commercial flight crews (the standard commercial aviation altitude is ~ 10 km, close to the Pfozter Maximum) and on astronauts during their long-term missions on board ISS (International Space Station).

In the past fifteen years several studies have been performed for understanding this matter [7],[8],[9],[15]. It has been estimated that, at aviation altitudes, the neutron component of the secondary cosmic radiation contributes about half of the dose equivalent but, unfortunately, it was not possible to calculate or measure accurately the cosmic-ray neutron spectrum in the atmosphere and, consequently, to determine the dosimetry [7],[8],[9].

1.2.6 Atmospheric neutrons as detector background

At ground level atmospheric neutrons are one of the most important background components for surface detectors like antineutrino detectors (see chap. 3) for nuclear power plant activity supervision and SNM (Special Nuclear Material) detectors for cargo container inspection [13].

The antineutrino detection may be used for monitoring the activity of nuclear power plants and in particular for detecting illicit or suspicious uses of these facilities. The International Atomic Energy Agency is spending several efforts to develop new technologies to monitor nuclear activity on power plants, aiming at the verification of non-proliferation safeguards. The advantages of using $\bar{\nu}_e$ for reactor safeguards and monitoring include the availability of real time information on the status of the core, less intrusiveness, and simplified operations from the standpoint of both the reactor operator and the safeguards agency [16].

Such $\bar{\nu}_e$ detector should be placed very close to the reactor core in order to have suitable statistics; it should be also small (~ 1 m³) and not overburdened, because price and

logistical reasons, and thereby it would be very poorly sheltered from cosmic radiation. Neutrons can easily mimic the Inverse Beta Decay (IBD) reaction, which is the main one for $\bar{\nu}_e$ detectors, and the only chance for disentangling neutron signals from IBD ones consists on “pulse-shape” technique (see chap. 3). The efficiency of this technique varies from detector to detector but, in any case, for neutrino detectors the atmospheric neutron flux has to be reduced as much as possible.

Neutrons are used for SNM detection because, unlike other forms of radiation produced by SNM, they are produced by a copious and penetrating emission in the MeV energy range: such a detection would provide an unambiguous proof of the presence of illegal fissionable material [13]. Consequently, the development of SNM detection techniques based on neutron imaging nowadays is one of the highest priority R&D areas in the application of nuclear science to world security [13]. To effectively design instrumentation to scan for illicit amounts of SNM, the flux of background neutrons at the search site must be known accurately, including the shape and any major features in the energy spectrum, as well as the zenith and azimuth angle dependences [17].

Chapter 2

Underground neutrons

In this chapter I report the results of a Monte Carlo Geant4 simulation code for studying LVD as a detector for muon induced neutrons and as moderator for neutrons produced by natural radioactivity. The work was aimed to estimate the neutron flux inside the LVD central part where a new generation Dark Matter experiment could be housed.

2.1 The Dark Matter problem

Since the first measurement of galaxies motion in Coma cluster by Zwicky in 1933 up to the latter measurement of Cosmic Microwave Background Radiation performed by WMAP collaboration, several evidences about the existence of a large quantity of mass besides the ordinary one have been collected. Since the ordinary mass is estimated very well by optical observations, that amount of mass not emitting light has been called “Dark Matter”. The first hypotheses were for an astrophysical or cosmological solution of the problem, i.e. galactic dust, black holes, brown dwarves, MaCHOs (Massive Compact Halo Objects) and Big Bang relic neutrinos, but all of these have been rejected by experimental astronomical observations (infrared, X-rays, gravitational lensing) or by laboratory measurements of neutrino mass (actual upper limit is $m(\nu_e) < 2$ eV C.L. 95% [24], [25]). Nowadays the research is focused on an exotic solution like sterile neutrinos, axions, WIMPs (Weakly Interacting Massive Particles),

etc. . . which should exist in a spherically-symmetric distribution in the galaxy, making up a Dark Matter cloud through which the Solar System, and hence the Earth, moves. Occasionally a Dark Matter particle would experience a collision with an atomic nucleus of an Earth-based detector while the Earth is passing through the WIMP wind: this would lead to a detectable signal.

The biggest problem of such approach is that experiments have been designed to detect particles whose there is no experimental evidence of their existence. As a consequence, the uncertainties about their interaction modes are very large.

The baryonic mass density in the Universe is estimated equal to $\sim 5\%$ of the total energy density, the non-baryonic one is estimated $\sim 23\%$ whereas the rest is estimated to be “Dark Energy” [26].

Up today only the DAMA-NaI experiment, and its evolution DAMA-Libra, claimed for Dark Matter detection [27] but its results are difficultly in agreement with the null results obtained by other experiments (like Xenon, EDELWEISS and CDMS) as discussed in the next paragraph.

2.1.1 The DAMA results

The experiment DAMA-Libra (Large sodium Iodide Bulk for RAre processes) is the evolution of the DAMA-NaI experiments.

The active mass is formed by ~ 250 Kg of highly radiopure NaI(Tl) scintillator subdivided in 25 independent detectors, placed on a 5 x 5 matrix, each one with 9.70 kg active mass monitored by two photomultiplier tubes. The threshold of each one of the two photomultiplier tubes (pmts) on a module is set at single photoelectron level; their coincidence provides the trigger of the detector, whereas the software energy threshold has been cautiously taken at 2 keV electron equivalent [27]. The entire apparatus is shielded from the environmental radioactivity by layers of Cu, Pb, Cd-foils, polyethylene and paraffin. The whole set-up is maintained at a constant temperature and monitored continuously.

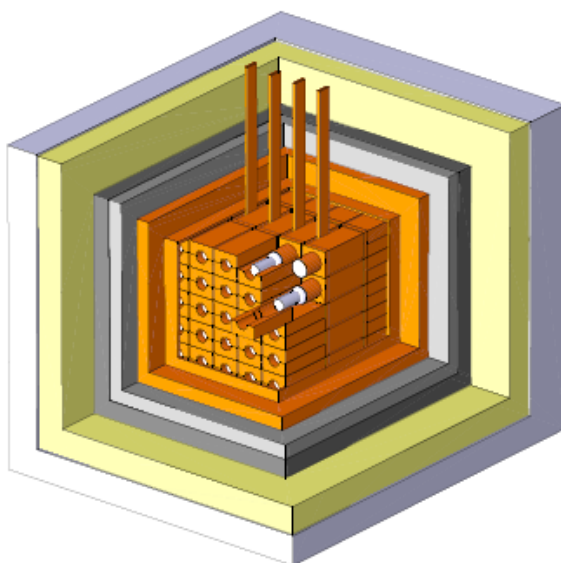


Figure 2.1: Scheme of DAMA-Libra detector [36]

The goal of DAMA-NaI and DAMA-Libra experiments was to detect Dark Matter by finding annual modulation of interaction rate of Dark Matter particles due to the Earth's revolution motion around the Sun. In fact, the sum of this motion and the Sun's one around the galactic center is expected to give out an annual modulation of the speed of Dark Matter particles observable at Earth and, as a consequence, an annual modulation of their flux. Thus the Dark Matter particles counting rate, in a particular energy interval, has to be modulated like

$$S = S_0 + S_m \cos \omega(t - t_0)$$

where S_0 is the constant part of the signal, S_m is the modulation amplitude, $\omega = \frac{2\pi}{T}$ with period T , and t_0 is the phase.

The residual rate of events is defined as

$$\langle r_{ik} - flat_k \rangle_k$$

where r_{ik} is the rate in the i^{th} time interval in the k^{th} energy bin and $flat_k$ is the average rate in the k^{th} energy bin computed over the all data acquisition cycles [27].

In particular, the maximum value of this flux should be reached around roughly June 2nd and the minimum value around roughly December 2nd (see fig. 2.2) [27]. This technique has the advantage to be independent to the various theoretical models predicting Dark Matter particle features and Dark Matter distribution inside the Milky Way Galaxy.

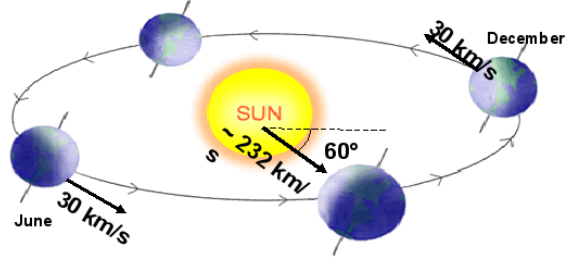


Figure 2.2: Annual Earth motion around the galactic center

The DAMA-NaI detector collected data from January 1996 until July 2002 during seven annual cycles whereas the DAMA-Libra detector, whose detector apparatus is described in the next paragraph, collected data from September 2003 until July 2007 during four annual cycles: for the first experiment the total active mass was 87.3 Kg, corresponding to a total exposure equal to 0.29 ton x year, while for the second one the active mass was 232.8 Kg, corresponding to a total exposure equal to 0.53 ton x year.

The time distribution of residual counting rate observed by DAMA experiments in the energy range $2 \text{ KeV} < E_{vis} < 6 \text{ KeV}$ (KeV electron equivalent, i.e. the visible energy released by a 1 KeV electron) is shown in fig. 2.3 together with a cosinusoidal fit (period $T = 1$ year, phase $t_0 = 152.5$ days)

The confidence level of the fitted curves for only DAMA-NaI and DAMA-Libra data is equal to 8.2σ , while it is equal to 6.3σ considering only DAMA-NaI data and 5.6σ considering only DAMA-Libra data [27].

It is important to note that the modulation of residual rate disappears for energy above 6 KeV as shown in fig. 2.4-2.5 in agreement with the expectation about Dark Matter

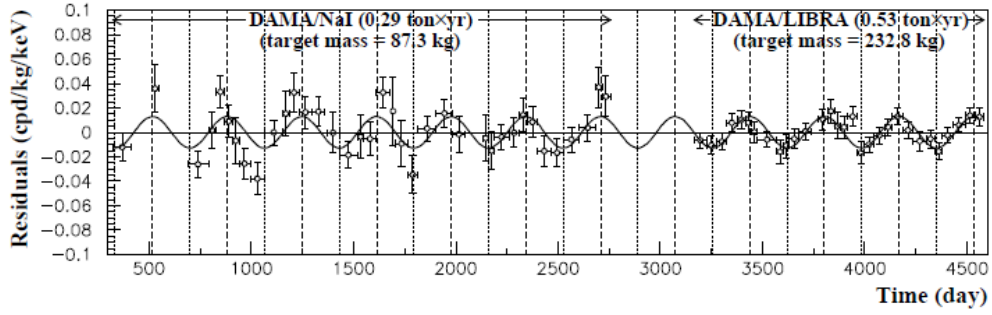


Figure 2.3: Residual rate of events as a function of time modulation in the 2-6 KeVee intervals as measured by the DAMA-NaI and the DAMA-Libra experiments. The plotted point are fitted with a cosinusoidal curve with annual period. The zero of the time scale is January 1st 1996, the first year of data taking of the DAMA-NaI experiment [27]

particles interaction.

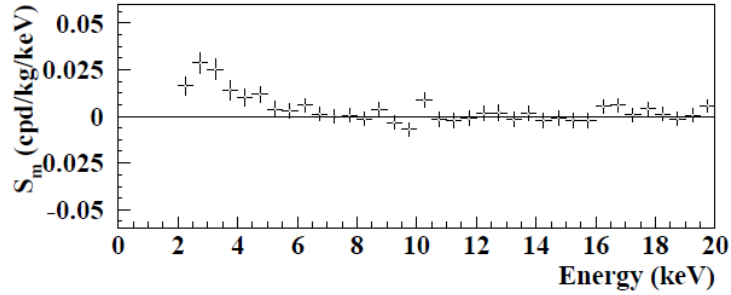


Figure 2.4: Residual rate of single-hit events collected in a single annual cycle for the total exposure DAMA-NaI and DAMA-LIBRA (0.82 ton x year) [27]

The results are a strong indication toward identification of Dark Matter existence and they are not directly comparable with other ones which have been obtained by different techniques [27]. In order to compare this result with other ones, several *a priori* assumptions are needed about Dark Matter particles mass, their interaction mode and cross section, about quenching (i.e. the ratio between the observed energy and the released one; it is due to saturation effects of scintillator light yield) and channeling effect in NaI(Tl) scintillator and about Dark Matter space of phases distribution.

The usual assumptions consist on:

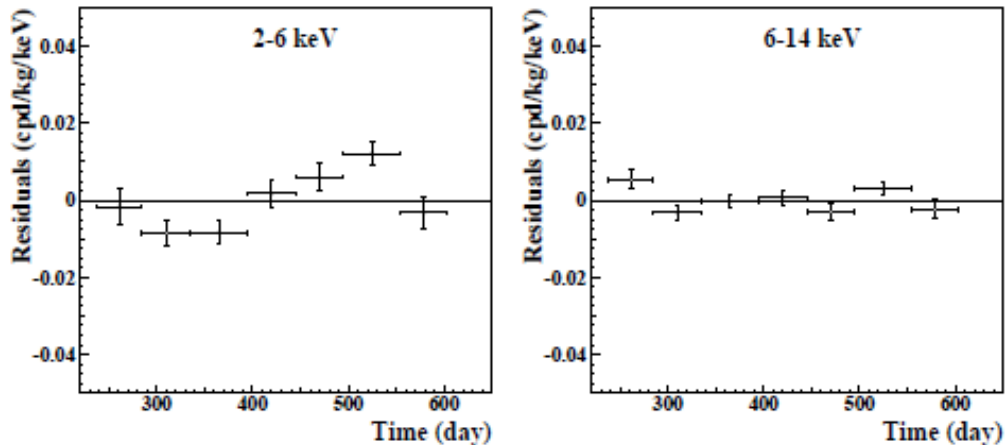


Figure 2.5: Modulation amplitude S_m for the total exposure, DAMA/NaI and DAMA/LIBRA (0.82 ton x year), in the energy range 2-6 KeVee (at left) and 6-14 KeVee (at right) [27]

- Dark Matter formed by WIMPs with elastic spin-independent cross section;
- Dark Matter velocity distribution in the galactic rest frame described the Standard Halo Model (SHM).

SHM assumes that in the galactic frame the WIMPs distribution is an isotropic isothermal sphere: this leads to an essentially structureless isotropic Maxwell-Boltzmann velocity distribution with dispersion set by the local circular velocity [28].

Under this assumption DAMA results are in large disagreement with the null results obtained by other experiments, CDMS and Xenon10 in particular (see fig.2.6).

The solution to this problem, without rejecting any result, may consist on modifying the preliminary assumptions, in particular about WIMPs interaction mode and their distribution in the galactic frame.

For WIMPs interaction it has been suggested a spin dependence of WIMPs cross section and different WIMPs cross section values for protons and neutrons. It has also been hypothesized an inelastic interaction (iDM) instead of elastic one (DM) [30]: in the iDM scenario, WIMP-nucleon elastic scattering is suppressed, while inelastic scattering from a ground-state WIMP to a slightly higher mass excited WIMP ($\delta \sim 100$ KeV) is allowed and dominates the recoil event rate. The first hypothesis do not solve the

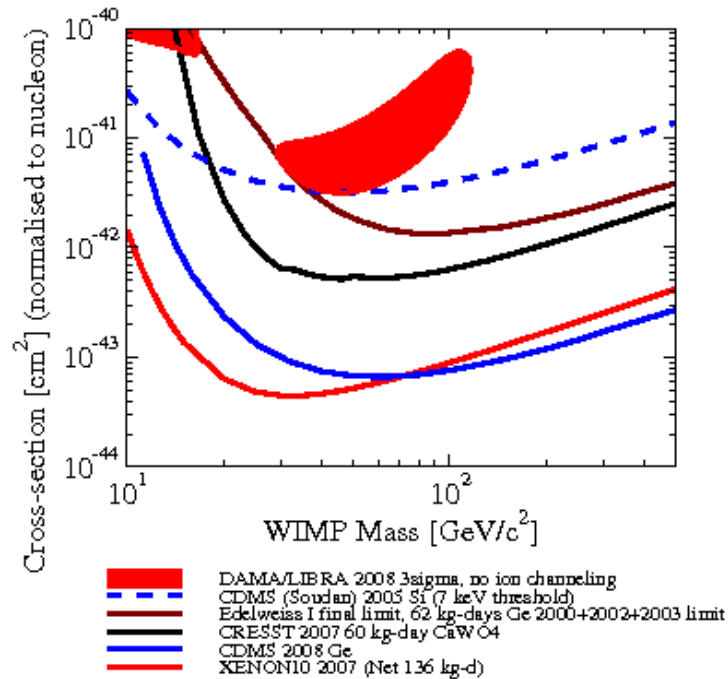


Figure 2.6: Spin Independent Cross Section *vs.* WIMP Mass, DAMA 3σ boundary region together with Xenon10, CDMS, CRESST and Edelweiss upper limits [29]

incompatibility of DAMA results except for WIMPs mass below about 5 GeV (see fig. 2.7), while the iDM scenario can bring the DAMA results closer to agreement with the other experiments, but the parameter region allowed by DAMA and other experiments still remains strictly constrained [28] (see fig. 2.8).

In fig. 2.8 are shown the exclusion limit regions given by all the past null experiments together with the DAMA allowed region (C.L. 90% and 99.5%). These regions have been computed under the hypothesis of iDM, SHM and WIMP mass equal to 80, 100, 200 and 1000 GeV.

For WIMPs distribution new models are coming out from *N-body* numerical simulations (e.g. *Via Lactea* [31], *Dark Disc* [32]). These simulations, starting from a homogeneous distribution plus quantum oscillations of Dark Matter density (plus baryons, if considered), are aimed to study the actual Dark Matter distribution inside

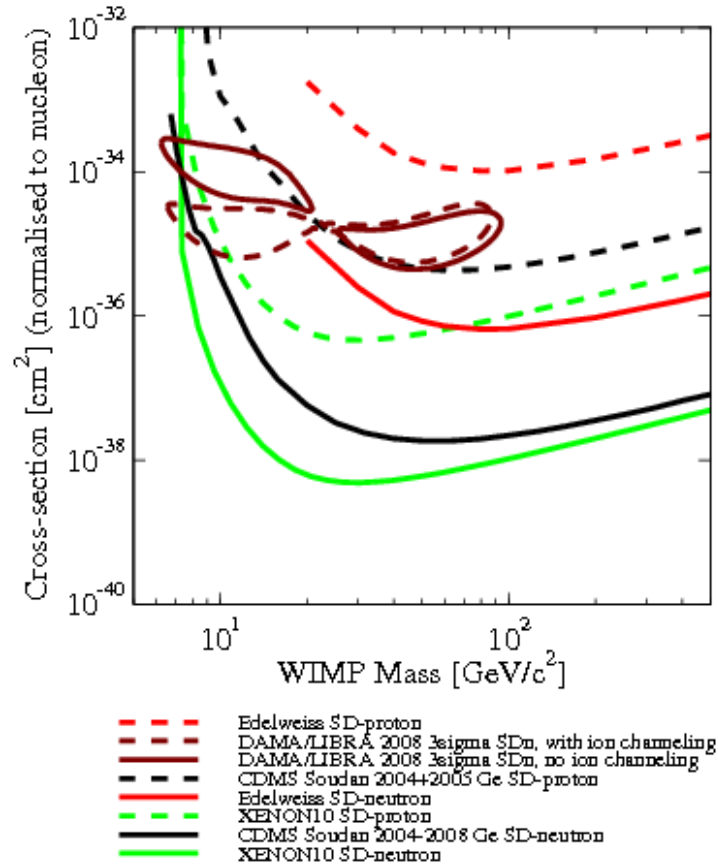


Figure 2.7: Spin Dependent Cross Section *vs.* WIMP Mass for neutrons (continuous lines) and protons (dashed lines), 3σ DAMA boundary region results together with Xenon10, CDMS, CRESST and Edelweiss upper limits [29]

a Milky-Way like galaxy by following “step-by-step” its formation. Their results are quite different because the different initial hypothesis and resolution, nevertheless all of them exclude a structureless isotropic Maxwell-Boltzmann velocity distribution: *Via Lactea* predicts a very clumpy Dark Matter distribution whereas *Dark Disc* predicts the presence of an additional Dark Matter disc due to tidal effects on massive satellites when they cross the galactic plane [28]. By combining the iDM scenario with a modified WIMPs distribution model it is possible to increase noticeably the agreement between DAMA and other experiments results as shown in fig. 2.9.

Fig. 2.9 shows the exclusion limit regions given by all the past null experiments

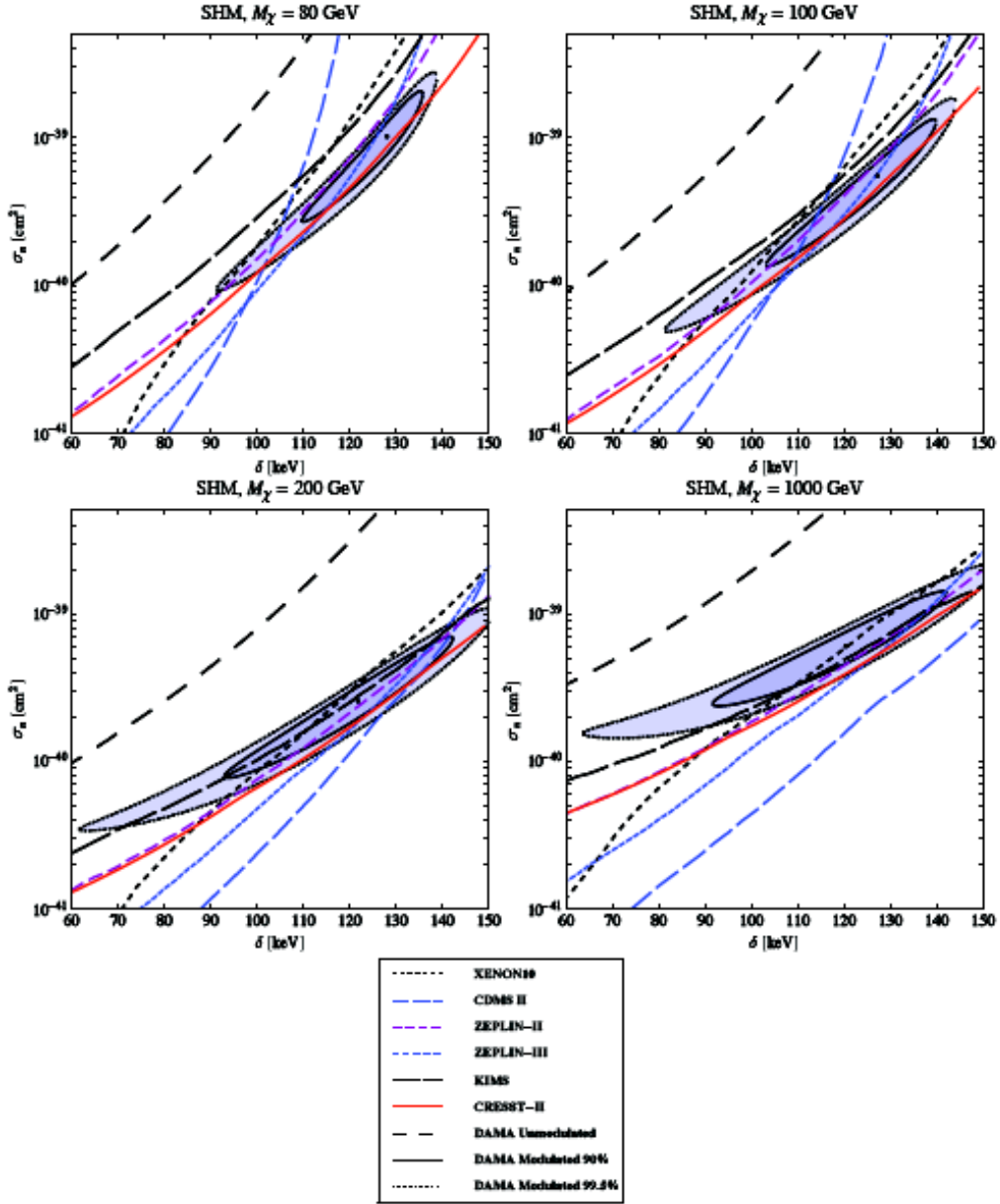


Figure 2.8: Exclusion limit regions σ_n vs. δ for iDM obtained by assuming M_χ equal to 80, 100, 200 and 1000 GeV and SHM. DAMA best fit point is plotted with a dot together C.L. 90% and 99.5% boundary regions [28]

together with the DAMA allowed region (C.L. 90% and 99.5%) by assuming SHM or *Via Lactea* WIMPs distribution.

It is evident that the problem is still far to be solved and that several efforts are

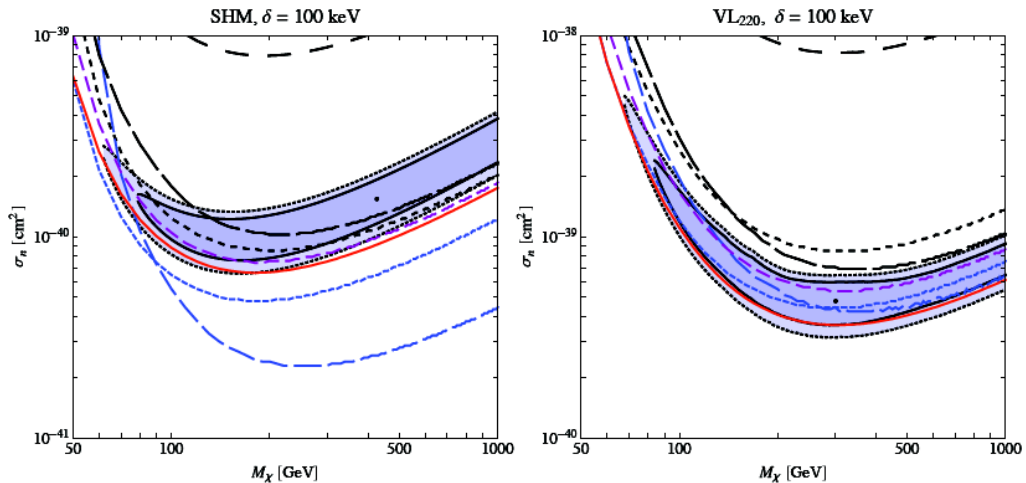


Figure 2.9: iDM Cross Section *vs.* WIMP Mass allowed region for fixed $\delta = 100$ KeV assuming the SHM (left panel) and assuming *Via Lactea* (right panel). DAMA best fit point is plotted with a dot together C.L. 90% and 99.5% boundary regions, together with CRESST (red line), ZEPLIN II and III (violet and blue dotted line), KIMS (black dashed line), CDMS-II (blue dashed line) and Xenon10 (black dotted line) upper limits [28]

necessary for getting more precise *N-body* simulations about WIMPs distribution and theoretical models about their interaction. Also, new unambiguous experimental data are necessary in order to confirm or reject the DAMA results.

2.1.2 The Gran Sasso Laboratories and Experiment for the search of Dark Matter

The *Laboratori Nazionali del Gran Sasso* (LNGS) are located in the center of Italy, 20 Km far away from the city of L'Aquila under the namesake mountain which is part of Gran Sasso massif. The underground laboratories have been realized alongside of the highway tunnel which connects L'Aquila to Teramo and they are placed at the equivalent vertical depth of 3.1 km of equivalent water, relative to a flat overburden. Thanks to the deep underground location, which offers a powerful shielding for cosmic rays and in particular for muons (the muon flux is $\sim 1 \text{ event } m^{-2} s^{-1}$ [35]), and to the large amount of limestone (CaCO_3) inside the overburdening rock: this has a very low natural radioactivity and it makes the LNGS underground site an optimal location for

very low background experiments, like neutrino and Dark Matter experiments. Nowadays several Dark Matter experiments are present inside the the LNGS underground site and they are here briefly described.

DAMA-Libra

DAMA-Libra experiment is described in previous sec. 2.1.1.

CRESST-II

Cresst-II is the last evolution of the Cresst (Cryogenic Rare Event Search with Superconducting Thermometers) experiment.

It is a double-phase cryogenic bolometric modular apparatus for detection of WIMP elastic scattering on heavy nuclei: each module is formed by a highly reflecting cavity containing one 300 g crystal of CaWO_4 and two cryogenic calorimeters. The CaWO_4 crystal, in case of recoiling nucleus, emits both heat in the form of phonons and scintillation light: the first ones are detected by the cryogenic calorimeter kept in touch with the crystal, while the the scintillation light, collected by a light absorber, is detected by the other calorimeter. The double signal allows a highly efficient suppression of background [37].

In order to have a hardware threshold equal to 5 KeV [38], the working temperature of Cresst II apparatus is kept below 10 mK by a $^3\text{He}/^4\text{He}$ dilution refrigerator. Nowadays it is formed by 17 modules and in its last configuration it will consist on 33 modules, reaching up to 10kg of active target mass.

WARP

Warp (Wimp ARgon Program) is a two-phase experiment looking for nuclear recoils.

The active mass of the detector is formed by ~ 100 liters of Argon maintained at cryogenic temperature in order to have the noble gas both in liquid and in the gas phase: this permits the simultaneous detection of both ionization and scintillation. In fact, the impinging particle produce a prompt primary scintillation signal in the

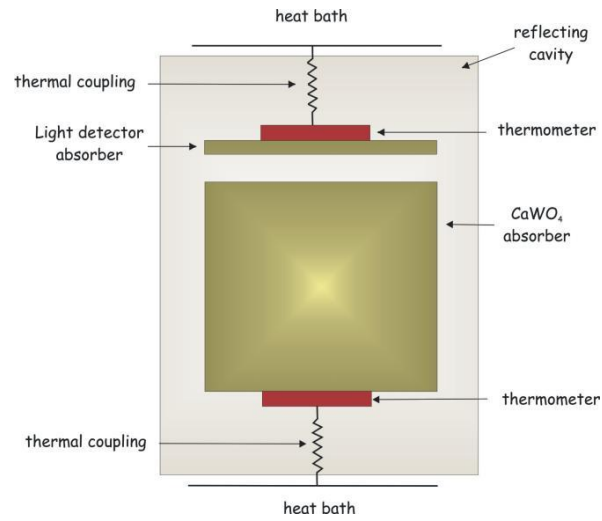


Figure 2.10: Scheme of one Cresst-II module [37]

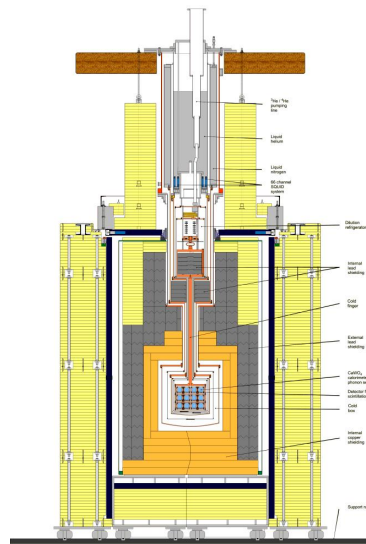


Figure 2.11: Scheme of Cresst-II cryostat [37]

liquid Argon due to de-excitation of argon excited dimers and this signal is detected by the photomultiplier tubes matrix positioned in the gaseous phase. By applying an opportune electric field a bunch of ionization electrons, which have been produced in the interaction and survived recombination processes, is drifted toward liquid-gas interface and extracted to gas. Once extracted they are accelerated in order to produce, through collisions with atoms, the emission of photons. This light signal, proportional

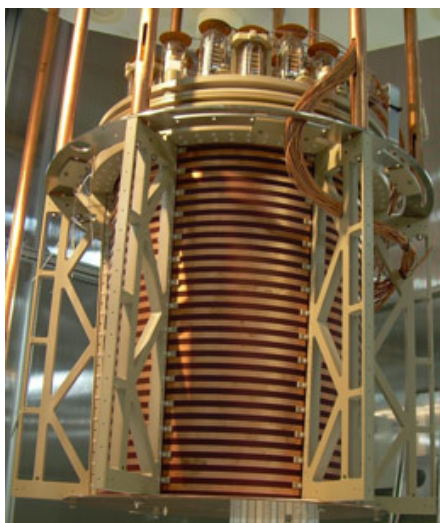


Figure 2.12: Picture of Warp detector [39]

to ionization, is called secondary scintillation or proportional light.

The ratio of primary over secondary signal depends on the kind of particles pro-

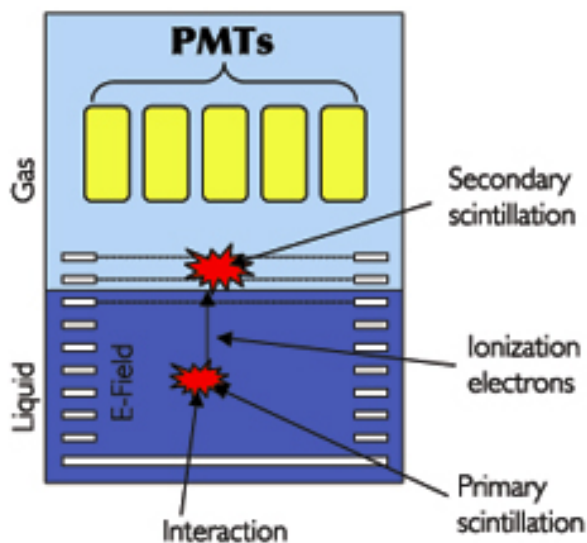


Figure 2.13: Scheme of Warp detector working way [40]

ducing excitation and ionization because of the different recombination probability of ionization electrons. For the same reason also the shape of the primary signal strictly depends on the impinging particle type and it is a powerful tool for discriminating the nature of the ionizing particle. The Warp energy ranges from 10 to 100 keV: in

this range the substantial background induced by gammas and electrons is strongly suppressed by the proposed techniques that are used as discrimination method. A first test measurement on a 2.3 litres test detector has been performed [41] and, nowadays, the 100 litres detector is in the filling phase and it will be ready very soon for data taking.

XENON100

The XENON100 detector is a two-phase (liquid/gas) time projection chamber (TPC) which measures simultaneously the ionization and scintillation signal produced by a Xe nuclear recoil: it is the evolution of XENON10 experiment which was operating between 2005 and 2007 achieving some of the best upper limits for WIMP-nucleon couplings (see fig.2.6). The detector is filled with ~ 170 Kg of liquid Xe which, thanks to its high density ($\rho \sim 3 \text{ g cm}^{-3}$), permits to construct compact detectors, where the outer part shields the inner part very efficiently (self-shielding): the total target mass is ~ 70 Kg of liquid Xe.

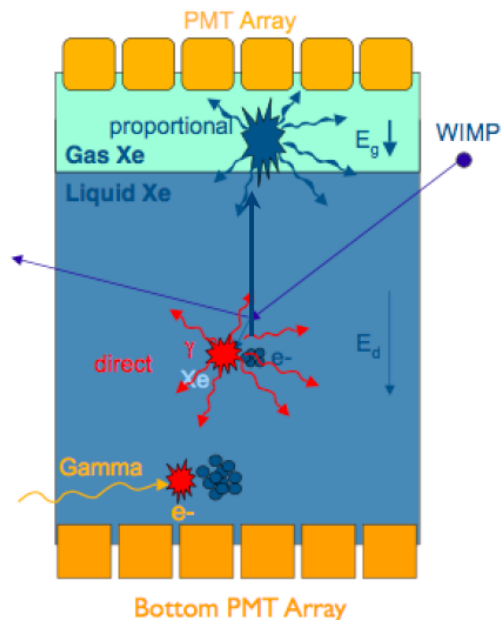


Figure 2.14: Scheme of XENON100 detector working principle [39]

Like for Warp detector, the distinct ratio of the two signals for nuclear recoil events (from Dark Matter WIMPs and neutrons) and for electron-like events (from dominant gamma-rays background) allows for an event-by-event discrimination between signal and background.



Figure 2.15: XENON100 detector [42]

2.1.3 Neutrons as ultimate background for Dark Matter experiments

In the previous paragraph it is clearly shown that almost all the Dark Matter experiments present in the LNGS underground site are looking for nuclear recoil due to WIMP elastic scattering (the only exception is the DAMA experiment which is able to observe light particles besides heavier ones like WIMPs). The worst background component for a such reaction is due to neutrons and their elastic scattering on detector nuclei: this is the same reaction expected for detecting Dark Matter particles. There is no possibility to disentangle between nuclear recoils due to WIMPs from the ones due to neutrons. The only possibility for removing neutrons from WIMP candidates is the “single-hit” technique which consists on selecting events for which only one recoiling

nucleus is present: in fact the probability of a double scattering for WIMPs is risible but it is not for neutrons. The efficiency of this rejection technique, which depends on the detector spatial resolution, is larger as the detector active mass is bigger.

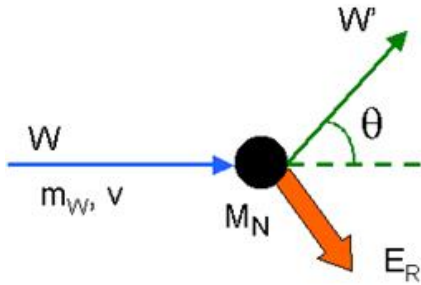


Figure 2.16: WIMP elastic scattering

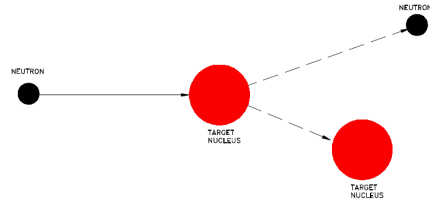


Figure 2.17: Neutron elastic Scattering

Furthermore, it is difficult to shield a detector from neutrons: it is necessary to surround the detector by a moderator material shell which has to be larger as the detector active mass is bigger and thicker as the neutron energy is higher. The energy of underground neutrons, which are divided into radioactivity and muon induced neutrons (see chap. 1), range from thermal energy (~ 26 meV) up to several GeV.

Moderators are all the materials with a large quantity of free protons, like polyethylene, water, paraffin, etc. . . which are able to slow down or stop neutrons. In fact, for simply kinematic reason, the mean kinetic energy released by a neutron to a nucleus after an elastic scattering is as higher as the atomic mass number is lower.

It is evident that the location for a Dark Matter experiment is as better as the neutron background is lower or, as an alternative, a good neutron veto-shielding system has to be present.

2.2 The Large Volume Detector

2.2.1 The detector

The LVD (Large Volume Detector) is a modular experiment located inside the Hall A of LNGS underground site. Its main goal is the detection of $\bar{\nu}_e$ bursts from stellar gravitational collapses. The total active mass, which is ~ 1 KTon, is arranged on an array of 105 modules, each of them formed by 8 counters, placed on 3 towers, 5 columns and 7 levels. Formerly, every module was equipped by two streamer tubes for tracking muons but they were switched-off in 2001 for safety reasons.

Over the seventh level of the second, third and fourth column there is one additional switched-off module (the modules are overall 114). Below the first level a 10 cm thick Boron-paraffin layer is placed for shielding the experiment from Hall A natural radioactivity (neutrons in particular). The aim of a such modular geometry, which involves a lower energy resolution of detected events and a higher background (and consequently a lower sensitivity), is to maximize the duty cycle. In fact, $\bar{\nu}_e$ bursts due gravitational collapse are very rare (2 ± 1 events century $^{-1}$) and very brief ($\Delta t \sim 10$ s) events.

In fig. 2.18-2.19 it is shown the LVD detector (front view) and a single module; while in fig. 2.20 the LVD scheme (active modules only) is described.

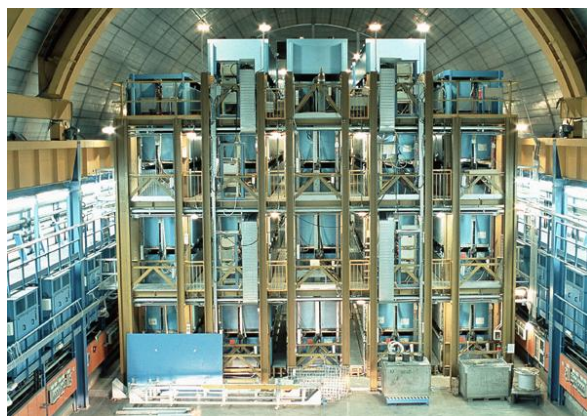


Figure 2.18: The LVD detector, front view



Figure 2.19: A LVD module

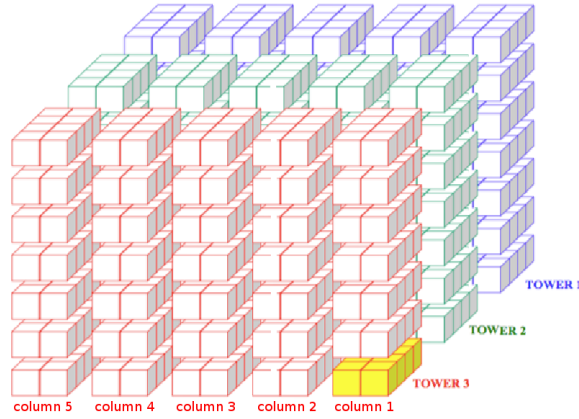


Figure 2.20: Scheme of the LVD detector, switched-on modules only

Each LVD counter is filled with 1.5 m^3 organic liquid scintillator (C_nH_{2n} with $\bar{n} = 9.6 + 1 \text{ g/l}$ of scintillation activator PPO + 0.03 g/l of wavelength shifter POPOP, density $\rho = 0.78 \text{ g cm}^{-3}$, attenuation length $\lambda \gtrsim 16 \text{ m}$ [43]). To increase the internal reflectivity, the counters are internally coated by an aluminated mylar film with reflection coefficient ~ 0.92 .

Each counter is monitored by three 15 cm photomultiplier tubes (Feu-49B or Feu-125). In each counter events are defined by the 3-fold coincidence among the three pmts ($\Delta t = 250 \text{ ns}$).

The main reaction inside LVD apparatus in case of a *core collapse SN explosion* is

the Inverse Beta Decay (IBD) on an hydrogen nucleus followed by a neutron capture on a proton which occurs with a mean delay $\tau = 195 \pm 4 \mu s$ after the prompt signal [43]. Since the energy released by neutron captures on free protons is ~ 2.23 MeV, a double threshold system has been developed in order to detect both the positron and neutron capture signal: the detection of this double pulse gives the signature for IBD interactions. The two LVD threshold level are:

- High Threshold (HT) (~ 4 MeV) is the standard threshold of every LVD counter;
- Low Threshold (LT) (~ 1 MeV) is set during a gate $\Delta t = 1$ ms after an HT event in all the counters of a module in which the HT event occurred.

2.2.2 LVD as neutron detector and neutron moderator

LVD is a neutron detector, not only a SN neutrino observatory: the hardware and DAQ setup that makes LVD a neutrino detector makes it also a good neutron detector, especially for muon-induced neutrons. In fact, a neutron incoming on a LVD counter can incur very easily in energy losses by elastic scattering on protons. When the neutron energy is thermal or epithermal the probability of its nuclear capture becomes large enough to make neutron capture happen inside a short time window (as described in the previous paragraph).

$$n + p_1 \Rightarrow n + p_1$$

$$\hookrightarrow n + p_2 \Rightarrow n + p_2$$

$$\hookrightarrow n + p_n \Rightarrow n + p_n$$

$$\hookrightarrow n + p_{last} \Rightarrow D + \gamma \quad (E_\gamma = 2.23 MeV)$$

In this case the energy of prompt signal is given by $\sum^i E(p_i)$ and the detection of the double pulse gives the signature for disentangling neutrons from the other background components. It is possible that one single counter would not be sufficient for thermalizing and stopping a neutron: in this case the neutron energy would be given by the

sum of the energy seen by all the counters crossed by the neutron. The real situation is more complicated and it is necessary to take into account:

1. the energy losses due to neutron inelastic scattering;
2. the uncertainty for locating the neutron production point;
3. the uncertainty for disentangling the energy of neutron from the energy of other component of the muon induced cascade;
4. the quenching effect for non-relativistic particles inside liquid scintillator;
5. the LVD modular geometry that determines energy loss, due to escaping particles and scattering in iron;
6. the energy threshold and resolution for each counter.

LVD was already used for performing a measurement of muon-induced neutrons flux and multiplicity as a function of the distance from the parent muon [44]. Even if the streamer tubes were switched-off in 2001 (that involved a bigger difficulty for locating the muon track and the neutron generation point), a new measurement of muon-induced neutrons is underway [45].

The largest component of underground neutrons is due to neutrons coming from natural radioactivity of the surrounding rock (see chap. 1). Their energy spectrum runs out for $E_{neutron} > 10$ MeV [2]: for a such energy the quenching effect in LVD liquid scintillator is ~ 2 (see chap. 5 tab. 3.4) whereas the LVD HT is 4 MeV. This means that a measurement of radioactivity neutrons is very hardly achievable by LVD. Even if unable to measure their flux, LVD liquid scintillator remains a very powerful neutron moderator: it is extremely interesting to study the attenuation factor for radioactivity neutrons during their propagation inside LVD.

2.3 The LVD Core Facility

The LVD Core Facility project consists on making a cavity inside the inner part of LVD by removing two modules, each of them formed by 8 counters (see fig.2.21): the obtained volume, called LVD Core Facility (LVDCF), is about $6 \times 2.5 \times 2 \text{ m}^3$, enough for housing a 1 Ton WIMP detector [47].

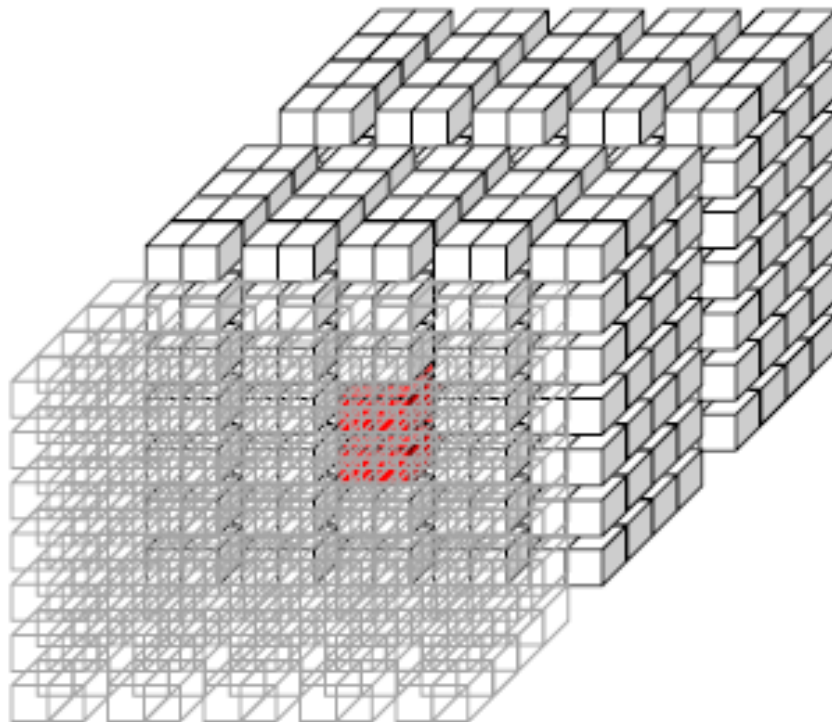


Figure 2.21: A schematic view of LVD detector with LVD Core Facility in red [47]

This solution does not have a heavy impact on the LVD main task (i.e. SN neutrino telescope) and it would offer several advantages about background reduction for WIMP detection:

1. the observed γ flux is ~ 10 times lower than the one observed in Hall A outside LVD, as shown in fig.2.22;
2. Since LVD is considerably bigger than the obtained cavity, it could work like a big veto for muon passing far away from the WIMP detector: this will reduce

largely the muon induced background, particularly neutrons;

3. the low energy neutron flux is expected to be considerably reduced.

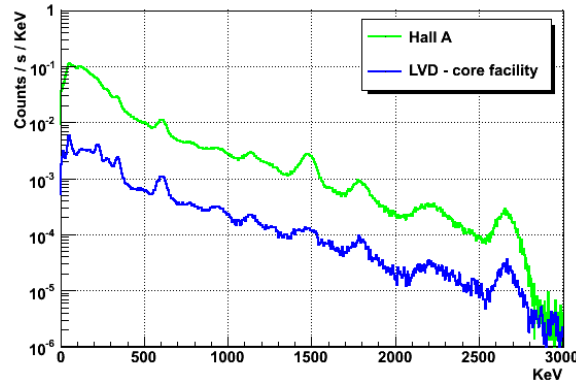


Figure 2.22: Gamma background measurement obtained by a NaI(Tl) detector inside Hall A and inside LVD inner part [48]

2.4 Geant4 simulation of LVD Core Facility

A Geant4 based simulation was made for studying the reduction factor of neutron background flux inside LVDCF by using LVD as an active veto (muon-induced neutrons) and as a passive shielding (muon-induced and radioactivity neutrons).

The simulation geometry is shown in fig.2.24-2.25 and here summarized:

1. The LVD geometry was the real one: so there are 114 modules, each of them made by 8 counters, placed on 3 towers, 5 columns and 7 or 8 modules level;
2. the two modules located in the third and the fourth level of the third column of tower 2 were removed and replaced with a parallelepiped 2 m large, 6 m deep and 2.5 m high made by air: the LVDCF volume;
3. the 1% Borum doped paraffin layer 10 cm thick covering Hall A floor under LVD was considered;
4. all the main iron structures were considered;

5. for the study of muon-induced neutrons the rock surrounding LVD was considered by a layer ~ 6 m thick. This layer was removed for the simulation of radioactivity neutrons because they are isotropic and their possible backscattering on Hall A walls was already computed in their total flux.

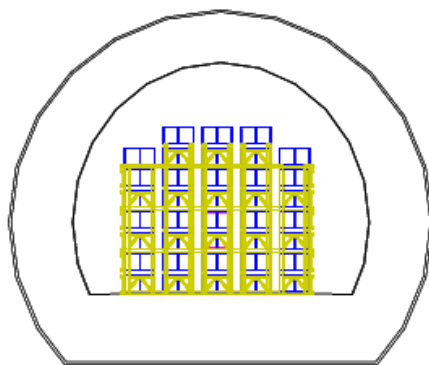


Figure 2.23: Simulation geometry front view

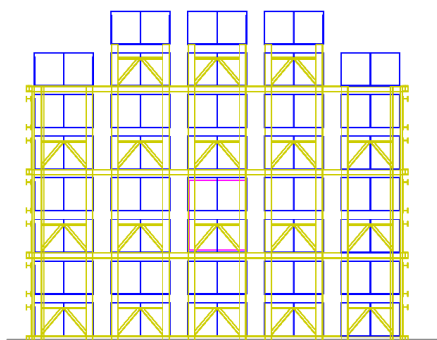


Figure 2.24: Simulation geometry front view (without rock)

In fig. 2.23 the full geometry is shown, while the In fig.2.24-2.25 it is possible to see in more detail the modules (in blue), the paraffin layer (in gray), the iron structures (in yellow) and, less evident, the LVDCF (in purple).

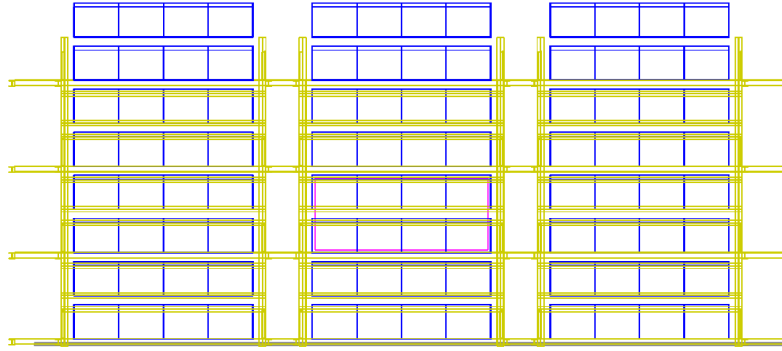


Figure 2.25: Simulation geometry lateral view (without rock)

2.4.1 Muon-Induced Neutrons

For muon-induced neutrons, it has been evaluated both the active vetoing and the shielding power of LVD by Selvi *et al.* [48]. In this simulation the primary particle was a muon with a energy spectrum and angular distribution sampled accordingly to [46],[1]. The aim of this work was to evaluate how many neutrons (and their energy spectrum) produced by those muons would arrive in the LVDCF in four different conditions:

1. inside LNGS Hall A with LVD switched off (only passive shielding);
2. inside LNGS Hall A with LVD switched on;
3. inside LNGS Hall A without LVD;
4. inside a deeper underground site (Sudbury).

For the first and the second case (which have been studied at the same time by asking or not asking the “tagged” condition for the neutrons incoming the LVDCF) it was also stored as output the energy released in each LVD counter for each events: a counter was considered “hit” during an event if there was an energy release above 10 MeV inside its liquid scintillator. An event (and consequently a neutron) was defined “tagged” if there were at least two hit counters.

For the other two cases it has been necessary to make simulation runs again: in the third case the LVD apparatus was completely removed, in the fourth one the the muon

energy spectrum and angular distribution were modified in agreement to what expected in the Sudbury underground site [1].

Muons were generated over the experimental Hall with a trajectory selected in order to hit a circular surface with radius 15 m whose center corresponds to the center of LVD.

$5 \cdot 10^6$ events (corresponding to ~ 8 months real time in LNGS Hall A) have been generated: the results for the four different cases have been collected in Table 2.1.

$\Phi(10^{-9} \text{ n cm}^{-2} \text{ s}^{-1})$	LVD off	LVD on	LNGS Hall A	Sudbury Hall
Φ_{total}	0.60	0.022	1.78	0.0337
$\Phi(E > 1MeV)$	0.30	0.0066	0.30	0.0048
$\Phi(E > 10MeV)$	0.10	0.0023	0.11	0.0015
$\Phi(E > 100MeV)$	0.03	0.0005	0.03	0.0004

Table 2.1: Neutron fluxes inside LVDCF [48]

Table 2.1 shows that it is possible reducing by a factor 50 the muon induced neutron flux by using LVD as muon veto. The same result is not achievable by using LVD just as a passive shielding because neutrons can be easily produced by muons in the LVD iron structures and the total flux would result similar to the one obtained in Hall A without LVD. This can be easily seen in fig.2.26 where it is shown that most of muon induced neutrons reaching LVDCF are generated inside LVD itself (in particular near the LVDCF), whereas most of un-vetoed ones are generated inside the rock surrounding Hall A.

In conclusion, the predicted muon induced neutrons flux inside LVDCF by using LVD as active veto is similar to the one expected inside the Sudbury underground site in Canada[48] which is much deeper (6020 m.w.e *vs.* 3100 m.w.e.).

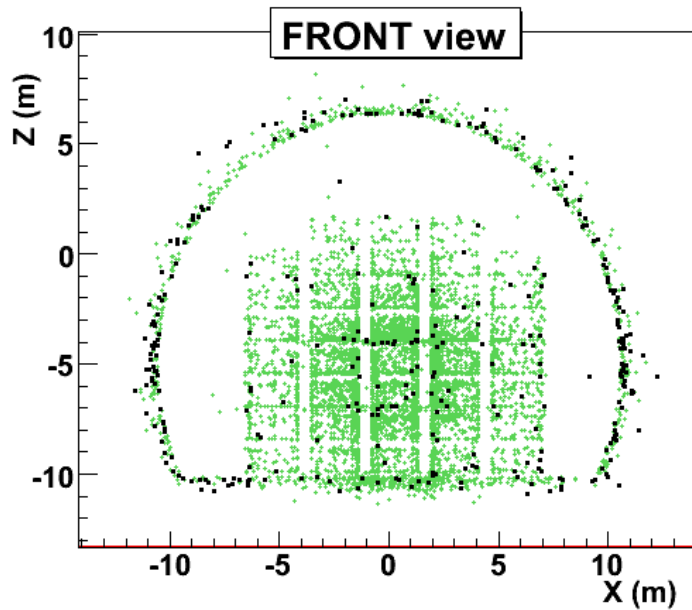


Figure 2.26: Position where muon induced neutrons which reached LVDCF were produced: in green events vetoed by LVD, in black un-vetoed ones [48]

2.4.2 Radioactivity neutrons inside LVD Core Facility

For radioactivity neutrons, only the shielding power of LVD was evaluated because their energy is too low for being detected by LVD (see sec. 2.2.2). In this simulation the primary particle was a neutron sampled with isotropic angular distribution and with an energy spectrum according to [2]. This work was aimed to evaluate the energy spectrum and the attenuation factor for radioactivity neutrons incoming the LVDCF.

Neutrons launching surface Neutrons were produced homogeneously on a closed surface, formed by a hemisphere and a circular plane which was located at Hall A ground level, which was centered in correspondence of the LVD central point. The radius of the hemisphere and of the circular plane was 18 m long: in this way all the LVD detector (iron structures included) and the paraffin layer were fully inscribed inside this surface (see fig.2.27). The total area of neutron launching surface was given by $3 \pi r^2$.

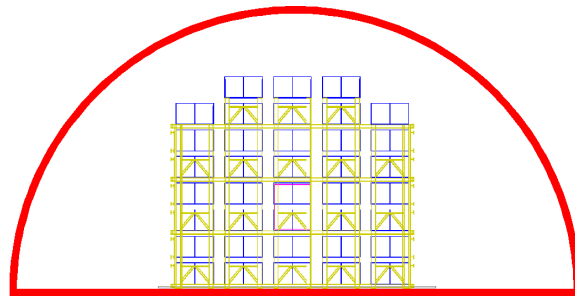


Figure 2.27: Simulation geometry together with neutrons launching surface, front view

Neutrons momentum Neutrons were generated isotropically incoming the plane which is tangent to the launching surface: in this way the solid angle covered was 2π sterad and the needed CPU time was halved. Neutrons kinetic energy was extracted between 0.5 and 8.5 MeV according to the computed radioactivity neutron energy spectrum inside Hall A by [2] and shown in fig.2.28.

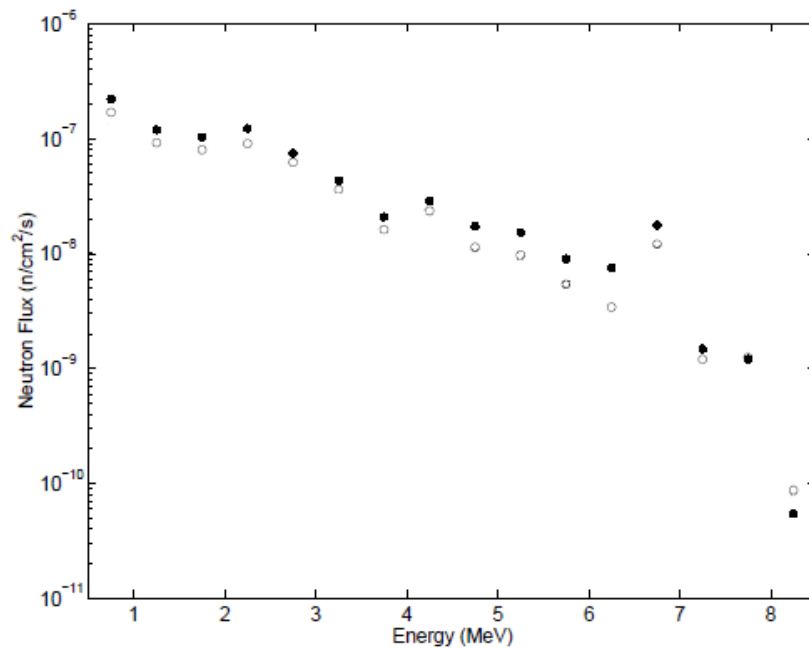


Figure 2.28: Neutron flux at the Gran Sasso laboratory, ●: Hall A ○: Hall C [2]

Neutrons inside LVD Core Facility When a neutron reaches the LVDCF volume, its kinetic energy was stored in an histogram; also the coordinates x, y, z of starting point were stored as output.

Results $1 \cdot 10^7$ neutrons have been generated along the launching surface: among them, 1,508,659 have been captured inside LVD liquid scintillator and 688,091 inside LVD iron structures; only 18,615 neutrons (8,489 with kinetic energy above 1 MeV) reached the LVDCF.

In fig.2.29 the energy spectrum of neutrons incoming LVDCF is shown together with the energy spectrum of generated neutrons (normalized to the same area).

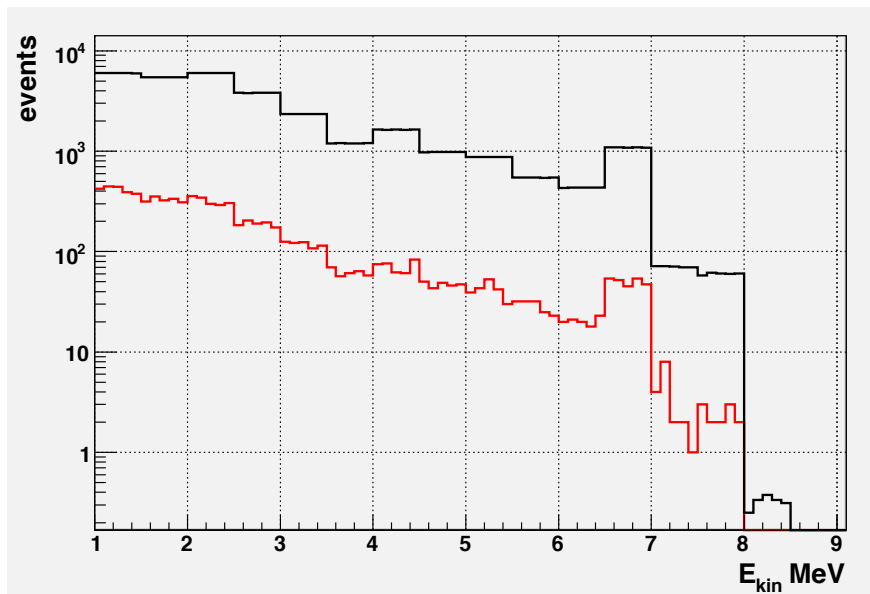


Figure 2.29: Kinetic energy spectrum of generated neutrons (in black) and neutrons reaching LVDCF (in red), the spectra have been normalized to the same area

The ratio between the integral of the two spectra for $E_{kin} > 1$ MeV gave the attenuation factor of LVD to radioactivity neutrons:

$$Q = \int_{E_1=1MeV}^{E_2=8.5MeV} \frac{\Phi(Hall A)}{\Phi(LVD C. F.)} dE = 17.95 \pm 0.19(stat.)$$

Since neutrons were generated only with a direction incoming the launching surface,

the neutron flux inside LVDCF is expected to be $2 \times Q$ times smaller than inside LNGS Hall A, i.e. $Q_{eff} = 35.9 \pm 0.4(\text{stat.})$.

In fig.2.30-2.32-2.31 are drawn the Cartesian projection of the point where neutrons, which reached LVDCF, have been generated (the central point of LVDCF is placed in $X = 11.582 \text{ m}$, $Y = -6.764 \text{ m}$, $Z = 0.27 \text{ m}$).

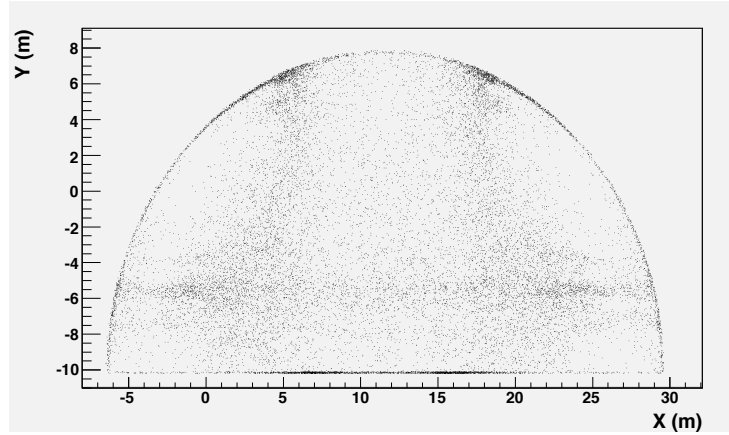


Figure 2.30: Starting point of neutrons reaching LVDCF, xy (lateral) view

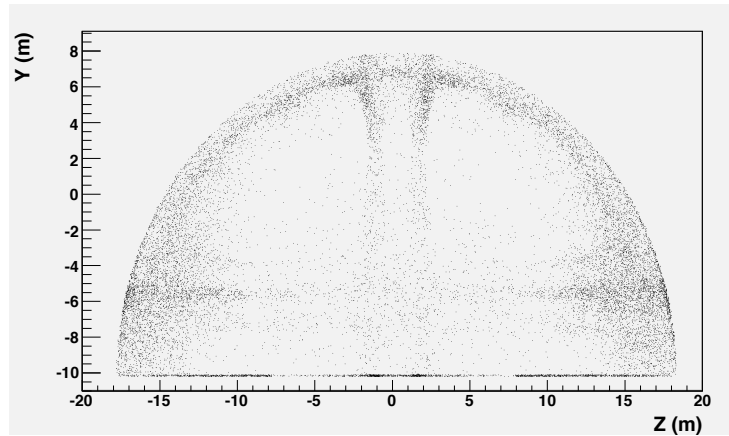


Figure 2.31: Starting point of neutrons reaching LVDCF, zy (front) view

It is evident that most of neutrons which reached LVDCF has been generated near a corridor, especially the corridors between the 3 towers and the ones between column 3 and column 2 and 4. This is in agreement with our expectations and confirms that LVD liquid scintillator is a good neutron moderator.

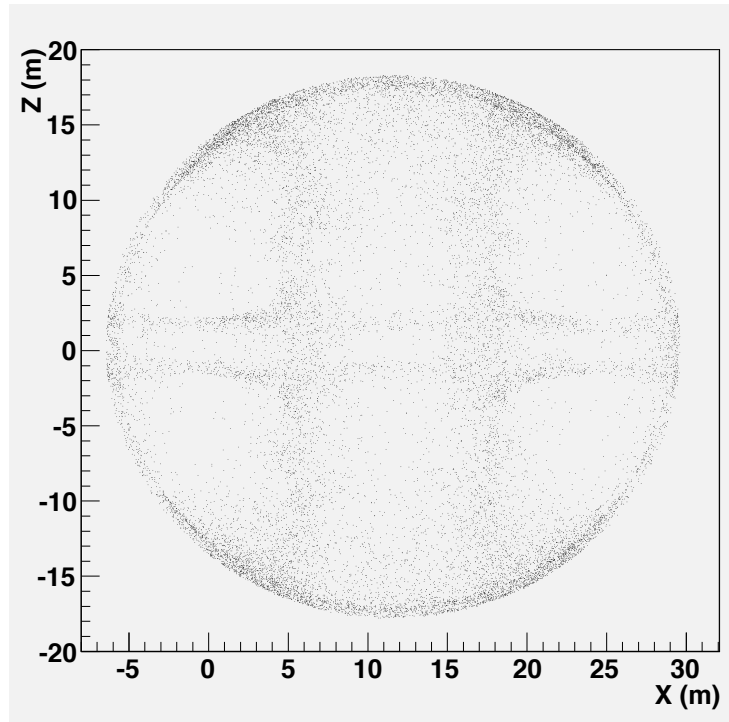


Figure 2.32: Starting point of neutrons reaching LVDCF, xz (top) view

2.5 Conclusion

The ultimate background for underground Dark Matter experiments is formed by neutrons which are produced by muon interaction and natural radioactivity. It is possible to obtain a low background location, called LVD Core Facility, by making a cavity inside LVD apparatus. This location is sized $6 \times 2 \times 2.5 \text{ m}^3$ and it is able to house a 1 Ton new generation WIMP detector. A Geant4 Monte Carlo code was produced with good accuracy in order to simulate the fluxes of muon induced and radioactivity neutrons inside the LVD Core Facility.

Muon induced neutrons The attenuation factor by using LVD as active veto is ~ 50 making the expected muon induced neutron flux similar to the one expected in Sudbury underground site. On the contrary, by using LVD as passive shielding only, the attenuation factor is negligible and the flux results similar to the one present in

Hall A outside LVD: in fact, neutrons can be produced by muons crossing LVD iron structures.

Radioactivity neutrons The attenuation factor for radioactivity neutrons with energy above 1 MeV is equal to $Q_{eff} = 35.9 \pm 0.4(\text{stat.})$. Since the radioactivity neutron flux inside LNGS Hall A was estimated equal to $5.8 \pm 1.3 \cdot 10^{-7}$ neutrons $\text{cm}^{-2} \text{s}^{-1}$ by [2], the radioactivity neutron flux inside LVD Core Facility has been estimated

$$\Phi_n(E_{kin} > 1 \text{ MeV}) = 1.6 \pm 0.4 \cdot 10^{-8} \text{ neutrons cm}^{-2} \text{ s}^{-1}.$$

Chapter 3

The on-the-ground detector

In this chapter I described the detector used for performing the measurements of stopping muons and atmospheric neutrons which are reported in chap. 5. The detector was formed by a Gd-doped LVD counter located in the Laboratori Nazionali del Gran Sasso (LNGS) Assembly Hall equipped with a muon active veto assembled in Turin at the INFN technological laboratory. All the realization stages (design, fulfillment, test) of the veto system are described too.

3.1 The LVD on-the-ground counter

On July 2005, the 1.2 tons *white-spirit* liquid scintillator of one LVD (Large Volume Detector, see chap. 2 sec. 2) counter was doped with Gadolinium (Gd) up to 0.1% fraction mass for studying performance and stability of the Gd doped liquid scintillator [50]. The counter (called T40) was not part of the LVD detector: it was located as spare counter in the LNGS the external site Assembly Hall ($42^{\circ} 25' 11''\text{N}$, $13^{\circ} 31' 2''\text{E}$, altitude 970 m a.s.l.).

In fig.3.1 T40 is shown together with the argon cylinder, which has been used for removing air residual from liquid scintillator. The two wooden boxes contain the modules of the muon telescope, which has been used for energy calibration.

In comparison with a standard LVD counter, the three *15 cm* Feu-49B photomul-

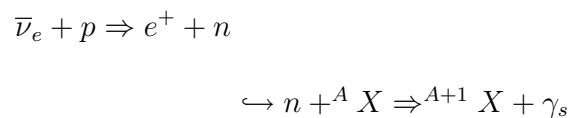


Figure 3.1: T40 test counter

multiplier tubes (pmts) have been substituted by three more efficient *5-inches* Photonis XP3550B pmts in order to increase light collection and energy resolution. XP3550B dividers were modified in order to collect and amplify the last dynode signal: these signals have been used for trigger purposes in the measurements described in chap. 5 sec. 5.4-5.7.

Also the DAQ setup changed: the three pmts signals were sampled by a digital oscilloscope Tektronix TDS5054B (sampling rate 625 MSample/s, 1.6 ns for sampled bin), used as digitizer, and the sampled waveforms were analyzed by off-lines techniques (see chap. 5).

The main reaction inside LVD apparatus in case of a *core collapse SuperNova explosion* is the Inverse Beta Decay (IBD) on an Hydrogen nucleus followed by the neutron capture on a nucleus.



The energy of the prompt signal due to the e^+ is:

$$E_{prompt} \simeq E_{\bar{\nu}_e} - (M_n - M_p - M_{e^+}) c^2 \simeq E_{\bar{\nu}_e} - 0.8 \text{ MeV}.$$

while the energy of delayed signal depends on the nucleus which captured the neutron. The detection of this double pulse gives the signature for IBD interactions.

Usually in LVD standard counters, neutrons are detected through the capture on protons which produces one gamma of energy 2.23 MeV with a mean delay $\tau = 195 \pm 4 \mu s$ after the prompt signal [43]. Since the Gd neutron capture cross section is considerably higher than the Hydrogen one ($\sim 50,000$ barn *vs.* ~ 0.3 barn for thermal neutrons), it is sufficient to dope the LVD liquid scintillator with Gd up to 0.1% fraction mass for reducing the mean neutron capture time to $\tau \simeq 25 \mu s$ [50]-[52]. Furthermore the total energy emission following a (n,Gd) capture is ~ 8 MeV.

It is evident that the LVD efficiency of disentangling neutron captures from chance background would be considerably increased by Gd doping the LVD standard liquid scintillator and, thereby, the efficiency of disentangling IBD events from chance background would be increased too.

In fig. 3.2 it is shown the observed neutron capture energy spectrum (in red), obtained by using a ^{252}Cf source placed in T40 central point, together with the subtracted background (in blue) and the expected spectrum coming from a Geant4 Monte Carlo simulation (in black) [50].

3.2 The active muon veto

An active muon veto system was designed, constructed and tested at the INFN technological laboratory in Turin, then transported to the LNGS and assembled around T40.

3.2.1 Instrumentation recovery

Before starting with veto design, the first very preliminary phase was to get the needed plastic scintillator slabs, light guides and pmts. Since all of these objects are very

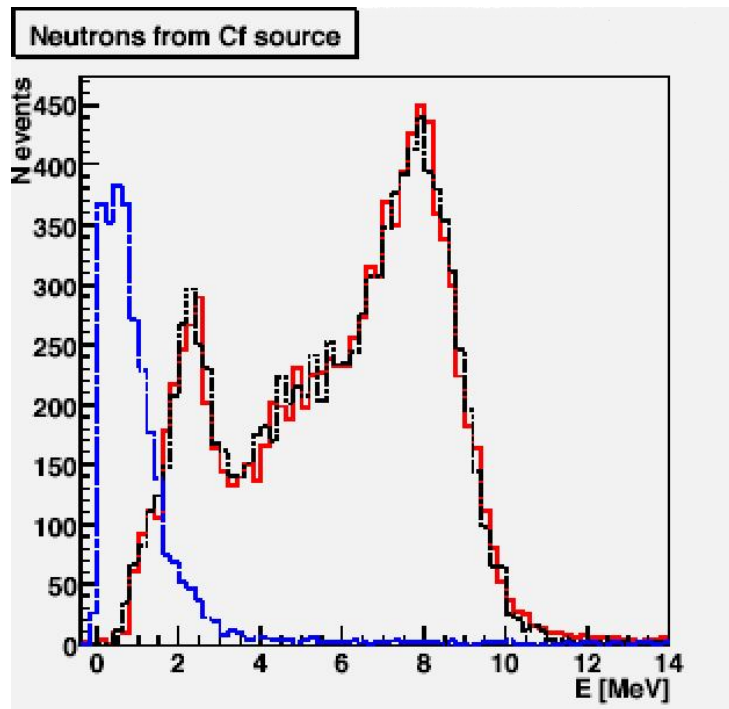


Figure 3.2: Observed neutron capture energy spectrum (in red) after background subtraction (in blue), Monte Carlo simulation spectrum (in black) [50]

expensive, we decided to recover them from old detectors.

The plastic scintillator recovery The plastic scintillator and the light guide were recovered by detectors stored inside “Monte dei Cappuccini” underground laboratory in Turin: even if the detectors were in very poor condition as shown in fig.3.3, the plastic scintillator slabs and the light guides were still good enough to be re-used (after an accurate cleaning up). We globally recovered:

- 10 slabs 3 cm thick, 140 x 70 cm² large, together with respective light guides;
- 2 slabs 2 cm thick, 120 x 120 cm² large, together with respective light guides.

The pmts recovery The photomultiplier tubes (pmts) recovered were *2-inches* XP2020 fast pmts: in the '80s they were used for the Obelix experiment and they were stored in the INFN technological laboratory in Turin. Their weight has been



Figure 3.3: A detector retrieved from Monte dei Cappuccini laboratory

reduced by replacing their iron cylindrical shell with an aluminum one. All of them have been tested to check:

- their sensitivity: by using the light produced by a plastic scintillator 1 mm thick beamed by a ^{252}Am source and fitting the obtained charge spectrum by a Gaussian function (see fig.3.4);
- gain function: by using the light produced by a led and changing the intensity of the high voltage power supply (for two random sampled pmTs the single photo electron spectrum was measured too);
- noise: by measuring the dark counting rate for Gain $G = 10^7$ with threshold level equal to 0.2 photo-electrons.

3.2.2 The design

The veto apparatus design had to take into account:

1. T40 size: the smallest parallelepiped circumscribing T40 is 157 cm long, 130 cm high and 107 cm wide;

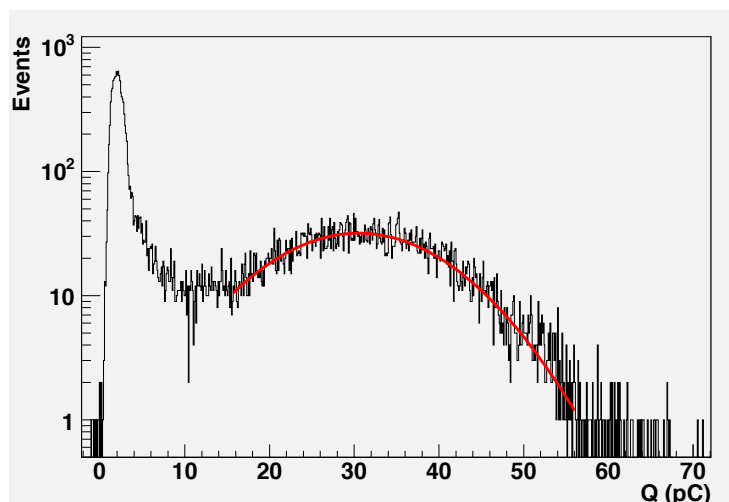


Figure 3.4: Charge spectrum for a XP2020 pmt enlightened by plastic scintillator 1 mm thick beamed by a ^{252}Am source

2. the number of recovered ptms, ~ 40 ;
3. the size of recovered plastic scintillator slabs because it was very difficult to cut and glue them.

The best solution was to make nine independent modules, as shown in fig.3.5-3.6, and here summarized:

- 2 modules $120 \times 120 \text{ cm}^2$, 2 cm thick, called Top1 and Top2: they have been partially superimposed for covering T40 upper surface;
- 2 modules $110 \text{ cm} \times 140 \text{ cm}^2$, 3 cm thick, called S2 and S4: they have been used for covering each T40 short lateral side;
- 1 module $156 \text{ cm} \times 104 \text{ cm}^2$, 3 cm thick, called Bottom for covering T40 lower surface;
- 2 modules $100 \text{ cm} \times 140 \text{ cm}^2$ called S1_a and S3_a plus 2 modules $70 \text{ cm} \times 140 \text{ cm}^2$ called S1_b and S3_b, 3 cm thick, for covering the two T40 long lateral surface.

Each module was equipped by 2, 3 or 4 pmts depending on module size and thickness:

- S1.b and S3.b by 2 pmts;
- S1.a, S2, S3.a, S4 and Bottom by 3 pmts;
- Top1 and Top2 by 4 pmts.

Therefore, the total number of employed pmts was 27.

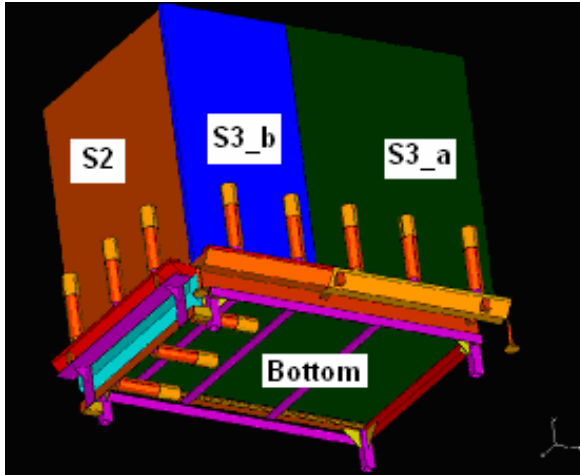


Figure 3.5: T40 veto looked upward

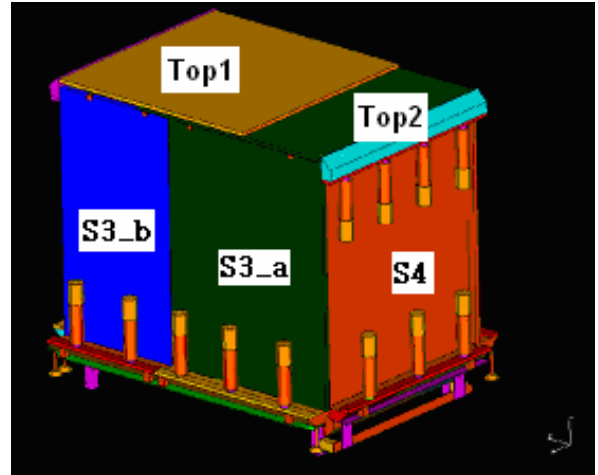


Figure 3.6: T40 veto looked downward

3.2.3 The assembling phase

All the assembling phases were carried out at the INFN-Technological Laboratory in Turin.

For assembling veto modules, it was necessary to wash and dry the plastic scintillator slabs and the light guides. Then, for each module, the light guide has been glued on the scintillator slab (as shown in fig. 3.7): before this, for the most complex modules, two different scintillator slabs and/or two different light guides have been pasted in order to form a unique piece (as shown in fig.3.8-3.9). The used glue was the Bicon BC600.

Then each module was packaged firstly by a *double aluminum-coated* mylar film to increase the light collection and, subsequently, by a polypropylene layer 0.3 mm thick

to shield it from external light and accidental shocks (as shown in fig.3.10-3.11-3.12). Finally pmts have been installed: the optical interface between the photocathode of each pmt and the light guide has been set up by an optical disc ~ 1 mm thick composed by Sylgard 184 elastomer.



Figure 3.7: The gluing phase of a light guide on a scintillator slab

Figure 3.8: The gluing phase of a pair of scintillator slabs

3.2.4 The selection of single module logic of trigger

After the assembling phase, the next step was to set up the logic of trigger of all the modules for enabling them to detect muons. In fact, with the exception of Top1 and Top2 which were in a particular geometrical configuration, all the modules have 2 or 3 pmts and there were two different options for the logic of trigger:

- a) discriminating each pmt and asking for a *n-fold* coincidence;
- b) discriminating the sum/average of all pmts signals.

In order to take a decision, the module S3_b was used for test (the modules setup is described in the next subsection). Muons crossing S3_b in different positions (which



Figure 3.9: The gluing phase of a two pairs of light guides

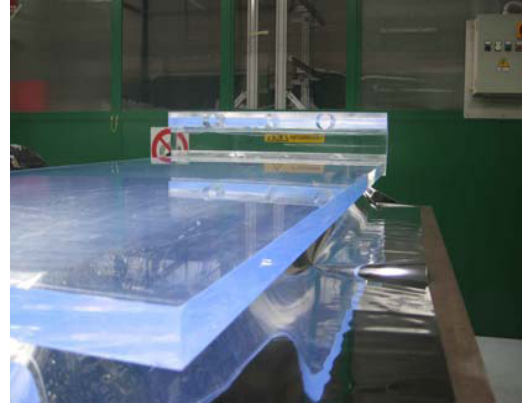


Figure 3.10: A naked module before packaging



Figure 3.11: The same module after mylar packaging



Figure 3.12: The same module at the final state

are shown in fig.3.13) were selected by an hodoscope (formed by a pair of small plastic scintillator $16 \times 22 \text{ cm}^2$) and the signals of the two pmts were sampled by a digital oscilloscope Tektronix TDS3054 in time windows 200 ns long (sampling rate 2.5 GSamples/s). Then the sampled waveforms were analyzed by a ROOT code, here

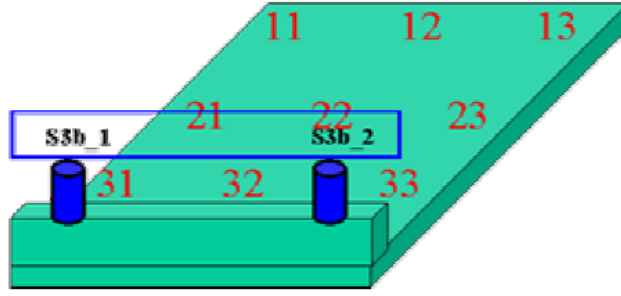


Figure 3.13: Module S3.b with map of observed points

briefly summarized:

1. the first 48 ns of each waveform, where no signal was expected to be, were used to evaluate the baseline and its fluctuation on each channel;
2. the muon signal was searched in the remaining 152 ns and identified by the coincidence among the two pmts (threshold baseline mean value + 3σ baseline fluctuation, coincidence time interval 4 ns);
3. the efficiency for option a) and option b) versus threshold value was computed for each signal.

For all the different collected positions, the normalized sum of the efficiency function versus threshold value is shown in fig. 3.14 (option a)) and fig. 3.15 (option b)).

The last step consisted on measuring the S3.b counting rates in the two different configurations at different threshold values: the results are collected in Table 3.1.

pmt1 AND pmt2		pmt1 + pmt2	
Thr (mV)	Hz	Thr (mV)	Hz
30	690	40	590
40	475	50	440
50	340	60	340
60	270	70	270
70	235	80	230
80	210	90	205

Table 3.1: Observed counting rates in the two configurations as function of threshold

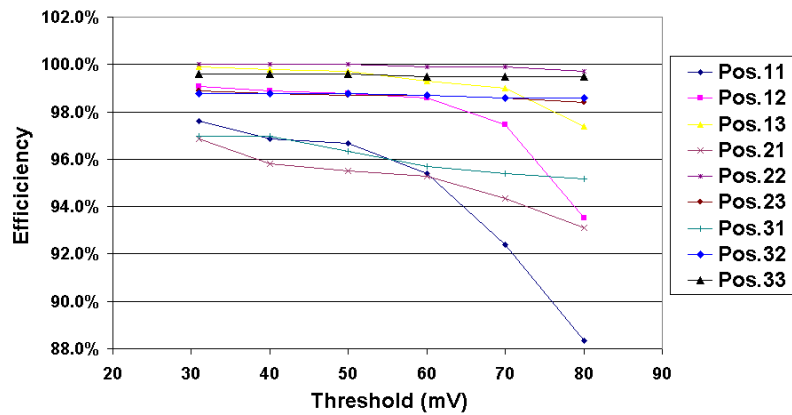


Figure 3.14: Observed detection efficiency obtained by setting “pmt1 AND pmt2”

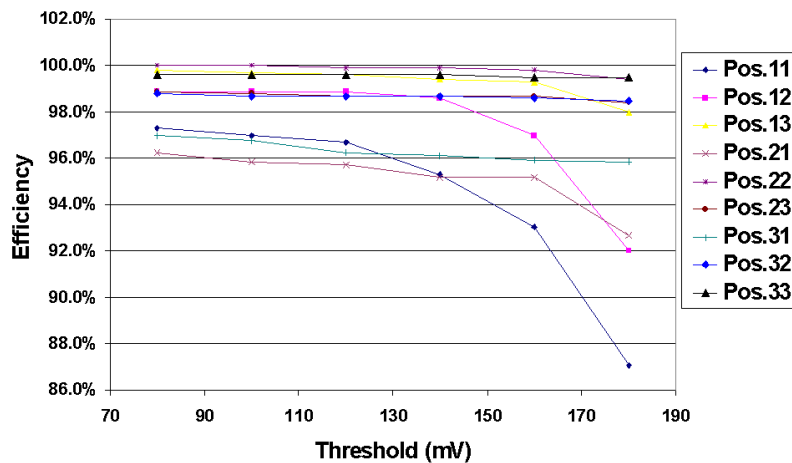


Figure 3.15: Observed detection efficiency obtained by summing pmt1 and pmt2

Table 3.1 and fig.3.14-3.15 show that the two configurations of logic of trigger had similar detection efficiencies for similar counting rates. Since discriminating the signals of all the pmts was largely more expensive than discriminating the sum/average of them, the second option has been preferred.

The last task consisted in determining the trigger configuration for the modules Top1 and Top2, which were only 2 cm thick and partially overlapped. Also in this case we had to decide between two different options:

- a) summing/averaging the signals of Top1 and Top2;
- b) dealing with Top1 and Top2 separately as two independent modules.

In order to take a decision, Top1 and Top2 were placed in their final geometry and, after that, a measurement of detection efficiency was performed in the same way previously described. After the worst point among the measured ones was found for both the considered options, the threshold value was set in order to have the worst point efficiency $\epsilon \geq 98\%$. Finally, the counting rates has been measured for both the possible options.

The obtained results are:

- $\epsilon = 99.8\%$ counting rate = 1500 Hz, for setup a);
- $\epsilon = 99.8\%$ counting rate = 1430 Hz, for setup b).

The performances for both the options were very close and, like in the previous case, the cheaper solution has been preferred again, i.e. summing/averaging the signals of Top1 and Top2.

The final veto trigger configuration is here summarized (see fig.3.16):

- all the pmts signals of each module were collected by a “passive sum” and the output was discriminated (Top1 and Top2 are dealt as a single module);
- the outputs of the eight discriminators were collected by an “OR” logical pattern whose output was a logical signal (100 ns width);
- in real data taking this output was acquired in order to discriminate between vetoed and un-vetoed events (see chap. 5);
- an event was considered “vetoed” if it occurs inside a time window 400 ns wide centered at the time of occurrence of the veto signal, otherwise “un-vetoed”.

3.2.5 The testing phase

After the assembling phase, each module was tested. First of all, the pmts gains were equalized by selecting muons crossing the module central point. In order to take into account the geometric effects due to equalization modality, the peak value was required to be:

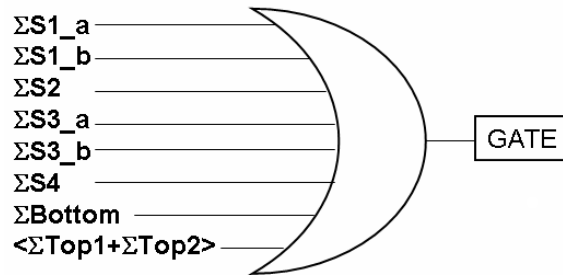


Figure 3.16: Diagram of the veto trigger

- a) in the modules equipped by 3 pmts: ~ 200 mV for central pmt and ~ 150 mV for side ones ;
- b) in the modules equipped by 2 pmts: ~ 170 mV for both the pmts ;
- c) in the modules equipped by 4 pmts: ~ 120 mV for central pmts and ~ 80 mV for side ones (scintillator slabs are 2 cm instead of 3 cm thick).

The detection efficiency was measured for each module. Threshold values have been set in order to obtain a detection efficiency greater than 98% for all the measured positions.

An exception was made for the Bottom module whose scintillator surface was assembled by three scintillator slabs glued in two different phases: its observed worst point (w.p.) was $\epsilon = 97.4\%$. This value has been considered sufficient because the efficiency observed in all the remainder positions was largely above 99%;

The modules features and performance are summarized in Table 3.2

Module	Surface (m ²)	THR (mV)	w. p. efficiency	Rate (Hz)
S1_a	1.4	40	99.3%	540
S1_b	0.98	40	99.8%	440
S2	1.54	40	99.7%	650
S3_a	1.4	40	99.1%	540
S3_b	0.98	40	99.8%	590
S4	1.54	40	99.5%	510
Bottom	1.62	30	97.4%	1200
<Top1+Top2>	2.04	10	99.5%	1500

Table 3.2: Veto modules features and performance

3.3 Conclusion

In November 2007 all the veto modules were transported to the LNGS and assembled around T40, see fig.3.17.



Figure 3.17: T40 during veto assembling phase

In the final geometry the total muon veto counting rate was equal to ~ 2500 counts s^{-1} .

Chapter 4

Geant4 simulation of the on-the-ground detector

In this chapter I describe the Geant4 code which was used for simulating the above ground detector (see chap. 3). In section 4.1 the simulation geometry is reported, while in section 4.2-4.3 are reported the simulations of vertical muons used for calibration purpose. The aim of this work was to give a tool for interpreting the experimental data about stopping muons and atmospheric neutrons as described in chap. 5.

4.1 The apparatus geometry

In the Monte Carlo simulation the apparatus geometry was quite simple and it remained unchanged for all the studied topics. It included just the T40 detector, the active muon veto and the muon telescope which was used for calibration purpose (see chap. 5 sec. 5.2): they were placed inside a cubic experimental hall ($10 \times 10 \times 10 \text{ m}^3$) filled with air.

The active muon veto In the simulation the active muon veto did not play any role in particle discrimination and its role was neglected. It was included in the geometry only to take into account its passive shielding power for atmospheric neutrons. It was simulated as composed by the 8 scintillator slabs which form all its modules (the

bottom module was neglected because useless).

The muon telescope In the real case the muon telescope was formed by two small plastic scintillator slabs contained in two small wooden boxes. Each of them was monitored by one Photonis XP3462 pmt. In order to simplify the simulation and remove useless complications, they were simulated as two volumes filled with air: their dimensions and position were equal to the real ones. No simulation about their working way was done: if a muon went through one of them it was detected with efficiency equal to 1. A muon was “selected” if it went through both the volumes of the muon telescope.

The detector It was formed by a stainless steel box filled with a 0.1% Gd-doped liquid scintillator plus an argon gas layer 4 cm thick, exactly as in the real case. Also the plexiglas optical windows used as optical interface of the pmts were considered. Optical properties of the liquid scintillator (attenuation length and light yield) were extrapolated from LVD standard liquid scintillator (not doped) and from chemical measurements [50],[43]: the attenuation length was fixed at $\lambda = 9$ m and the light yield equal to 7100 photons MeV^{-1} .

For simplifying the simulation geometry, the mylar layer coating the inner surfaces of the stainless steel box was neglected and its optical properties were assigned directly to the stainless steel box. Also the pmts were not included in the simulation and optical photons were removed for saving CPU time for all the topics not needing them. For all the cases optical photons were unavoidable, an output file was created and all the informations about optical photons escaping from T40 through the optical windows were stored inside it. Thus the simulation of pmts light collection and amplification was not done during the Geant4 simulation, but during the analysis of the output file.

The simulated geometry of the full apparatus is shown in fig.4.1: in green the Gd doped liquid scintillator, in blue the argon gas layer, in violet the plexiglas windows, in red the 2 elements of muon telescope and in black the muon veto modules.

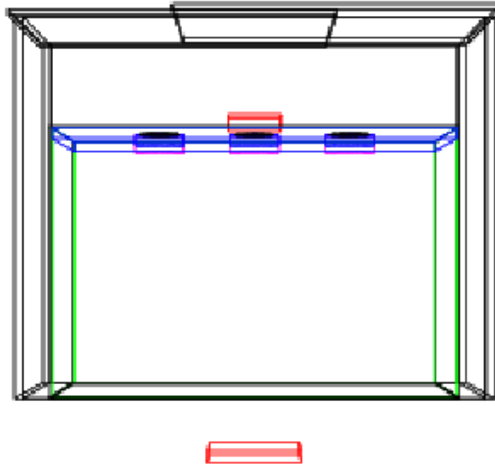


Figure 4.1: Simulated detector geometry, pictorial front view

4.2 Vertical Muons: the released energy

Every time a measurement on T40 was done, the energy calibration of the detector was needed. This was obtained by collecting signals due to muons selected by the muon telescope (as described in chap. 5):

1. the signals were collected and integrated in time;
2. the charge distribution was fitted by the convolution between a Gaussian and a Landau function;
3. the calibration factor was given by the ratio of the fitted function and $Edep_{sim}$ which is the energy released by muons.

It is evident that for doing that, it was necessary to know the energy released by muons selected by the hodoscope.

This simulation is briefly described:

1. 1,000,000 muons equally divided between μ^+ and μ^- of energy $E_{kin} = 1$ GeV have been generated 10 cm above the detector on a surface 1.5×1 m² large;
2. their zenithal distribution was proportional to $\cos^2 \theta$ and the azimuthal distribution was isotropic;

3. $\sim 7,000$ of them passed the muon telescope selection;
4. the energy lost inside the liquid scintillator by selected muons was put in an histogram which has been fitted by the convolution between a Gaussian and a Landau function: the peak of this function gave the energy calibration parameter $Edep_{sim} = 160$ MeV with a relative uncertainty equal to $\frac{\sigma_{Edep_{sim}}}{Edep_{sim}} \sim 2\%$.

For this simulation optical photons were useless and so they have not been used.

4.3 Vertical Muons: the outcoming signal

The simulation of the outcoming charge signal due to muons selected by the hodoscope was useful for two different reason:

1. to fix Q_{sim} , the charge-energy calibration parameter, and $\overline{Nphe_{sim}}$, the photoelectrons-energy calibration parameter;
2. to check the agreement between acquired data and simulated one and fix the correction parameter K. The parameter K was needed for compensating all the approximations made about detector optical properties.

The code used to study the vertical muons spectrum was divided in 2 levels and it is briefly summarized here:

1) Geant4 MC simulation:

1. $\sim 2,000$ muons equally divided between μ^+ and μ^- of energy $E_{kin} = 1$ GeV passing through the muon telescope have been generated;
2. they were generated just above the muon telescope upper detector on a surface 22×22 cm^2 (i.e. a surface slightly bigger than the hodoscope upper module);
3. their zenithal distribution went like $\cos^2 \theta$ and the azimuthal distribution was isotropic;

4. for each event the number of optical photons arriving to the 3 photocathodes was stored in an output file;
- 2) The analysis:
1. for each photon arrived on each pmt a random extraction was made to simulate the light collection efficiency (set equal to 0.15 for all the optical photons, i.e. flat light collection efficiency function);
 2. the total number of photo-electron for each event was collected in an histogram fitted by the convolution of a Gaussian and a Landau function: the peak of that function divided for $Edep_{sim}$ is the photoelectrons-energy calibration parameter $\overline{Nphe_{sim}}$ (found equal to $\frac{5092 \text{ phe}}{160 \text{ MeV}}$);
 3. for each j -th pmt and for each i -th photo-electron produced, a Gaussian random extraction was made to simulate the pmt gain factor G in order to obtain $Q^{i,j} = G \cdot Q_e$ (Q_e is the electron charge);
 4. for each j -th pmt the total charge was given by $Q_{tot}^j = \sum^i Q^{i,j}$;
 5. the total charge value was given by $Q_{tot} = \sum^j Q_{tot}^j$
 6. Q_{tot} was multiplied by a parameter K (K ranging $0.8 \leq K < 1$, $\Delta K = 0.002$) and put in an histogram: by minimizing the χ^2 value between simulation and real data (region of interest encompassed between 330 pC and 480 pC), K was fixed equal to 0.932 (see fig. 4.2) with $\widetilde{\chi^2} \sim 1$;
 7. the corrected Q_{tot} distribution (see fig. 4.3) was fitted by the convolution of a Gaussian and a Landau function: the peak of that function was the simulation energy calibration parameter $Q_{sim} = 381.9$ pC.

It is very important that K was found very close to 1 because this means that all the assumptions previously made (light yield, pmts light collection, surface reflectivity, etc. . .) were quite good. The obtained values of K and of energy calibration have been used for all the simulations described in chap. 2.

In figure (fig.4.3) the vertical muons charge spectrum coming from simulation (in black)

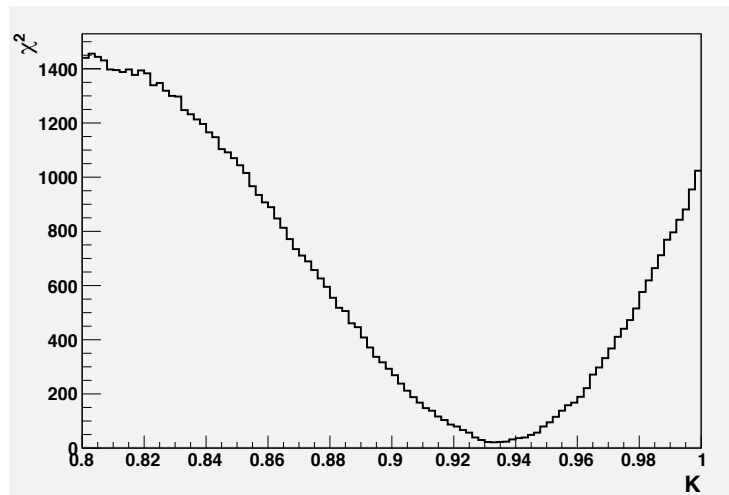


Figure 4.2: Distribution of χ^2 vs. K value

is shown together with the one (re-normalized) coming from real acquired data: the large number of high charge events present in acquired data and not present in simulated data is supposed to be due to vertical muons belonging to EAS.

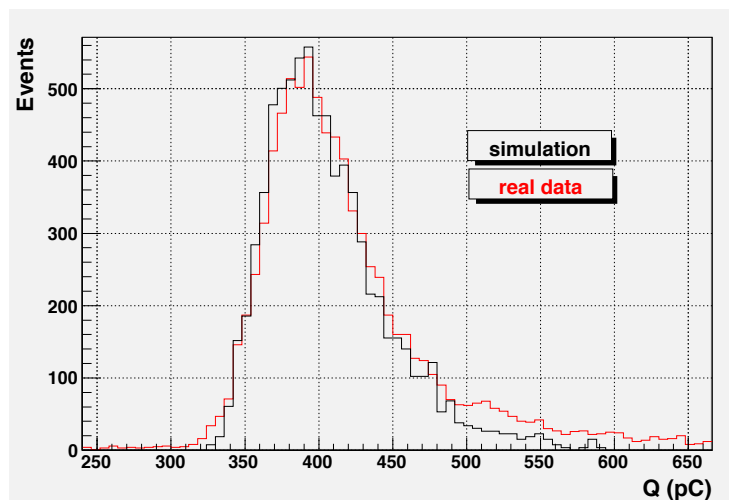


Figure 4.3: Vertical muons charge spectrum, simulation in black, real data in red

4.4 The Michel Spectrum

In chap. 5 sec. 5.6 the measurement of stopping muons rate for $E_\mu > 10\text{MeV}$ is described. In order to estimate the stopping muon rate, a Monte Carlo simulation of Michel spectrum was necessary for evaluating the μ -decay detection efficiency due to the applied energy cuts on delayed signal ($10\text{ MeV} < E_{\text{delayed}} < 60\text{ MeV}$).

The code was divided in 2 levels and it is briefly summarized here:

- 1) Geant4 MC simulation:
 1. muons equally divided between μ^+ and μ^- were generated at rest uniformly distributed inside the T40 liquid scintillator;
 2. for each event the arrival time of all the photons to each pmt were stored in an output file;
- 2) The analysis:
 1. for each photon arrived on each pmt a random extraction were made to simulate the light collection efficiency (set equal to 0.15 for all the optical photons, i.e. flat light collection efficiency function);
 2. for each i -th photo-electron produced, a Gaussian random extraction was made to simulate the pmt gain factor G (pmts gain mean value $\mu=5 \cdot 10^5$, pmts resolution for a single photo-electron $\sigma=50.2\%$) in order to obtain $Q_{phe}^{i,j} = K \cdot G \cdot Q_e$ (Q_e is the electron charge, K the correction parameter computed in sec. 4.3);
 3. for each j -th pmt the charge value Q_{tot}^j was given by $\sum^i Q_{phe}^{i,j}$ inside the integration time gate which, according to the real value, was set to 450 ns (starting from the arrival time of the first generated photo-electron). The arrival time acceptance of the first photo-electron was set $480\text{ ns} \leq t_0 < 10\mu\text{s}$;
 4. in case of photo-electrons generated after the integration time gate, they were considered part of a second signal: all the signals after the first one were discarded;

5. the total charge Q_{tot} was given by $\sum^j Q_{tot}^j$ corrected by the “single pmt” correction [43];
6. the energy of each event was finally given by $E = Q_{tot} \cdot \frac{Edep_{sim}}{Q_{sim}}$ ($Edep_{sim}$ and Q_{sim} are the calibration factors computed in sec. 4.2-4.3).

About 12,000 muons have been generated: 9,544 of them passed the time selection and 8,170 the energy cuts. Consequently, the μ -stop detection efficiency due to energy cuts of delayed signal ($10 \text{ MeV} < E_{delayed} < 60 \text{ MeV}$) has been evaluated equal to $85.5 \pm 1.0(\text{stat.}) \pm 0.5(\text{syst.})\%$. The uncertainties have been computed in the same way used for the real data: the statistical error according to Poissonian fluctuations, the systematic one according to the calibration uncertainty.

The simulated energy spectrum is reported in fig.4.4 together with the measured one (after background subtraction and re-normalization to the same number of events) which is described in chap. 5 sec. 5.7.

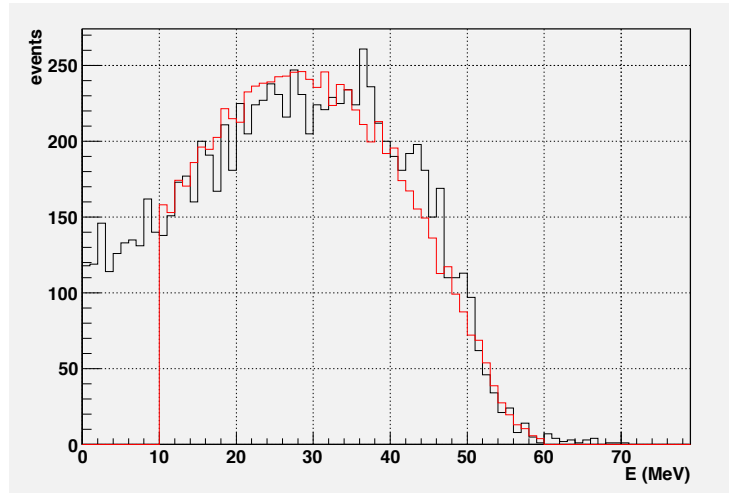


Figure 4.4: Muon decay energy spectrum inside T40, simulation in black and real data in red

The $\widetilde{\chi^2}$ computed on the difference of the 2 histograms is equal to 1.3. That means simulated and real data are in good agreement.

Simulated data are considerably less than real one ($\sim 12,000$ events *vs* $\sim 76,000$ events) because simulation of μ -stop events is noticeably slower than real data acquisition.

That is due to the presence of optical photons inside the MC code: in fact, Geant4 is very CPU time expensive in dealing with optical photons.

4.5 Neutron Capture Detection Efficiency

In chap. 5 sec. 5.5 the measurement of atmospheric neutrons flux for $E_{neutron} > 10MeV$ is described. In order to obtain the atmospheric neutron absolute flux, it was necessary to compare real data with simulated ones. The simulation of atmospheric neutron flux observed in T40 is described in sec. 4.6 but, before simulating that, it was necessary to evaluate the neutron capture detection efficiency due to the applied energy cuts on delayed signals ($3 MeV < E_{delayed} < 10 MeV$).

The simulation was divided in two levels and it is here summarized:

1) Geant4 MC simulation:

1. neutrons with kinetic energy $E_{kin} = 26 meV$ were generated homogeneously inside the liquid scintillator of the detector;
2. their direction distribution was isotropic on 4π sterad;
3. for each event the number of photons collected by each pmt and the time delay of neutron capture were stored in an output file. If the neutron was not captured or it was outside the liquid scintillator of the detector, a negative value was assigned;

2) The analysis:

1. for each photon arrived on each pmt a random extraction was made to simulate the light collection efficiency (set equal to 0.15 for all the optical photons, i.e. flat light collection efficiency function);
2. for each j -th pmt and for each i -th photo-electron produced, a Gaussian random extraction was made to simulate the pmt gain factor G in order to

obtain $Q^{i,j}=K \cdot G \cdot Q_e$ (Q_e is the electron charge, K the correction parameter computed in sec. 4.3);

3. for each pmt the total charge was given by $Q_{tot}^j = \sum^i Q^{i,j}$;
4. the total charge value was given by $Q_{tot} = \sum^j Q_{tot}^j$ (no “single pmt” correction [43] and no “single pmt” threshold were applied);
5. the observed energy was given by $E= Q_{tot} \cdot \frac{Edep_{sim}}{Q_{sim}}$ ($Edep_{sim}$ and Q_{sim} are the calibration factors computed in sec. 4.2-4.3).

$1 \cdot 10^5$ neutrons have been generated and, among them, 96,570 have been captured inside liquid scintillator. The simulated neutron captures energy spectrum is shown in fig. 4.5 together with the experimental one (after re-normalization and background subtraction) which is described in chap. 5 sec. 5.5.

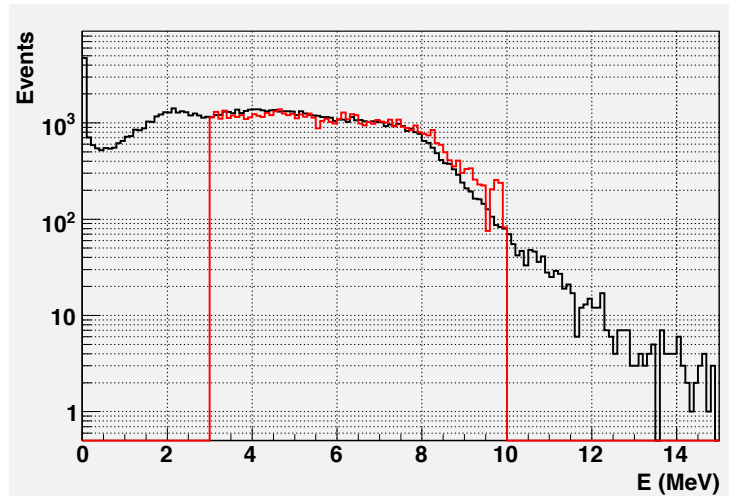


Figure 4.5: Energy spectrum of simulated neutronic capture differential for homogeneously distributed thermal neutrons in black, neutron capture candidates after background subtraction in red

The two histograms shown in fig. 4.5 are in good agreement, even if their agreement gets worse for $E > 8$ MeV. Probably this is due to the starting position of simulated events which have been generated homogeneously inside T40 liquid scintillator whereas this is not necessarily true for real data. In fact, atmospheric neutrons are essentially downward moving, therefore it is easy to guess that in the real case the neutron capture

probability in the T40 upper part is smaller than in the lower one where, for simple geometrical reasons, light collection efficiency is lower. The peak for $E_{vis} < 0.2$ MeV was due to detector border effect.

The total number of events with energy encompassed between 3 and 10 MeV is 63,440. Therefore the neutron capture detection efficiency is equal to $65.7 \pm 0.3(stat.)\%$, as shown in fig.4.6.

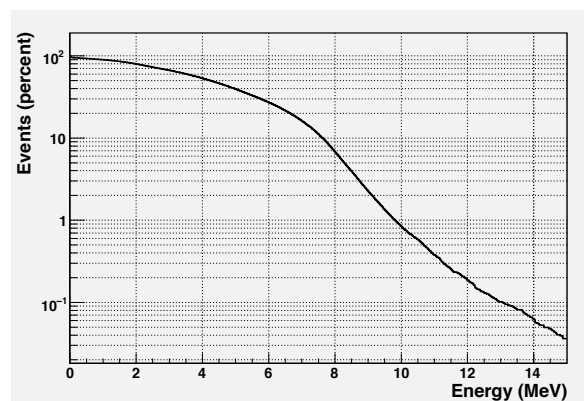


Figure 4.6: Simulated neutronic capture energy spectrum for homogeneously distributed thermal neutrons, normalized integral spectrum

The obtained value of neutron capture detection efficiency ($\epsilon = 65.7 \pm 0.3(stat.)\%$) has been used in the simulation of atmospheric neutrons which is described in the following section.

4.6 Atmospheric Neutrons Observed Spectrum

Since the neutron capture detection efficiency was evaluated in the previous section, the atmospheric neutrons observed spectrum has been simulated. It was necessary to correct the experimental rate:

1. by taking into account the quenching effect of *white-spirit* liquid scintillator for

recoiling protons;

2. by taking into account the trigger efficiency (i.e. the efficiency of neutron capture detection and the probability for an impinging neutron to be captured within $\Delta t < 95 \mu\text{s}$);
3. by scaling the neutron rate to the detector acceptance.

In this case optical photons was not included in the simulation because they would be useless. In fact Geant4 is not able to take into account the liquid scintillator quenching effect. As in the previous case, the simulation was divided in two levels and it is here summarized:

1) Geant4 MC simulation:

1. neutrons were generated homogeneously on a surface $9 \times 6 \text{ m}^2$ large placed 10 cm above the detector with a kinetic energy sampled in agreement with the experimental spectrum obtained by Kowatari *et al.* [54]. (An experimental energy spectrum was used instead of a theoretical one because a theoretical spectrum was never calculated for detectors placed on the ground and, as shown by Goldhagen *et al.* [7] and described in chap.1 sec.2, the neutron energy spectra measured by an on the ground detector and by a flying one are different because soil effects. The spectrum given by Kowatari *et al.* was preferred to the one given by Goldhagen *et al.* because the first one was obtained at 1,020 m a.s.l. whereas the latter one at sea level.). The energy spectrum of simulated neutrons is shown in fig. 4.7;
2. neutrons azimuthal distribution was isotropic while their zenithal distribution was $\propto \cos^3 \theta$ in agreement with Moser *et al.* [55];
3. for each event, the visible released energy E_{vis} inside the liquid scintillator was stored in an output file, whereas the released energy due to neutron capture was discarded. E_{vis} was given by the sum of the energy released by each particle multiplied for its quenching factor which was given by Table 5.2

(quenching factor of particles heavier than alphas was considered equal to 0). The time delay of all the neutron captures occurring inside the detector was stored too (a single primary neutron can produce many secondary neutrons after an inelastic scattering on an nucleus according to its kinetic energy).

2) The analysis:

1. for each neutron capture following a primary neutron within a time delay $\Delta t < 95 \mu s$, a random extraction was done for simulating the neutron capture detection efficiency due to energy cuts (the neutron capture detection efficiency was estimated equal to 65.7% in the previous section). Events not followed by any detected neutron capture were discarded;
2. for the remainder events the global light collection was given by the global number of produced photo-electrons among the three pmts of the detector: this was given by a Poissonian draw whose mean value was equal to the product of E_{vis} and $\overline{Nphe_{sim}}$ ($\overline{Nphe_{sim}} = \frac{5092 \text{ phe}}{160 \text{ MeV}}$ is the the photoelectrons-energy calibration parameter computed in sec. 4.3);
3. for each i -th photo-electron produced, a Gaussian random extraction was made to simulate the pmt gain factor G (pmts gain mean value $\mu=5 \cdot 10^5$, pmts resolution for a single photo-electron $\sigma=50.2\%$) in order to obtain $Q^{i,j} = K \cdot G \cdot Q_e$ (Q_e is the electron charge, K the correction parameter computed in sec. 4.3);
4. for each event the final energy value was given by $E = Q_{tot} \cdot \frac{E_{dep_{sim}}}{Q_{sim}}$.

Among $1 \cdot 10^7$ neutrons which have been generated 17,870 produced a signal of visible energy above 5 MeV and were followed by at least one detected neutron capture and they are called “selected neutrons”.

In Fig. 4.8 the simulated time delay distribution of neutron captures together with an exponential fit whose slope has been found $\tau = 23.2 \pm 0.1 \mu s$, in agreement with real data one reported in chap. 5 sec. 5.5 and equal to $\tau = 24.6 \pm 1.5 \mu s$.

The visible energy spectrum of “selected neutrons” (normalized to the impinging at-

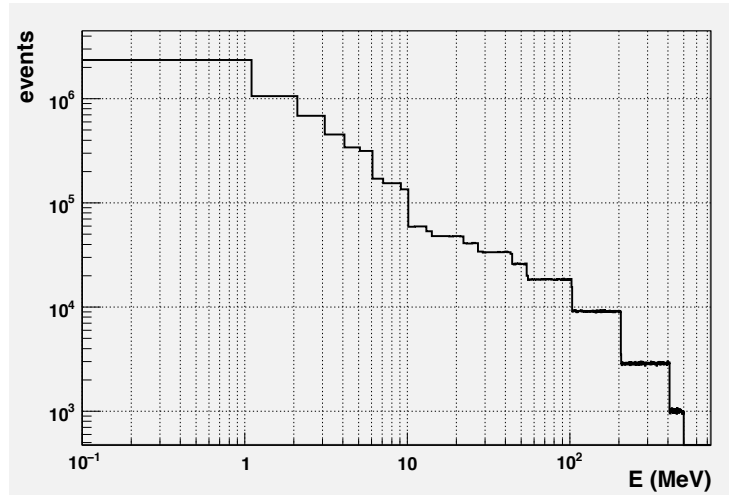


Figure 4.7: Initial kinetic energy of simulated neutrons, sampled according to [54]

atmospheric neutrons flux $\Phi_{neutron}(E>20 \text{ MeV}) = 33 \text{ neutron s}^{-1} \text{ m}^{-2}$ as reported by Kowatari *et al.* [54] and Nakamura *et al.* [53]) is shown in fig. 4.9.

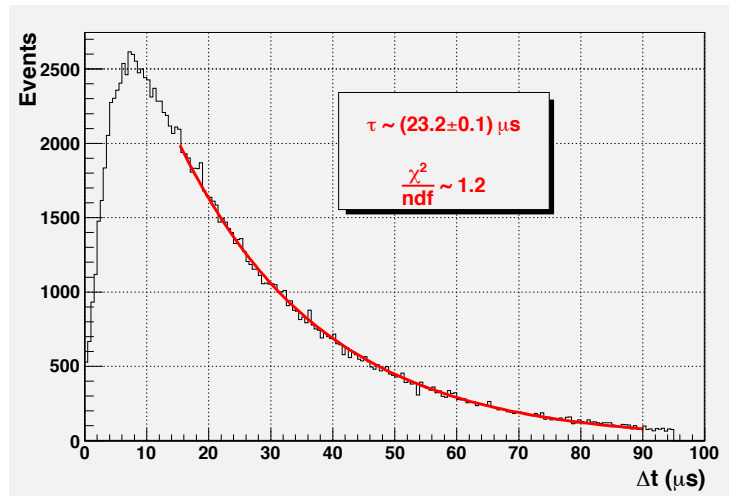


Figure 4.8: Simulated neutron captures time distribution

The T40 acceptance for $E_{neutron} > 10 \text{ MeV}$ was given by the ratio of the number of generated neutrons of energy above 10 MeV and the number of them which reached the liquid scintillator multiplied for the area of the launching surface:

$$Acceptance = \frac{4.163 \cdot 10^6}{1.196 \cdot 10^6} \cdot 54 \text{ m}^2 = 1.55 \text{ m}^2$$

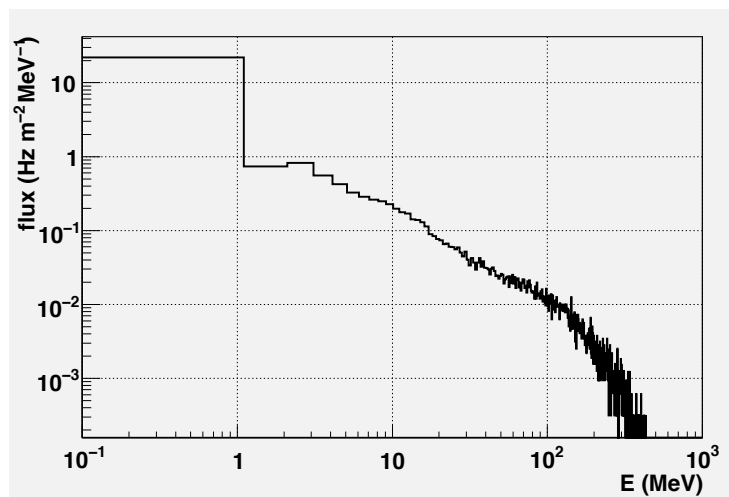


Figure 4.9: Visible energy spectrum of simulated "selected neutrons"

Chapter 5

Above the ground measurements

In this chapter I report the results of the measurements performed with a Gd-doped LVD counter located in the Laboratori Nazionali del Gran Sasso (LNGS) Assembly Hall equipped with a muon veto (see chap. 3).

Since the famous Reines and Cowes experiment [49], Gadolinium (Gd) or Cadmium (Cd) doped detectors have been placed in close proximity to nuclear power plants to study $\bar{\nu}_e$ emitted by the nuclear reactions which take place inside the reactor core. The main problem of these kind of detectors, which cannot be placed deeply underground, is the cosmic rays background which is huge compared to the number of expected $\bar{\nu}_e$ interactions. The number of interaction expected inside a 1 ton water detector placed 50 m away from the reactor core whose thermal power is 1 GW is ~ 340 interactions day⁻¹ (see fig.5.1).

For this reason it is important to know flux and energy spectrum of any background component. In particular the work was aimed to study the fluxes of stopping muons and atmospheric neutrons, which are the main background components for a $\bar{\nu}_e$ surface detector: these measurements are discussed in section 5.5-5.6.

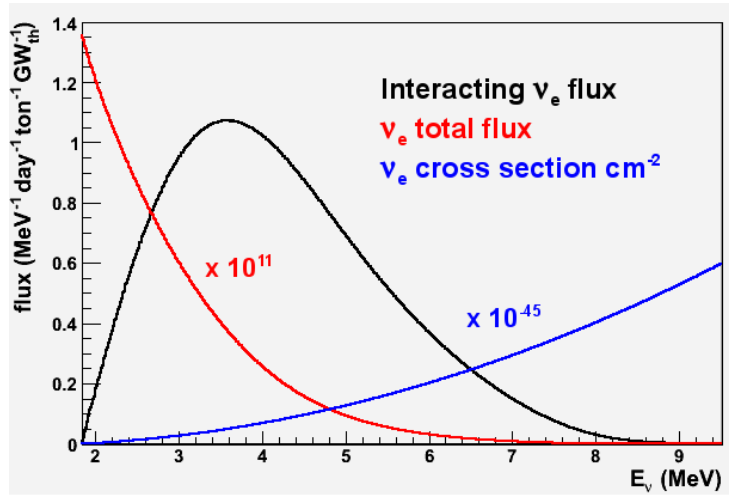


Figure 5.1: Interacting $\bar{\nu}_e$ flux (in black) and $\bar{\nu}_e$ total flux (in red) for a detector located at 50 m from reactor core; IBD cross section (in blue)[51]

5.1 Measurement setup

A Tektronix TDS5054B digital oscilloscope was used as digitizer for collecting the signals coming from the detector and from the veto (8 bits, sampling rate 625 MSample/s, 1.6 ns for sampled bin). For each sampled waveform the pre-trigger region was used for evaluating the baseline and its fluctuations: baseline + its fluctuations were used to set threshold value. The DAQ setup slightly changed according to the measurement:

- setup a) the waveforms coming out from the three *5-inches* XP3550B pmts of the detector and from the veto were sampled by the digital oscilloscope and analyzed by off-line techniques (oscilloscope scale changed according to the measurement from 2 to 50 mV/division). Events were found by the 3-fold coincidence (threshold equal to baseline + 3σ , $\Delta t = 16$ ns) among the detector pmts. The resulting energy was obtained by summing the signals of the three pmts (integration gate 450 ns, total death time 480 ns) and by applying the “single pmt” algorithm [43];
- setup b) the signals of the three pmts of the detector were summed, and this sum was sent to a linear fan out whose outputs were collected by three oscilloscope channels set at different vertical scales (from 5 to 80 mV/division). The signal from the veto was collected by the fourth oscilloscope channel. The sampled waveforms

were analyzed by off-line techniques. Events were found by the most precise oscilloscope scale whose threshold was fixed equal to baseline + 4σ , $\Delta t = 16$ ns (the threshold exceeding was evaluated by integrating the charge every 10 acquired bins: since the time interval between two bins is 1.6 ns, $\Delta t = 16$ ns). The energy was evaluated by exploiting the not-saturated oscilloscope channel with larger sensitivity (integration gate 450 ns, total death time 480 ns).

The DAQ setup a), by allowing to apply the “single pmt” correction of energy over-estimation occurring when the scintillation light is produced close to one detector pmt [43], involved a better energy resolution. DAQ setup a) was used for stopping muons measurement.

The DAQ setup b) involved a broader dynamic energy range but, on the other hand, a reduced energy resolution. DAQ setup b) was used for veto efficiency check and atmospheric neutrons flux measurement.

Also the acquisition windows changed according to the measurement performed:

- energy calibration: acquisition windows 800 ns long;
- background spectrum: acquisition windows 100 μs long;
- veto efficiency test: acquisition windows 100 μs long;
- atmospheric neutrons: acquisition windows 100 μs long;
- stopping muons: acquisition windows 20 μs long;

An event was called “vetoed” if it occurred inside a time window 400 ns wide centered at the time of occurrence of the veto signal, otherwise it was “un-vetoed”.

5.2 Energy calibration

Before performing every measurement the T40 was calibrated. Vertically crossing muons were selected by a muon telescope, consisting on two plastic scintillators (20

X 20 cm^2 the upper one, 36 X 36 cm^2 the lower one, see chap. 3 fig. 3.1), each one monitored by one pmt Photonis XP3462.

The acquisition setup and the data analysis are here summarized:

1. the trigger was done by the coincidence among the 2 modules of the muon telescope ($\Delta t = 200$ ns, time width of pmts signal);
2. the trigger started the acquisition window 800 ns long;
3. the signals out-coming from the detector pmts were sampled (according to the DAQ setup) by the digital oscilloscope (if DAQ setup a), oscilloscope scale equal to 50 mV/division);
4. the pre-trigger region (200 ns long), where no events were supposed to be, was used to evaluate the baseline: after this the muon signal was found according to the used DAQ setup and its charge was measured. If DAQ setup a) was used, the charge was measured on the three pmts and then summed;
5. after saturated signals rejection, the charge distribution was fitted by the convolution between a Gaussian and a Landau function: the peak of that function was the energy calibration parameter Q_{data} ;
6. the energy calibration factor was given by the ratio $\frac{Edep_{sim}}{Q_{data}}$. $Edep_{sim}$ corresponds to the modal energy released by muons selected by the muon telescope and was found by simulation equal to 160 MeV (see chap. 4).

The relative uncertainty was given by:

$$\frac{\sigma_{CAL}}{CAL} = \sqrt{\left(\frac{\sigma_{Edep_{sim}}}{Edep_{sim}}\right)^2 + \left(\frac{\sigma_{Q_{data}}}{Q_{data}}\right)^2}$$

Since $\frac{\sigma_{Edep_{sim}}}{Edep_{sim}} \sim 2\%$ and $\frac{\sigma_{Q_{data}}}{Q_{data}} \sim 1\%$, the systematic energy uncertainty due to calibration was $\sim 2.5\%$.

Since the selected muons crossed the detector in a region close to the detector central point, there were no difference on energy calibration due to the used DAQ setup.

5.3 Background spectrum

Background spectrum was measured by acquiring randomly triggered windows $100 \mu\text{s}$ long by using the DAQ setup a) (oscilloscope scale equal to 2 mV/division).

230,274 gates have been acquired corresponding to $\sim 22.1 \text{ s}$ real time: the obtained cumulative integral background spectrum is reported in fig.5.2 together with the vetoed and the un-vetoed components.

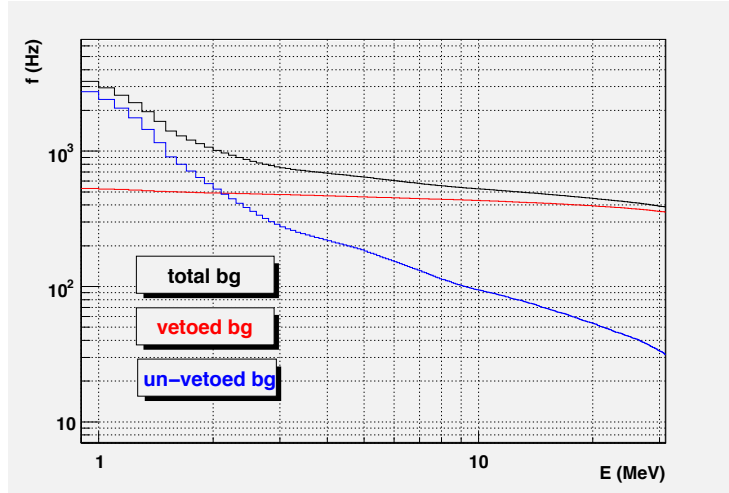


Figure 5.2: Cumulative integral background spectrum (in black) with vetoed component (in red) and un-vetoed component (in blue)

Fig.5.2 shows that the rate of vetoed signals with $E > 10 \text{ MeV}$ is:

$$R(E > 10 \text{ MeV}) = 432 \pm 5(\text{stat.}) \pm 1(\text{syst.}) \text{ counts } s^{-1}$$

This rate was used for normalizing the stopping muons rate as described in sec. 5.6. Vetoed signals are mainly due to atmospheric muons crossing the detector and the veto system and, concerning the lower part of the energy spectrum, electromagnetic component of EAS not necessarily accompanied by muons. From now these signals are called “muon candidates”, while un-vetoed signals are called “not-muon candidates”.

In order to evaluate the impact of DAQ setup changes on T40 background spectrum, the randomly triggered sampled waveforms were re-analyzed.

For each acquired window, the three pmts waveforms were summed and the resulting waveform was analyzed. The analysis criteria were the same used for all the measurements performed with DAQ setup b) (see sec. 5.1).

Fig.5.3 shows the obtained integral spectrum together with its vetoed and un-vetoed components.

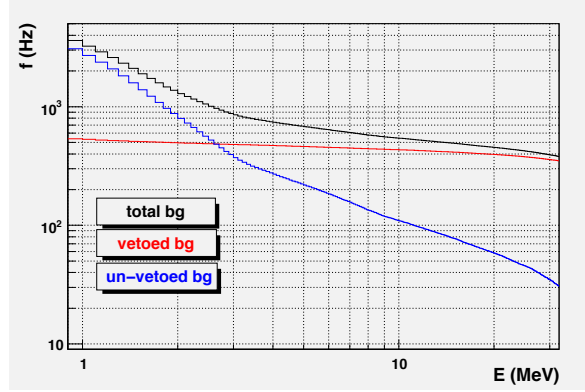


Figure 5.3: Cumulative background spectrum measured by summing T40 pmts

Tab. 5.1 collects the observed not-muon candidates counting rates for the “Single pmt” case (i.e. DAQ setup a)) and for the “ Σ pmts” case (i.e. DAQ setup b)).

Threshold	“ Σ pmts” (Hz)	“Single pmt” (Hz)
$E_{vis} > 3$ MeV	$368 \pm 4 \pm 20$	$276 \pm 4 \pm 11$
$E_{vis} > 5$ MeV	$216 \pm 3 \pm 4$	$183 \pm 3 \pm 4$
$E_{vis} > 10$ MeV	$108 \pm 2 \pm 2$	$94 \pm 2 \pm 2$
$E_{vis} > 13$ MeV	$87 \pm 2 \pm 2$	$78 \pm 2 \pm 1$
$E_{vis} > 15$ MeV	$76 \pm 2 \pm 2$	$69 \pm 2 \pm 1$

Table 5.1: Not-muon candidates rates for “ Σ pmts” (DAQ setup b)) and “Single pmt” (DAQ setup a)), statistical and systematic errors are reported too

Table 5.1 shows the not-muon candidates counting rates changed according to the DAQ setup used for performing the measurement.

In the “Single pmt” analysis (i.e. the DAQ setup a)), during which all the three pmts

were individually considered, events were found by 3-fold coincidence among the three pmts to reject spurious signals (i.e. “after-pulse” signals and ptms noise). Also the “single pmt” algorithm was used to correct energy overestimation due to detector geometry [43] and that was very useful to reduce background counting rate.

When only the sum of the three pmts was analyzed (i.e. the DAQ setup b)) the “single pmt” algorithm could not be used anymore and, therefore, the background counting rate increased, especially in the low energy region.

The not-muon candidates rates for energy above 5 and 13 MeV shown in tab. 5.1 have been used for normalizing the the atmospheric neutrons flux as described in sec. 5.5.

Finally, a further short background measurement was performed by using the DAQ setup b) in order to check its correct working: 9,900 randomly triggered windows 100 μ s long have been collected corresponding to ~ 0.94 s real time. The cumulative background spectra for all the three oscilloscope scales are reported in fig.5.4 (the total background) and in fig 5.5 (only the not-muon candidates).

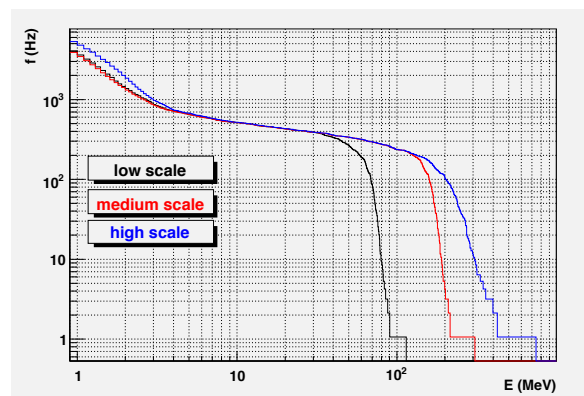


Figure 5.4: Cumulative background spectrum measured in 3 different oscilloscope amplification scale values

The spectra in fig. 5.4-5.5 show a good agreement between all the different oscil-

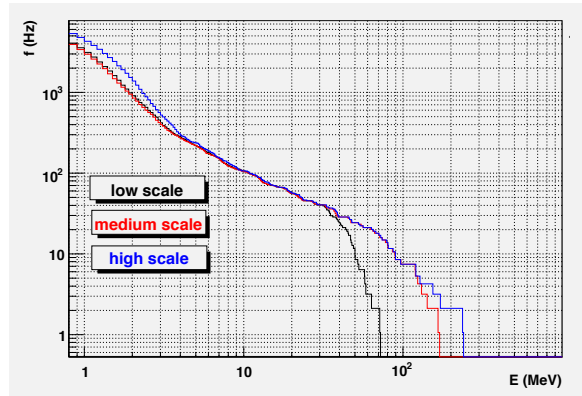


Figure 5.5: Not-muon candidates cumulative spectrum measured in 3 different oscilloscope amplification scale values

loscope scales until their saturation but the higher scale for $E < 4$ MeV: this effect was due probably to the low resolution of the highest oscilloscope scale and it shows why the energy value considered for each event was the one given by the most precise not-saturated one. Fig.5.4-5.5 are also in good agreement with the spectra shown in fig.5.3.

Furthermore, tab. 5.1 and fig. 5.2-5.5 show not-muon candidates T40 counting rate for $E > 5$ MeV was considerably high, it could mean:

1. the veto apparatus was strongly inefficient;
2. there was a large neutral component (i.e. neutrons and/or gammas) in the background spectrum beyond natural radioactivity that ends for $E \sim 4$ MeV.

5.4 Veto Efficiency Check

Since the actual possibility to perform measurement about stopping muons and (especially) atmospheric neutrons fluxes strictly depended on veto efficiency, the veto efficiency was performed by measuring the stopping muon rate.

Stopping muons are one of the background components for a detector and particularly for a surface one because the muon flux is very large ($\sim 200 \text{ muons } m^{-2}s^{-1}$

at sea level). Nevertheless they can be used to calibrate and check the experimental apparatus because their characteristic signal inside the detector: a first vetoed signal is followed by a second un-vetoed one due to muon decay at rest (mean life = $2.2 \mu\text{s}$, electron/positron mean energy $\sim 37 \text{ MeV}$).

The technique used for performing this measurement was to observe a first signal due to a muon followed by an other one due to the Michel e^\pm which is produced by muon decay at rest inside the detector. Therefore the delayed signal had to be a not-muon candidate because its probability to be detected by the surrounding veto was negligible .

If the veto would have been fully efficient, no muon decay signal was expected to be after a not-muon candidate prompt signal. Muon decay signals were searched inside two different sets of data: the first one was collected by triggering on muon candidates, the second one by triggering on not-muon candidates. For performing this measurement the DAQ setup b) was used.

The second set of data here described was re-analyzed for performing the measurement of the atmospheric neutrons flux (see sec. 5.5). A more precise measurement of stopping muons rate is described in sec. 5.6.

The trigger

The trigger was designed for selecting muon candidates and not-muon candidates with an energy threshold $\sim 4.5 \text{ MeV}$. The trigger setup is here summarized:

1. the signals of the 8 modules of the veto (NB Top1 and Top2 were dealt as a one single module, see chap. 3 sec. 3.2) were discriminated and collected in an “OR” logical pattern (*signal 1*);
2. the signals coming out from last dynode of T40 pmts were amplified, discriminated at a threshold equal to $\sim 4.5 \text{ MeV}$, and collected in a 3-fold coincidence (*signal 2*), $\Delta t = 200 \text{ ns}$;

- the trigger was done by the coincidence ($\Delta t = 250$ ns) of *signal 1* and *signal 2* (muon candidates, fig.5.7) or of $\overline{\text{signal 1}}$ and *signal 2* (not-muon candidates, fig.5.6).

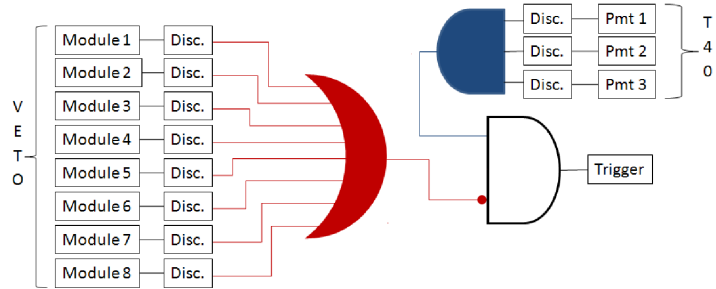


Figure 5.6: Logic diagram of not-muon candidates trigger

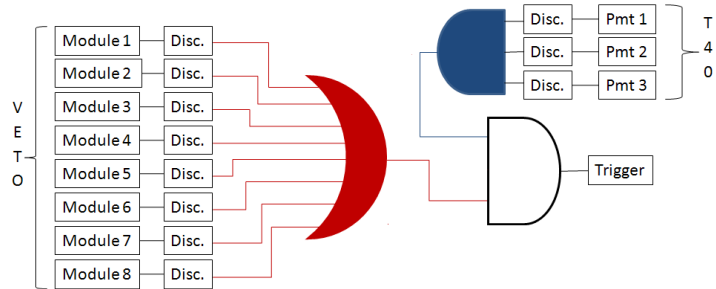


Figure 5.7: Logic diagram of muon candidates trigger

Data collection and analysis

The measurement setup is here summarized:

- the trigger started the acquisition window $100 \mu\text{s}$ long: the first $2.4 \mu\text{s}$ (where no events were supposed to be) were used to evaluate the baseline on each channel, the last $97.6 \mu\text{s}$ were used for the research prompt and delayed signals;
- energy cuts:

- a. prompt signals were required to be muon/not-muon candidates and corresponding to a released energy above 5 MeV;
- b. delayed signals were required to be not-muon candidates with a delay respect to the prompt $480 \text{ ns} \leq \Delta t < 10 \text{ } \mu\text{s}$ and with a released energy $15 \text{ MeV} < E < 60 \text{ MeV}$.

The energy cuts on delayed signals were set for rejecting neutron captures from μ -decay candidate signals. In fact, due to the reduced energy resolution at low energy of DAQ setup b), neutron captures could occur up to $E = 15 \text{ MeV}$. This is important in both the acquired set of data: for the first one because neutrons can occur together with muons in EAS (*Extensive Air Showers*), for the second one (“not-muon candidates”) because neutrons are expected to be a large component of T40 neutral background (see sec. 5.5).

Results

In the first set of data, 28,532 muon candidates with energy above 5 MeV have been acquired, 501 among them was followed by at least one delayed signal (~ 15 are the expected random coincidence). After random coincidence subtraction, the number of found stopping muons was equal to 1.71% of muon candidates.

In the second set of data, 90,991 not-muon candidates with energy above 5 MeV have been acquired, 93 of them followed by at least one delayed signal (~ 40 are the expected random coincidence). After random coincidence subtraction, the number of found stopping muons was equal to 0.056% of not-muon candidates.

The time delay distributions (renormalized to the same number of prompt signals) of delayed signals following a muon/not-muon candidate are shown in fig. 5.8-5.9. In fig. 5.8 an ”exponential + constant” fit is also drawn.

Therefore the muon contamination in not-muon candidates has been evaluated equal to $\frac{0.056}{1.71} \sim 3.3\%$. Since the muon candidates and not-muon candidates count-

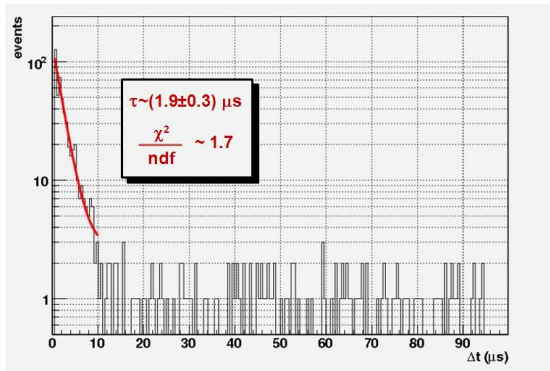


Figure 5.8: Time delay distribution of 15 MeV < E < 60 MeV un-vetoed signals after muon-candidate prompt signal

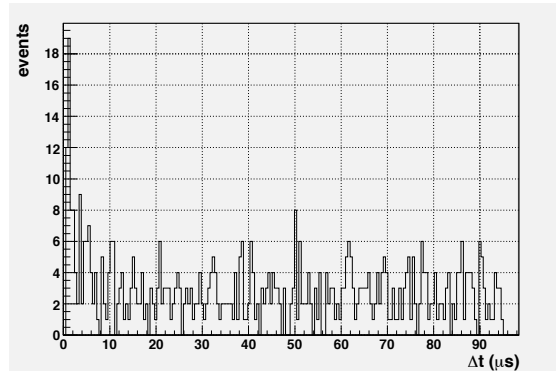


Figure 5.9: Time delay distribution of 15 MeV < E < 60 MeV un-vetoed signals after not muon-candidate prompt signal

ing rates for energy above 5 MeV was found equal to 456 and 216 counts s^{-1} (see fig. 5.3), the veto inefficiency (i.e. the probability for a crossing muon to go undetected by the veto system) has been evaluated equal to $\frac{3.3\% \cdot R_{not-muon}}{R_{muon} + 3.3\% \cdot R_{not-muon}} \sim 1.5\%$.

Since in the acquired data there was no rejection of after-pulse signals, the obtained result has to be interpreted as an upper limit. In fact, the time delay distribution for $\Delta t < 10 \mu s$ shown in fig. 5.9 is more similar to an after-pulse signals time distribution than a muon decay one.

5.5 Atmospheric Neutrons Flux

Atmospheric neutrons are a very important neutral background component for a surface detector. They are very nasty especially for $\bar{\nu}_e$ surface detectors because they can mimic the IBD reaction: a first elastic scattering on a proton can be followed by a neutron capture.

Nothing is possible to do for disentangling the two different interactions but the “pulse-shape” technique. It allows, by discriminating heavy particles from light ones, to disentangle e^+ prompt signals from the proton ones, i.e. IBD reactions from atmospheric neutrons background.

The efficiency of this technique varies from detector to detector: unfortunately the

white-spirit scintillator has a very poor discrimination efficiency.

The measurement of atmospheric neutron flux was performed by looking for a double un-vetoed signal in a $95 \mu s$ gate: the first one due to a recoiling proton, the second one due to (n Gd) neutron capture. The mean neutron capture time in this detector was measured equal to $25 \pm 1 \mu s$ [50].

The atmospheric neutrons flux was measured by re-analyzing the second set of data used in sec. 5.4, i.e. the waveforms acquired by triggering on not-muon candidates.

The analysis

The analysis cuts are here summarized:

1. prompt signals were required to be not-muon candidates and corresponding to a released energy above 5 MeV;
2. delayed signals (supposed to be due to neutron captures) were required to be not-muon candidates, with a delay respect to the prompt $480 \text{ ns} \leq \Delta t < 95 \mu s$ and with a released energy $3 \text{ MeV} < E < 10 \text{ MeV}$.

Results

90,991 not-muon candidate prompt signals with visible energy above 5 MeV have been collected and, among them, 8,160 were followed by at least one delayed signal which are called from now “neutron capture candidates” (the expected chance coincidences by background measurement shown in sec. 5.3 were ~ 2220). Not-muon candidate prompt signals followed by at least one neutron capture candidates are called from now “neutron candidates”.

The visible energy spectra of not-muon candidate prompt signals (in black) and neutron candidates (in red) are drawn in fig. 5.10.

In fig. 5.11 the energy spectrum of neutron capture candidates is reported together

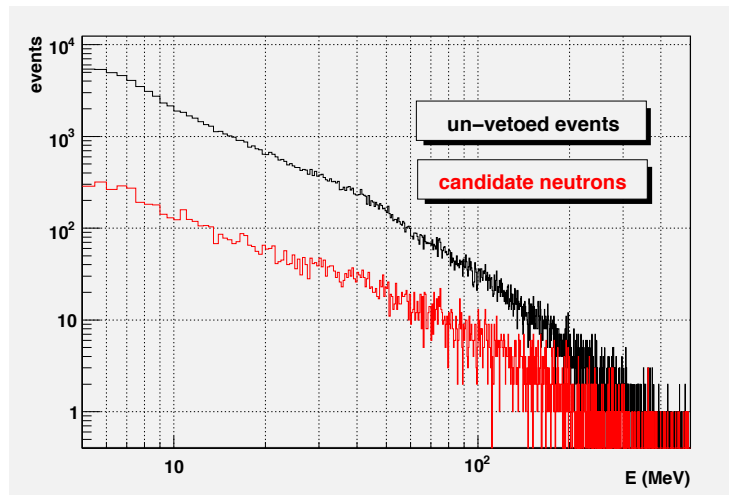


Figure 5.10: Visible energy spectra of not-muon candidate prompt signals (black line) and neutron candidates (red line)

with the expected background (coming from background measurement shown in sec. 5.3). In fig. 5.12 the time distribution of neutron capture candidates is shown together with an "exponential + constant" fit. The slope of the fitted function has been found equal to $\tau = 24.6 \pm 1.5 \mu\text{s}$ in good agreement with the mean capture time for thermal neutrons given by [50] and [52].

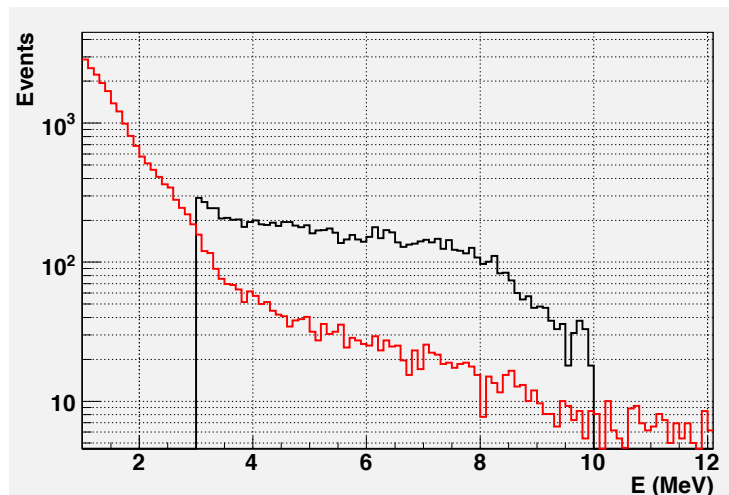


Figure 5.11: Neutron capture candidates energy spectrum, background in red

After subtracting the chance coincidences and normalizing to the not-muon candi-

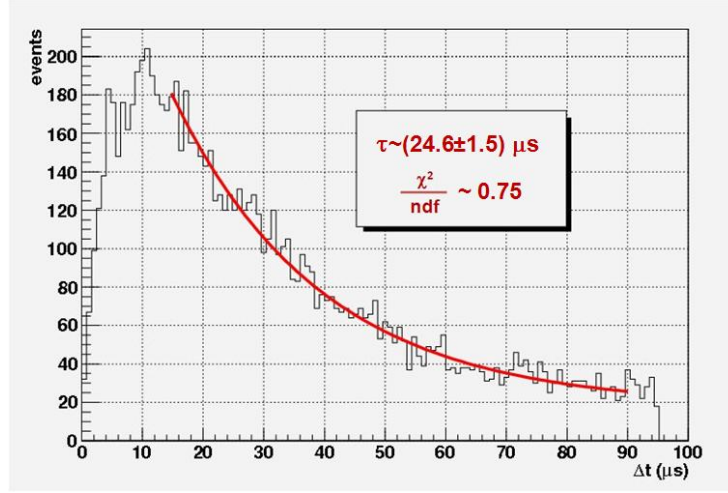


Figure 5.12: Candidates neutron captures time delay distribution

dates counting rate, the observed neutron rate for $E_{vis} \geq 5$ MeV is:

$$\Phi_{neutron}(E_{vis} \geq 5 \text{ MeV}) = 14.10 \pm 0.25(\text{stat.}) \pm 0.59(\text{syst.}) \text{ neutron s}^{-1}.$$

In fig. 5.13 the visible energy spectrum of neutron candidates (after background subtraction and normalization to the not-muon candidates counting rate) is shown.

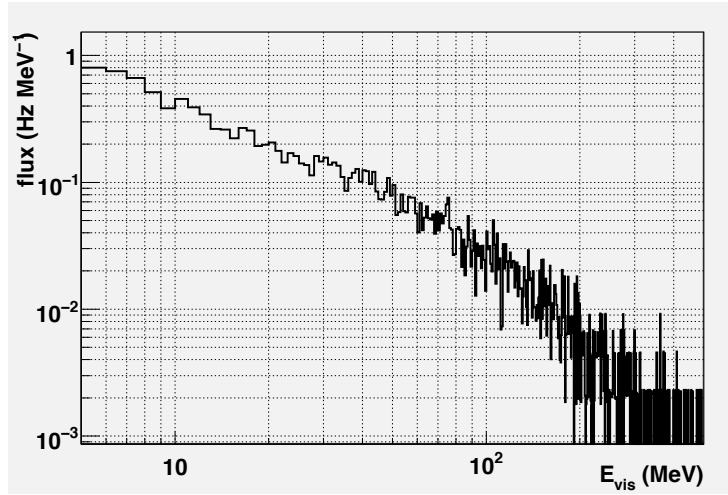


Figure 5.13: Neutron candidates visible energy spectrum, subtracted background and normalized to the not-muon candidates counting rate

In order to obtain the atmospheric neutron absolute flux, it was necessary to correct the experimental rate:

1. by taking into account the quenching effect of *white-spirit* liquid scintillator for recoiling protons (see Tab. 5.2);
2. by taking into account the trigger efficiency (i.e. the efficiency of neutron capture detection and the probability for an impinging neutron to be captured);
3. by scaling the neutron rate to the detector acceptance.

A Geant4 MC simulation code, described in chap. 4 sec.4.6, was used for this purpose.

The T40 acceptance has been found equal to $1.55 m^2$. The visible energy spectrum of neutron candidates (after background subtraction and acceptance normalization) and of “selected neutrons” coming out from simulation are shown in fig. 5.14.

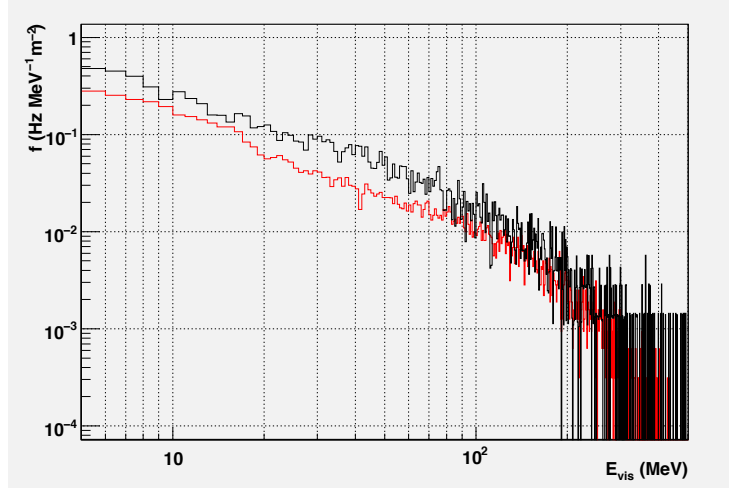


Figure 5.14: “Neutron candidates” visible energy spectrum subtracted background (black line), simulated “selected neutrons” (red line)

By comparing the integral of the two spectra shown in fig.5.14 for $E_{vis} > 5$ MeV and for $E_{vis} > 13$ MeV (quenching factor for 10 MeV and 20 MeV protons is ~ 2 and ~ 1.5 ., see Tab. 5.2), the neutron flux has been estimated equal to:

$$\Phi_{neutron}(E > 10MeV) = 75 \text{ neutron } s^{-1}m^{-2}$$

$$\Phi_{neutron}(E > 20MeV) = 52 \text{ neutron } s^{-1}m^{-2}$$

Since it was not possible to apply the “single pmt” algorithm to the atmospheric neutrons data, the obtained results were overestimated. In order to correct this overestimation, the obtained values were rescaled to the ratio of background counting rates observed in the two different DAQ setup configurations for $E_{vis} > 5$ MeV and $E_{vis} > 13$ MeV (see tab. 5.1 sec. 5.3).

In this way, the final neutron flux has been finally estimated equal to:

$$\Phi_{neutron}(E > 10MeV) = 63 \pm 6 \text{ neutron } s^{-1}m^{-2}$$

$$\Phi_{neutron}(E > 20MeV) = 47 \pm 5 \text{ neutron } s^{-1}m^{-2}$$

5.6 Stopping Muons

Muon candidates counting rate for energy above 10 MeV was obtained in sec. 5.3: the following step was to perform the measurement of stopping muons absolute rate. In this section the measurement of stopping muons absolute rate inside the detector for muons with energy above 10 MeV is described.

The DAQ setup a) was used for performing the measurement (oscilloscope scale equal to 30 mV/division).

The trigger

The trigger was aimed to select muon candidates with energy above ~ 4.5 MeV and was the same used for testing veto efficiency (see sec. 5.4):

1. the signals of the 8 active veto modules were discriminated and the obtained 8 output logic signals were collected by an “OR” logical pattern (*signal 1*);
2. the amplified signal coming out from last dynode of each pmt was discriminated at threshold value corresponding to ~ 4.5 MeV. The 3 coming out logic signals were collected in a 3-fold coincidence (*signal 2*), $\Delta t = 200$ ns;

3. the trigger was done by the coincidence of *signal 1* and *signal 2* (see fig.5.7), $\Delta t = 250$ ns.

Since the active muon veto surrounded 4π T40 and it was formed by 8 independent modules, it could seem strange not to use the veto modularity to disentangle μ -stop candidates from thoroughgoing muons by requiring that only one, among the 6 walls, to be triggered. The reason why this trigger has not been considered was that it would have rejected multiple muons belonging to EAS where μ -stop events may occur.

Data collection and analysis

The measurement setup is here summarized:

1. the trigger started the acquisition window $20 \mu s$ long: the first $2.4 \mu s$ (where no events were supposed to be) were used to evaluate the baseline on each channel, the last $17.6 \mu s$ were used for the research of prompt and delayed signals;
2. energy cuts:
 - a. prompt signals were required to be muon candidates and corresponding to a released energy above 5 MeV;
 - b. delayed signals were required to be not-muon candidates with a delay respect to the prompt $480 \text{ ns} \leq \Delta t < 10 \mu s$ and with a released energy $10 \text{ MeV} < E < 60 \text{ MeV}$.

Results

229,897 muon candidate prompt signals of energy above 10 MeV have been collected and, among them, 5,205 were followed by at least one delayed signal (~ 200 are the expected random coincidence) which are called from now “Michel electron candidates”. Prompt signals followed by at least one Michel electron candidate are called from now “ μ -stop candidates”. In fig. 5.15 the energy spectra of prompt signals (in black) and

μ -stop candidates (in red) are shown.

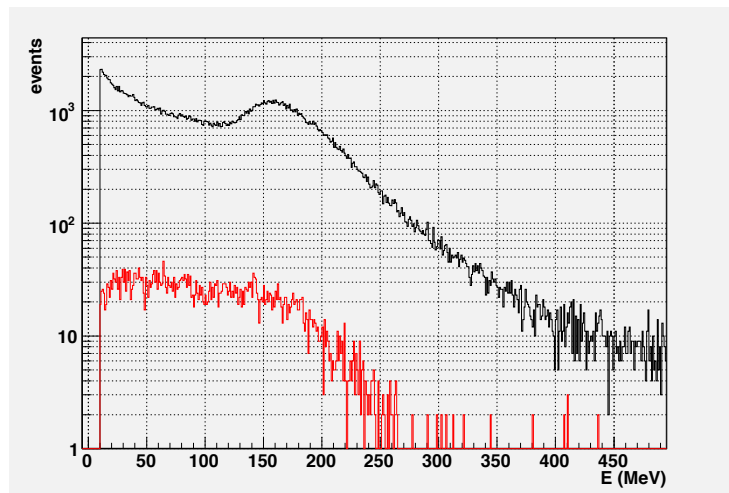


Figure 5.15: Energy spectrum of prompt signals (in black) and μ -stop candidates (in red)

The cumulative energy spectrum of prompt signals is reported in fig. 5.16 together with the muon candidate component of cumulative background spectrum (the two spectra have been re-normalized at the same value for $E=10\text{MeV}$). Fig. 5.16 shows that, in spite of the “hardware” threshold and the different oscilloscope scales used during the measurements of background spectrum and stopping muons rate, the largest difference between the two spectra in the energy region $5\text{ MeV} < E < 30\text{ MeV}$ is equal to 1.5% (for $E < 5\text{ MeV}$ there is heavy threshold effect for prompt signals, whereas for $E > 30\text{ MeV}$ the background spectrum begins to saturate). Thereby, any significant deformation on muon candidates energy spectrum due to the trigger selection has been excluded.

In fig. 5.17 the energy spectra of delayed signals with (in black) and without energy cut (in blue) and the expected background (in red) are shown. By observing the histograms shown in fig. 5.17 the energy cuts on delayed signals could seem strange. In fact, by assuming a total Poissonian behaviour of the measured background (see sec. 5.3), in the energy region $3\text{ MeV} < E < 10\text{ MeV}$ the expected background was considerably lower than the observed flux of delayed signals.

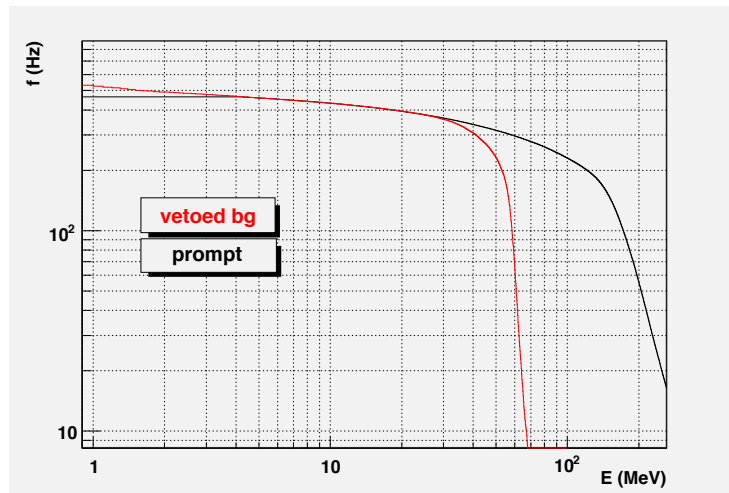


Figure 5.16: Cumulative prompt signals spectrum (in black), cumulative vetoed background spectrum (in red)

The reason why delayed events with energy below 10 MeV were rejected consisted on the fact that background not-muon candidate energy spectrum for $E \lesssim 10$ MeV is partially due to (n Gd) captures. Neutrons may be present in EAS or produced by muon itself inside the detector. This will be discussed in more detailed way in the next sec. 5.7.

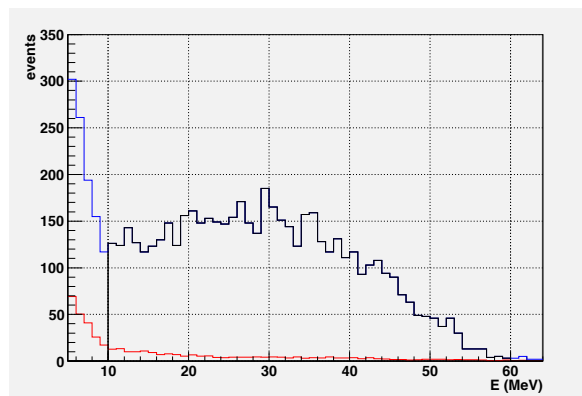


Figure 5.17: Energy spectrum of Michel electron candidates (in black), all delayed signals (in black) and expected background (in red)

In fig. 5.18 the observed time distribution of Michel electron candidates is shown

together with an "exponential + constant" fit: the slope of fitted function gave the muon mean life equal to $2.12 \pm 0.07 \mu s$.

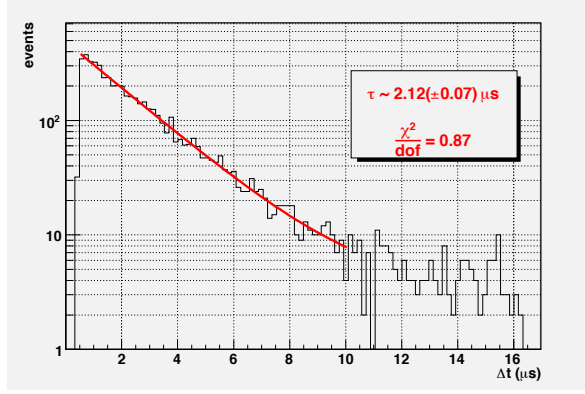


Figure 5.18: Selected delayed signals time distribution

After random coincidence subtraction and before further corrections (death time, energy cuts, electromagnetic contamination in muons spectrum), the observed stopping muons rate for $E_\mu > 10$ MeV is equal to $2.18 \pm 0.03\%$ (stat.) $\pm 0.01\%$ (syst.) of total vetoed events, corresponding to 9.43 ± 0.17 (stat.) ± 0.05 (syst.) μ -stop s^{-1} .

The efficiency due to energy cuts on Michel electron candidates was found by MC simulation equal to $\epsilon_E = 85.5 \pm 1.0 \pm 0.5\%$ (see chap. 4 sec. 4.4), whereas the efficiency in the research of Michel electron candidates due to the time selection was defined equal to

$$\epsilon_t = \int_{t_1=480ns}^{t_2=10\mu s} \frac{e^{-t/\tau}}{\tau} dt = 78.9\%$$

So the real stopping muon rate for energy above 10 MeV is:

$$Rate(E_\mu > 10MeV) = \frac{R(E_\mu > 10MeV)}{\epsilon_E \epsilon_t} = 13.98 \pm 0.30 (stat.) \pm 0.04 (syst.) \text{ events } s^{-1}$$

The considered systematic error was due to energy calibration.

5.7 Muon mean life and Michel spectrum

In this section the measurement of muon mean life in liquid scintillator is described. For muon mean life in liquid scintillator and Michel spectrum measurement it was extremely important to have a very large statistics and, consequently, to maximize the trigger efficiency in rejecting background. Therefore the DAQ setup a) and the trigger were slightly changed.

The trigger

The used trigger is here summarized:

1. the signals of all the 8 active veto modules were discriminated;
2. the 8 logic signals were collected by 2 different logic patterns: the first one, *signal 1*, was an “OR” on the 8 logic signals, the second one, *signal 2*, was a “majority” with threshold equal to 2 (i.e. the logic output was “TRUE” only if there was a coincidence of at least 2 signals);
3. the signals coming out from last dynode of T40 pmts were amplified, discriminated and collected in a 3-fold coincidence ($\Delta t = 200$ ns), *signal 3*;
4. the trigger was done by the 3-fold coincidence ($\Delta t = 250$ ns) of *signal 1*, $\overline{\text{signal 2}}$ and *signal 3* as shown in fig. 5.19

Muon candidates triggering only one module of the veto are called from now “single-triggering events”.

DAQ setup

The DAQ setup a) was used for performing this measurement (oscilloscope scale equal to 30 mV/division) but the fourth oscilloscope channel was used for collecting the majority analogical signal instead of veto one. In this way it was possible to select single-triggering events during the data analysis.

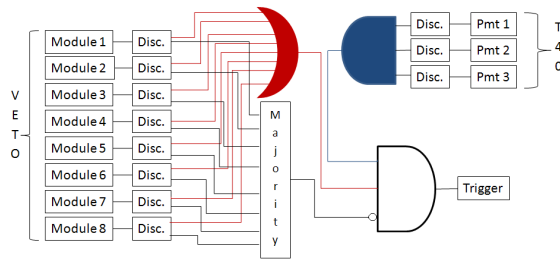


Figure 5.19: Logic diagram of μ -stop DAQ

The Data collection and analysis

The measurement setup was almost the same used in the previous case. The only difference was that prompt signals were requested to be single-triggering events and not only muon candidates.

580,160 single-triggering prompt signals of energy above 10 MeV have been collected and, among them, 76,325 were followed by at least one Michel electron candidate (~ 500 are the expected random coincidence). The large difference between the number of “single-triggering events” and the number of events followed by a Michel electron candidate is mainly due to electron/positron contamination of low energy muon candidates energy spectrum and, in last resort, to the geometrical inefficiency of the veto, especially in the Bottom module (see chap. 3 Tab. 3.2).

The energy spectrum of Michel electron candidate is reported in fig. 5.20 together with the previously measured one (after re-normalization) and the expected background (which has been subtracted for a better comparison). The $\widetilde{\chi^2}$ computed on the difference of the two spectra has been found equal to 1.35, in agreement with the assumption there was no distortion effect on the energy spectrum of Michel electron candidates due to the used trigger.

In fig. 5.21 the delay distribution of Michel electron candidates is reported together with an “exponential + constant” fit. The obtained muon mean life value is

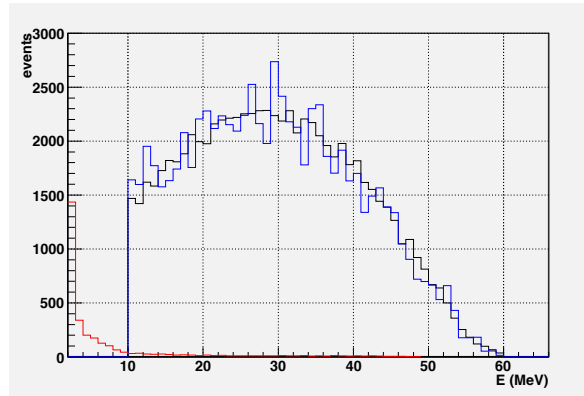


Figure 5.20: Energy spectrum of Michel electron candidates in black with the expected background in red. Energy spectrum of Michel electron candidates measured in sec. 5.6 is reported in blue

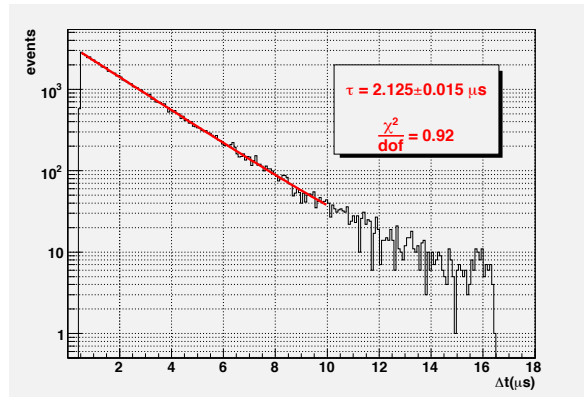


Figure 5.21: Michel electron candidates time delay distribution

$$2.125 \pm 0.015 \mu s$$

in good agreement with the previous one (see sec. 5.6).

Fig. 5.22 shows the low energy region of the delayed signal energy spectrum together with the expected background. In fig. 5.23 the time distribution of delayed pulses in the energy window energy $3 \text{ MeV} < E < 10 \text{ MeV}$ is reported.

Fig.5.23 shows 2 different regions: the μ -decay exponential region for $\Delta t < 4 \mu s$ and the background region for $\Delta t > 4 \mu s$. This last region presents a slight slope probably due to neutron capture contamination: unfortunately the acquisition window

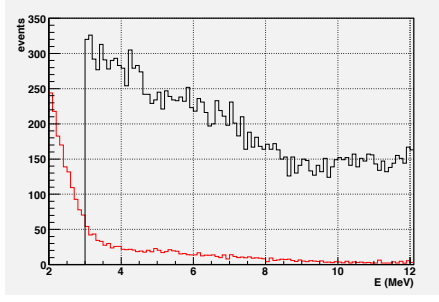


Figure 5.22: Low energy delayed signals, background in red

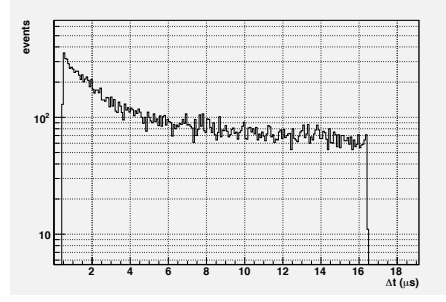


Figure 5.23: Low energy delayed signals time distribution

was not long enough for fitting it with an exponential function with $\tau \sim 25 \mu s$ (which is the mean capture time for thermal neutrons [52] in a LVD counters filled with 0.1% Gd doped liquid scintillator). This is the reason why this energy region was not considered during the research of Michel electron candidates.

5.8 Conclusions

By using a detector composed by a LVD counter filled with 1.2 tons of 0.1% Gd doped *white-spirit* liquid scintillator and an active muon veto, located in the INFN Gran Sasso National Laboratory external site (42° 25' 11" N, 13° 31' 2" E, altitude 970 m a.s.l.), the following results have been obtained:

1. the following atmospheric neutrons fluxes:

$$\Phi_{neutron}(E > 10MeV) = 63 \pm 6 \text{ neutron } s^{-1}m^{-2}$$

$$\Phi_{neutron}(E > 20MeV) = 47 \pm 5 \text{ neutron } s^{-1}m^{-2}$$

2. the stopping muon rate for energy above 10 MeV:

$$Rate(E_{\mu} > 10MeV) = 13.98 \pm 0.30 (stat.) \pm 0.04 (syst.) \text{ events } s^{-1}$$

3. the muon mean life in liquid scintillator:

$$\tau = 2.125 \pm 0.015 \mu s$$

These results have been presented during the 31st ICRC [56].

The observed muon mean life in T40 liquid scintillator (C_nH_{2n}) is in good agreement with the values reported by Suzuki *et al.* [57], even if a direct comparison is not possible to do: in [57] the authors only reported the μ^- mean life in several pure elements. The reported μ^- mean life in Carbon is $\sim 2.02 \mu s$ and in Hydrogen is $\sim 2.20 \mu s$: supposing $\frac{\mu^+}{\mu^-} = 1$ and taking into account the ratio of mass abundance of Hydrogen and Carbon inside the liquid scintillator (C_nH_{2n}), the expected muon mean life value is $2.12 \mu s$.

The observed atmospheric neutron flux values are $\sim 40\%$ larger than the results obtained at a similar altitude in Japan ($35^\circ 22' N$, $138^\circ 43' E$, altitude 1020 m a.s.l.) reported by Kowatari *et al.* [54] and Nakamura *et al.* [53]. The explanation of this broad difference consists on the different geo-magnetic latitude, the different period in the solar activity cycle and in the different technique used for performing this measurement. Kowatari *et al.* performed their measurement on September 2002 [54] during solar maximum activity in Japan by using a “Bonner multi-sphere neutron spectrometer”, while the present measurement was performed in Italy by using a liquid scintillator detector on November 2008 i.e. during solar minimum activity. A Bonner multi-sphere neutron spectrometer consists on several Bonner spheres shielded by different layers of a moderator material (polyethylene in this case) which are able to detect neutrons but not to give any estimation of their energy: the cosmic-ray neutron energy spectrum is obtained by unfolding the measured counting rates by using an appropriate code (SAND II [58] in this case) and an initial guess spectrum [54].

The present measurement was aimed to observe the energy of protons scattered by a neutron which was subsequently captured. Therefore the present measurement was almost calorimetric and it did not need any “a priori” guess spectrum.

Up to now *there are no other calorimetric measurement of atmospheric neutrons besides the present one.*

Kin. Energy (MeV)	protons	alphas	deuterons	tritium
1.0	0.230	0.020	0.150	0.1100
2.0	0.310	0.040	0.220	0.1800
4.0	0.390	0.080	0.270	0.2300
6.0	0.450	0.100	0.320	0.2600
8.0	0.500	0.120	0.350	0.2900
10.0	0.534	0.140	0.380	0.3100
12.0	0.565	0.155	0.412	0.3330
16.0	0.625	0.180	0.466	0.3600
20.0	0.664	0.202	0.520	0.3900
28.0	0.750	0.248	0.592	0.4400
30.0	0.764	0.260	0.620	0.4500
40.0	0.850	0.314	0.710	0.5100
58.0	0.950	0.386	0.810	0.6000
70.0	0.980	0.435	0.870	0.6500
90.0	1.000	0.515	0.930	0.7400
100.0	1.000	0.550	0.944	0.7800
140.0	1.000	0.670	0.980	0.8750
160.0	1.000	0.720	0.994	0.9200
200.0	1.000	0.800	1.000	0.9700
220.0	1.000	0.835	1.000	0.9800
240.0	1.000	0.865	1.000	0.9900
260.0	1.000	0.890	1.000	0.9930
280.0	1.000	0.910	1.000	0.9965
300.0	1.000	0.925	1.000	1.0000
320.0	1.000	0.944	1.000	1.0000
350.0	1.000	0.965	1.000	1.0000
400.0	1.000	1.000	1.000	1.0000

Table 5.2: Quenching factor for protons, deuterons, tritiums, alphas in *white-spirit* liquid scintillator

Bibliography

- [1] D. .M. Mei and A. Hime (2006), *Phys. Rev. D* 73, 053004
- [2] H. Wulandari (2004), *hep-ex/0132050. v2*
- [3] P. Belli *et al.* (1989), “Deep underground Neutron Flux Measurement with Large BF_3 Counters”, *Il Nuovo Cimento Vol. 101 A, N.6, 959-966*
- [4] F. Arneodo *et al.* (1997), “Underground neutron spectrometry with a liquid scintillator detector”, *INFN/AE-97/52*
- [5] M. J. Carson *et al.* (2004), *Astroparticle Physics* 21, 667
- [6] V. A. Kudryavtsev *et al.* (2003), “Simulations of muon-induced neutron flux at large depths underground”, *NIM A* 505, 688-698
- [7] P. Goldhagen *et al.* (2002) “Measurement of the energy spectrum of cosmic-ray induced neutrons aboard an ER-2 high-altitude airplane”, *NIM A* 476, 42â51
- [8] S. Roesler, W. Heinrich, H. Schraube (1998), *Radiat. Res.* 149, 87
- [9] A. Kurochkin *et al.* (1999), *Radiat. Prot. Dosim.* 83, 281
- [10] T. W. Armstrong *et al.* (1973), *J. Geophys. Res.* vol. 78, 2715
- [11] A. Preszler *et al.* (1974), *J. Geophys. Res.*, vol. 79, 17
- [12] F. Albernhe *et al.* (1971), *Ann. Geophys.*, vol.27, 339

- [13] U. Bravar *et al.* (2005), “*Atmospheric Neutron Measurements with the SONTRAC Science Model*”, *2005 IEEE Nuclear Science Symposium Conference Record N14-126*
- [14] J. F. Ziegler and W. A. Lanford (1979), “*Effect of Cosmic Rays on Computer Memories*”, *Science*, vol. 206, pp. 776-788
- [15] D. O’Sullivan *et al.* (1999), “*Cosmic rays and dosimetry at aviation altitudes*”, *Rad. Meas.* vol. 31, 579-584
- [16] A. Bernstein *et al.* (2002) “*Nuclear reactor safeguards and monitoring with antineutrino detectors*”, *Journ. Appl. Phys.* Vol 91, N. 7
- [17] L. Forman *et al.* (2004), “*Distinguishing spontaneous fission neutrons from cosmic-ray background*” *Proc. SPIE*, vol. 5541, pp. 27-36
- [18] J. F. Valdez-Galicia *et al.* (2009), “*Solar neutron events as a tool to study particle acceleration at the Sun*”, *J. Adv. Space Res.* 43 565â572
- [19] J. F. Valdez-Galicia *et al.* (2004), “*An improved solar neutron telescope installed at a very high altitude in Mexico*”, *NIM A* 535, 656-664
- [20] S. Shibata (1994), *J. Geophys. Res.* 99 6651
- [21] A. Chilingarian and N. Bostanjyan (2009), “*On the relation of the Forbush decreases detected by ASEC monitors during the 23rd solar activity cycle with ICME parameters*”, *J. Adv. Space Res.* doi:10.1016/j.asr.2009.09.001
- [22] H. S. Ahluwalia *et al.* (2009), “*Two intense Forbush decreases of solar activity cycle 22*”, *J. Adv. Space Res.* 44, 58-63
- [23] K. Watanabe *et al.* (2006), “*Solar neutron events in association with large solar flares in November 2003*”, *J. Adv. Space Res.* 38, 425-430
- [24] Ch. Kraus *et al.* (2005), *Eur. Phys. J. C* 40 447
- [25] V. M. Lobashev *et al.* (1999), *Phys. Lett. B* 460 227

- [26] <http://map.gsfc.nasa.gov/news/>
- [27] R. Bernabei *et al.* (2008), *Eur. Phys. J. C* 56 333-355
- [28] J. March-Russell *et al.* (2009), “Inelastic dark matter, non-standard halos and the DAMA/LIBRA results” *Jour. High. En. Phys.* 05
- [29] R. Gaitskell, V. Mandic, J. Filippini <http://dmtools.brown.edu/>
- [30] D. Smith and N. Weiner (2001), “Inelastic dark matter”, *Phys. Rev. D* 64 043502 [[hep-ph/0101138](http://arxiv.org/abs/hep-ph/0101138)]
- [31] J. Diemand *et al.* (2007), “Dark matter substructure and gamma-ray annihilation in the Milky Way halo”, *Astrophys. J.* 657 262 [[astro-ph/0611370](http://arxiv.org/abs/astro-ph/0611370)]
- [32] J. I. Read *et al.* (2008), “Thin, thick and dark discs in LCDM”, [arXiv:0803.2714](http://arxiv.org/abs/0803.2714)
- [33] V. Sanglard *et al.* (2005), *Phys. Rev. D* 71 122002
- [34] J. Angle *et al.* (2008), *Phys. Rev. Lett.* 100 021303
- [35] M. Aglietta *et al.* (1998), *Phys. Rev. D* 58 092005
- [36] R. Bernabei *et al.* (2008), *Nucl. Instr. & Meth. A* 592 297-315
- [37] <http://www.cresst.de/>
- [38] G. Angloher *et al.* (2005), *Astroparticle Physics* 23, pp. 325-339
- [39] <http://lngs.infn.it/>
- [40] <http://warp.lngs.infn.it/>
- [41] P. Benetti *et al.* (2008), “First results from a Dark Matter search with liquid Argon at 87 K in the Gran Sasso Underground Laboratory”, *Astroparticle Physics* 28, pp. 495-507
- [42] <http://xenon.astro.columbia.edu/>

- [43] A. Porta *phD Thesis* (2005), “Energy measurement in LVD to reconstruct Supernova neutrino emission”
- [44] LVD Collaboration (1999), *XXVI ICRC Proceeding, H.E. 3.1.15*
- [45] N. Aganofonova *et al.* (2009), *Bulletin of the R. A. S.: PH. Vol. 73 No.5, 628-629*
- [46] M. Aglietta *et al.* (1994), *Astropart. Phys. 2, 103*
- [47] F. Arneodo and W. Fulgione (2009), “A low background facility inside the LVD detector at Gran Sasso”, *JCAP02 28*
- [48] M. Selvi, LVD collaboration <http://arxiv.org/pdf/0811.2884>
- [49] C. L. Cowan, Jr., F. Reines, F. B. Harrison, H. W. Kruse and A. D. McGuire (1956) “*Detection of the Free Neutrino: A Confirmation*”, *Science 124, 103*
- [50] I. R. Barabanov *et al.*, arXiv:0803.1577
- [51] A. Strumia, F. Vissani (2003), “*Precise quasielastic neutrino/nucleon cross section*”, *Astro-ph/0302055*
- [52] N. A. Danilov *et al.* (2007), *Radiochemistry 49, 281*
- [53] T. Nakamura, *et al.* (2005), *Sequential Measurements of Cosmic-Ray Neutron Spectrum and Dose Rate at Sea Level in Sendai, Japan Journal of Nuc. Sc. and Tec., Vol.42, No.10, 843-853*
- [54] M. Kowatari, *et al.* (2005), “*Evaluation of the Altitude Variation of the Cosmic-ray Induced Environmental Neutrons in the Mt. Fuji Area*” *Journal of Nuc. Sc. and Tec., Vol.42, No.6, 495-502*
- [55] M. R. Moser *et al.* (2005), “*Atmospheric Neutron Measurements in the 10-170 MeV Range*”, *29th International Cosmic Ray Conference Pune 2, 421-424*
- [56] A. Bonardi *et al.* (2009), “*On a measurement of atmospheric stopping muons and neutron fluxes*”, *31st International Cosmic Ray Conference Lodz*

- [57] T. Suzuki, D. F. Measday (1987), “*Total nuclear capture rates for negative muons*”
Phys. Rev. C, Vol.35, No.6, 2212-2224
- [58] W. N. McElroy *et al.* (1967), “*A computer-automated Iterative Method for Neutron Flux Spectra Determination by Foil Activation*”, AFWL-TR-67-41, Air Force Weapons Laboratory

Ringraziamenti

Termino questo mio lavoro ringraziando le seguenti persone:

- Marco Aglietta e Walter Fulgione per il lavoro svolto insieme, per tutte le profique discussioni, e per tutte le cose da loro imparate senza le quali questa tesi non avrebbe potuto essere scritta;
- Gianmarco e Ana Amelia, per la collaborazione al lavoro qui descritto, e tutte le persone conosciute al Gran Sasso (Giulia, Maddalena in particolare): con loro tutti ho condiviso bellissime giornate;
- tutte le persone del quarto piano di fisica con cui è stato un piacere dividere con loro le mie giornate a Torino: ringrazio specialmente Milena per i consigli ricevuti e a cui mando un augurio di veder esauriti i propri progetti, qualunque essi siano;
- tutti i miei amici di Fisica e non per i bellissimi 3 (e non solo) anni vissuti insieme: tra questi ringrazio in particolar modo Elena per la quale non v'è spazio sufficiente per elencare i motivi;
- mia sorella per tutti i consigli di vita ricevuti e per essermi stata vicina nei momenti importanti;
- i miei genitori e i miei parenti grazie ai quali ho la pazienza e la calma che molti mi invidiano.

Infine, ringrazio Laura per aver accettato di percorrere con me quella lunga e accidentata strada che è la vita, con la speranza che continui a farlo senza mai voltarsi indietro.